Politecnico di Torino

Politecnico di Torino

Department of Environment, Land, and Infrastructure Engineering
Master of Science in Petroleum Engineering
A. y. 2021/2022
October 2022

FLUID-DYNAMIC AND GEOMECHANICAL MODELLING OF THE SHALLOW FORMATIONS OF THE PO PLAIN

Tutors:
Prof. Vera Rocca
Prof. Christophoros Benetatos
Dr. Celine Eid
Dr. Nacer Benlalam

Candidate:
Mustafa Mehrem

This page intentionally left blank

Abstract

Ground water extraction is one of the leading causes of land subsidence\uplift compromising the mechanical integrity of bearing rock formation.

In this research we apply 3D integrated modelling approach to analyze the induced mechanical response to a shallow aquifer in the Emilia-Romagna region. Geological investigation was performed over the area of study to define a representative model. The latter was populated with sought out petrophysical and mechanical properties, on sections of the grid depending on the aim of the simulation. Water production and well piezometric data were collected within the last 20 years, to reproduce the dynamic behaviour of the aquifer. In addition, injection wells were implemented in the dynamic model to reproduce the aquifer recharge. The resulting pressure maps were used as an input in a commercial software dedicated for geomechanical analysis, to estimate the resulting ground movements.

Acknowledgement

In the name of Allah: “And say: My Lord, increase me in knowledge.” (Quran 20:114)

Firstly, I am grateful to Allah for his blessings.

Then, I dedicate my whole efforts to my parents and my siblings. Without your support, I would have never been the person I am today. Thanks very much and may God shower you with his blessings.

Also, I want to give a special thank you to my supervisor Professor Vera Rocca and the co-supervisors, Dr. Celine Eid, Dr. Nacer Benlalam, and Prof. Christophoros Benetatos. Without their assistance throughout the process, this work would have never been accomplished. Thanks very much.

I would also like to thank the amazing professors at POLITO for their dedication and support.

Finally, I want to give a big shoutout to my friends, both in Egypt and Italy.

Mustafa Mehrem

Contents

LIST OF FIGURES

LIST OF TABLES

NOMENCLATURE

σ Normal Stress
τ Shear Stress
F Force
A Area
σ_{ij} Stress Tensor
ε Longitudinal Strain
γ Shear Strain
C_{ijhk} Stiffness Tensor
E Young's Modulus
v Poisson's Ratio
λ Lamé's Constant; Slope of Normal Consolidation Line under Isotropic Stress Conditions
G Shear Modulus
K Bulk Modulus
σ' Effective Stress
p_f Pore Pressure
α Biot Coefficient
q Deviatoric Stress
e Void Ratio
V Volume
V_w Water Volume
V_v Void Volume
v Specific Volume
n Porosity
OCR Over-Consolidation Ratio
σ'_p Pre-Consolidation Pressure
σ'_{vo} Current Mean Effective Stress
κ Slope of Swelling Line under Isotropic Stress Conditions
c_C Slope of Normal Consolidation Line under One-Dimensional Stress Conditions
c_s Slope of Swelling Line under One-Dimensional Stress Conditions
c_M Uniaxial Compressibility
E'_{ed} Oedometer Modulus
c_b Oedometer Test Compressibility
CSL Critical State Line
Γ CSL's Specific Volume at Unit Pressure
N Specific Volume at Unit Pressure
S_w Water Saturation
u Displacement
ρ Density
β Water Compressibility
S_s Specific Storage

γ_w Specific Weight of Water
h Hydraulic Head
K Hydraulic Conductivity

1 Introduction

1.1 Problem Definition

Land subsidence is a serious problem that is caused by natural and artificial causes, but it is commonly related to the underground flow of solids and liquids. So, this phenomenon has been exaggerated by water and hydrocarbons exploitation.

Land subsidence has been encountered in many parts of the world, leading to serious damages to the buildings and the infrastructure. The estimation of the total costs is imponderable because it has also indirect costs, like the decrease of land fertility in deltaic areas by the intrusion of saltwater.

The Po Plain in northern Italy is one of the major places affected by subsidence due to anthropogenic fluids extraction. The study area of this research is located in Emilia-Romagna. Its selection for this research is because land subsidence in this area is caused by both water and hydrocarbons extraction.

Water is extracted for civil, industrial, and agricultural uses from a shallow aquifer system, while, at deeper depths, gas storage and extraction activities take place.

In this research, geological description of the shallow layers of the Po Plain and the aquifer groups used for water extraction. Then, we focused on aquifer group A, for which a dataset was collected. This dataset contains the petrophysical properties of the aquifer and the aquitard, the production data of the study area, and the piezometric data for Emilia-Romagna, the study area, and the punctual data for two wells that are in the areal range of the study area.

These data were used then to perform the dynamic simulation using the same commercial software used in the petroleum industry to match the production and pressure.

Finally, the matched pressures were used to perform a geomechanical simulation to estimate the subsidence/uplift caused by groundwater extraction and recharge.

2 Literature Review

2.1 Land Subsidence

Land subsidence is the sinking of the Earth's land surface. It is a potentially dangerous hazard that can be triggered by a variety of natural or artificial factors, but is most commonly produced by solid or fluid movement underground (Herrera-García et al., 2021).

According to (Ritzema, 1994), one or more of the following processes are included in the term "subsidence":

- Compression/Compaction: The change in soil volume caused by the application of a static external load is known as compression. Compaction is achieved artificially through the application of a momentary load, such as rolling, tamping, or vibration.
- Consolidation: The gradual, slow compression of a cohesive soil caused by the weight acting on it as water, or water and air, is forced out of the spaces in the soil.
- Shrinkage: The reduction in soil volume caused by capillary stress as the soil dries.
- Oxidation: The conversion of organic carbon to carbon dioxide, which is then released into the atmosphere.

Compression/compaction and consolidation are two of the four processes that include soil mechanics; they occur both naturally and as a result of human intervention. Consolidation occurs only in clays and other low-permeability soils. Consolidation differs from compaction, which is a mechanical, instantaneous process that occurs exclusively in soils containing some sand. The degree of subsidence caused by these processes is a function of the original material's pore space, the compacting mechanism's efficacy, and the thickness of the deposit being compacted. Shrinkage is a physics-based phenomenon that takes place in the soil. The physical ripening of a newly reclaimed soil can result in irreversible shrinkage. The moisture content of the soil and the evapotranspiration of soil water determine how much subsidence occurs as a result of shrinkage. In organic soils, oxidation is a biological process that happens. It is caused by microorganisms that utilise organic substances as energy and carbon sources. The process is influenced by the soil's air and water conditions.

2.1.1 Natural Causes of Land Subsidence

Consolidation due to sediment loading, tectonics, volcanism, and dissolution of comparatively soluble carbonate and evaporite minerals are all examples of natural subsidence processes. Human activities including land and water use, as well as climatic fluctuation, have a direct impact on some natural subsidence processes. The use and diversion of existing surface-water supplies, as well as a reliance on groundwater supplies, are typical outcomes of the development of water resources to support human habitation and agricultural cultivation. These actions have the potential to change the natural hydrologic system, amplifying natural subsidence processes or causing new artificial subsidence (Galloway et al., 2016).

Basin formation is the outcome of crustal sinking. The sequence stratigraphic characteristics and burial history are used to begin the analysis of the basin subsidence history (Cong et al., 2015). According to (Ingersoll, 2011), Sedimentary basins sink due to crustal thinning,

mantle thickening while cooling, tectonic loading on the crust, subcrustal loading, asthenospheric flow dynamics, and increase in density of deep crustal layers “crustal densification”. An example of such basins is the Orange Basin, southwest Africa (Hirsch et al., 2010). Basin initiation occurred during the Early Cretaceous rifting between South America and Africa, which culminated in the breakup of the South Atlantic. The continents' disintegration was accompanied by massive, temporary volcanic activity. Initial faulting and the formation of grabens accompanied such rifting.

In places underlain by water-soluble rocks such as carbonate and evaporite rocks, sinkhole collapse is a regular event. A landscape with sinkholes, sinking streams, and springs, which indicate the presence of underlying voids or caves, is typical of karst topography. The term 'karst' has been broadened to cover both characteristics that represent surficial dissolution processes (epigenic karst) and, more recently, features that indicate dissolution processes at depth (hypogenic karst); both result in subsurface voids with the possibility for subsidence, rapid sinkhole collapse, or cave formation. It is impossible to predict when a catastrophic event will occur; nevertheless, by mapping areas underlain by water-soluble rocks at national and global sizes, it is possible to predict where such events are likely to occur (Galloway et al., 2016).

2.1.2 Land Subsidence Caused by Human Activities

The reduction in the volume of formations causes land subsidence. Anthropogenic land subsidence is associated with subsurface fluid withdrawal from porous medium. The pore fluid pressures fall as fluids are removed from porous media. Because effective stress, the difference between total stress and pore fluid pressure, controls deformation of porous media, a reduction in pore fluid pressure reduces pore volume. Compaction is the hydrological term for this process. Compaction is permanent and irreversible when effective stress surpasses the yield strength of the media's granular skeleton (Holzer and Galloway, 2005).

(Herrera-García et al., 2021) conducted a study of the susceptibility of land subsidence due to anthropogenic causes. Fig. 2.1. highlights some of the major cases worldwide. The color scale shows the probability ranges, ranging from very low (VL) to very high (VH). The white hatched polygons show countries with no groundwater data, and the possible subsidence merely provides information on vulnerability.

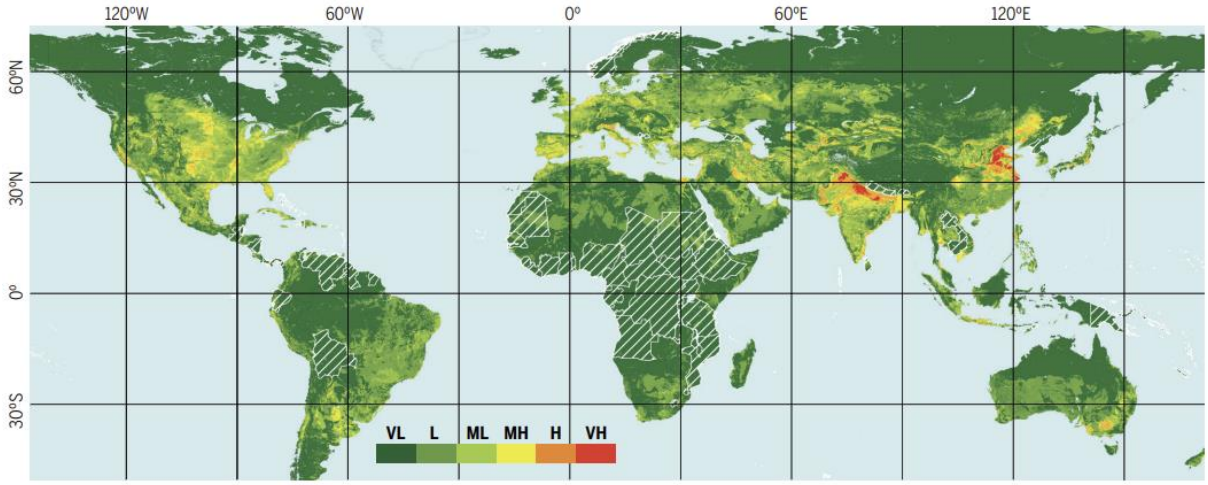

Fig. 2.1. Main anthropogenic land subsidence regions in the world (Herrera-García et al., 2021)

As can be noticed from the above figure, land subsidence occurs in many regions around the globe. It is of much concern in areas that have dense populations and those which are located close to deltas, lagoons or seas. Table 2.1 (Gambolati and Teatini, 2021) shows in detail the locations in Fig. 2.1, with relevant subsidence information.

Table 2.1. Selected areas of anthropogenic land subsidence in the world (Gambolati and Teatini, 2021)

No.	Location	Maximum Subsidence (m)	Recent subsidence Rate (cm/yr)	Depth of Pumping (m)	Area of Subsidence (km^2)
1	Wadi Al-Yutamah	0.3 (1993–1996)		0–150	150
2	Anthemountas Basin		3.5 (1995-2001)	30–150	40
3	Bangkok	2.1 (1933–2002)	2 (2005-2010)	30–300	700
4	Beijing	1.1 (1955–2007)	5 (2003-2010)	20–400	4,200
5	Celaya	3.1 (1985–2008)	9 (2007-2011)	50-200	50
6	Eloy Basin	3.0 (1948–1977)	4 (2010-2014)	100-760	1,000
7	Hanoi	0.5 (1988–2003)	7 (2007-2011)	0–80	35
8	Ho Chi Minh	0.4 (1996-2005)	4 (2006-2010)	50-240	250
9	Houston	3 (1915-2000)	2.5 (2005-2012)	60-900	12,000
10	Jakarta	4.1 (1974-2010)	26 (2007-2011)	40-240	660

11	Kolkata	1.1 (1956-2000)	4 (2001-2005)	50-160	150
12	Las Vegas	2 (1935-2000)	2.5 (1997-1999)	200-300	250
13	Latrobe Valley	1.3 (1960-1977)	1.5 (2006-2011)	0-150	400
14	Lorca	2.2 (1992-2012)	16 (1992-2011)	50-300	140
15	Taipei	2 (1955-1991)	-0.7 (1989-2003)	50-250	200
16	Mexico City	13 (1960-present)	30 (2007-2011)	0-350	250
17	Ravenna	1.4 (1897-2002)	0.2 (1998-2002)	80-450	400
18	San Joaquin Valley	10 (1930-present)	30 (2007-2011)	60-600	13,500
19	Santa Clara Valley	4.3 (1910-1995)	-0.5 (1992-2000)	50-280	500
20	Shanghai	2.6 (1958-2002)	1.5 (2006-2011)	10-330	5,000
21	Su-Xi-Chang area	1.1 (1960-1995)	3 (2003-2008)	20-200	4,000
22	Tehran	3.0 (1989-2004)	15 (2004-2005)	20-100	500
23	Tokyo	4.3 (1900-1975)	-0.3 (1991-2005)	0–400	3,400
24	Venice	0.12 (1952-1973)	0.1 (2008-2011)	70–350	150
25	Wairakei	14.5 (1950-present)	9 (2000-2007)	250-800	25
26	Xian	2.3 (1959-1995)	11 (2005-2012)	50-370	240
27	Zamora de Hidalgo		18 (2007-2011)	0–300	15
28	Tianjin	3.2 (1959-2007)	11 (1975-1985)	0-550	8000
29	Nile River delta	–	1 (2004-2010)	20-200	4800
30	Lagos	–	0.6 (2011-2018)	50-200	350

As shown in the table, the highest known settlement is more than 14 meters, and it occurred due to geothermal water production at the Wairakei geothermal field in New Zealand. Also, Settlement depths of more than ten meters are not uncommon. It is also noticed that the wells' depths vary from those tapping extremely shallow water table aquifers near to the ground surface to those reaching very deep gas/oil reservoirs (4000–5000 m). Moreover, the sinking area can be as large as 13,500 km^2 in the San Joaquin Valley

and 12,000 km^2 in the Houston-Galveston area, Texas, where groundwater was drained aggressively.

2.1.2.1 Land Subsidence due to Groundwater Withdrawal

Anthropogenic land subsidence due to groundwater pumping out is an issue that can be seen all over the world.

2.1.2.1.1 Groundwater Systems

(Cashman and Preene, 2013) differentiate three groundwater terminologies; aquifers, aquicludes, and aquitards.

a- *Aquifer*: A stratum is a collection of strata or a section of a stratum that contains water (i.e. saturated and permeable).
b- *Aquiclude*: A soil or rock layer that is part of a group of strata, or forms an entire stratum that has very low permeability and impedes groundwater flow.
c- *Aquitard*: A stratum, group of strata, or portion of a stratum made up of soil or rock with intermediate to low permeability, producing only very modest groundwater flows.

They also delineates aquifer systems as to be either unconfined or confined.

1. Unconfined Aquifers:

   The most straightforward aquifer for most people to envision and comprehend is probably one that is unconfined. The aquifer's soil or rock has voids, pores, or fractures. These spaces are open to the atmosphere and saturated (i.e., full with groundwater) up to a point known as the "water table." The water level in a monitoring well drilled into the saturated region of the aquifer will be equal to the water table as shown in Fig. 2.2. (Cashman and Preene, 2013).

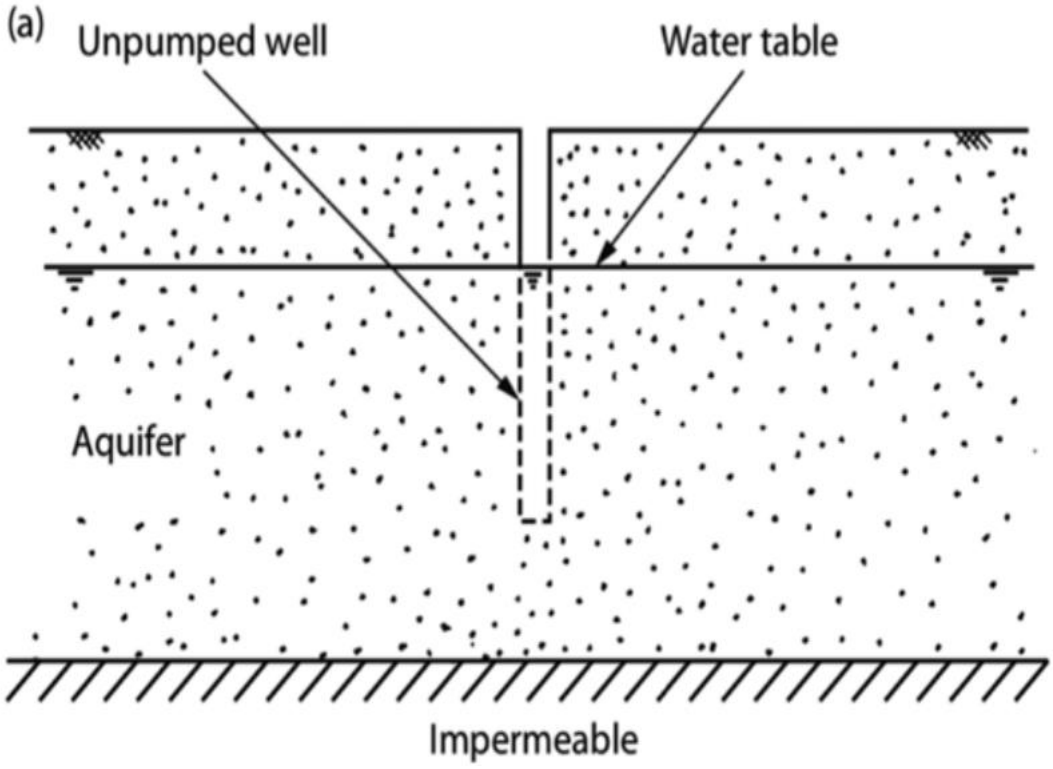

Fig. 2.2. Unconfined Aquifer and the Water Table (Cashman and Preene, 2013)

The level in the aquifer where the pore water pressure is zero (i.e. equal to atmospheric pressure) is known as the water table; the line where the pore water pressure is zero is also known as the phreatic surface. Below the water table, soils have positive pore water pressures and are saturated. The pressure in the voids will be negative (i.e., less than atmospheric) above the water table, and depending on the kind of rock or soil, at some height above the water table, they may be unsaturated and contain both air and water.

2. Unconfined Aquifers:
   A confined aquifer is covered by a very low-permeability layer called a "aquitard" or "aquiclude," which provides a confining bed, as opposed to an unconfined aquifer, which has an open top to the atmosphere and may have an unsaturated zone above the water table. Because the water pressure is higher than atmospheric everywhere in a limited aquifer, it is completely saturated. A monitoring well drilled into the confining bed would first be dry. Water will enter the borehole once it has pierced the aquifer, rising to a level above the aquifer's surface. A restricted aquifer lacks a water table because the pore water pressures are consistently higher than atmospheric everywhere. The "piezometric level," which reflects the height to which water levels would rise in monitoring wells drilled into the aquifer, is used to characterize the pressure distribution instead. Fig. 2.3. (Cashman and Preene, 2013) shows the confined aquifer with the piezometric level.

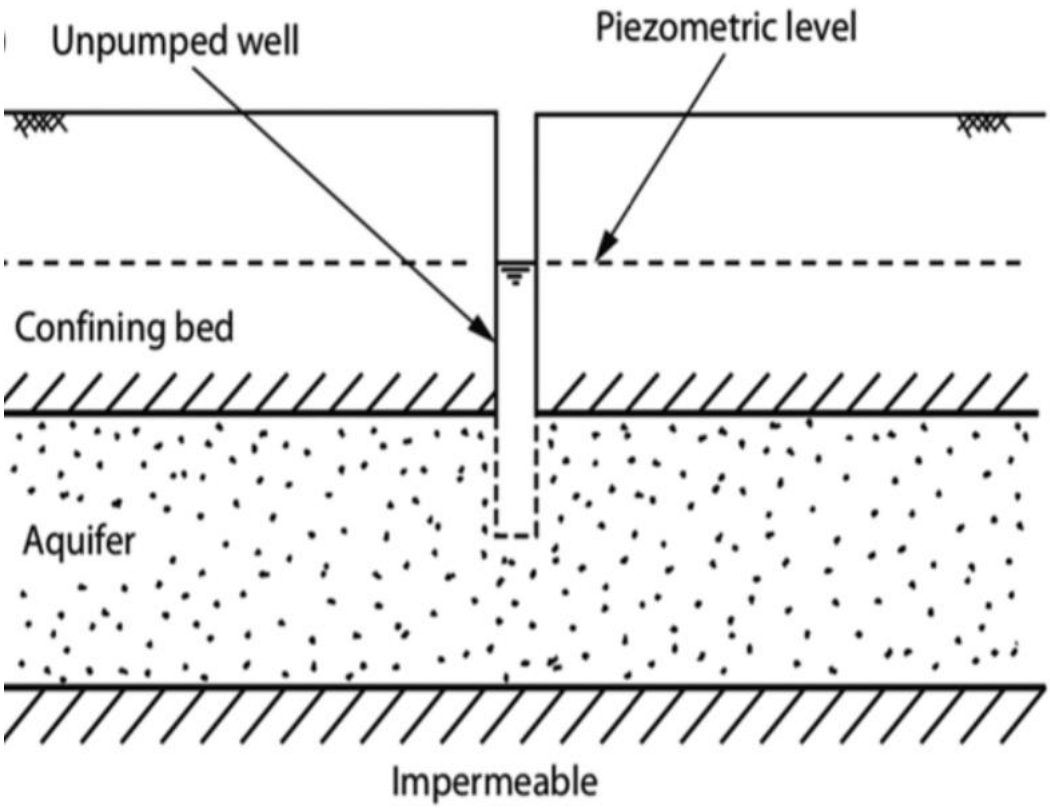

Fig. 2.3. Confined Aquifer with the Piezometric Level (Cashman and Preene, 2013)

2.1.2.1.2 Anthropogenic Land Subsidence due to Water Production

Groundwater withdrawal is responsible for more than 80% of identified subsidence in the United States, according to the US Geological Survey (Wade et al., 2016). In the coastal region, land subsidence owing to groundwater depletion, combined with global sea level rise, poses a major environmental hazard (Sun et al., 1999). That is the reason that groundwater pumping was regulated in Texas after subsidence of the ground had reached 10 feet (Greuter et al., 2021). Also, according to (Qin et al., 2018), groundwater supplies nearly two-thirds of Beijing's water, and the depletion from the city's unconsolidated aquifers has been over 10.4 billion m^3 over the last 50 years. By 2010, groundwater pumping in the city had caused a cumulative subsidence of more than 100 mm over a 3,900 km^2 region, with a maximum cumulative subsidence of more than 1,200 mm. In Beijing, the sinking has resulted in major social and economic losses, as well as significant damage to subterranean infrastructure.

In reaction to changes in water level, all aquifer systems deform to some extent. Seasonal recharge and outflow from unconsolidated heterogeneous aquifer systems often induce mild elastic (recoverable) expansion and compression, as well as uplift and subsidence of the ground surface (on the order of millimeters to centimeters).

The water supplied to a pumping well in confined aquifer systems is originally sourced from aquifer system deformation, i.e., water expansion and granular skeleton or matrix compression. In reality, the storativity of aquifers and the interbedded and confining

aquitards in the aquifer system is determined by water and matrix compressibilities and porosity.

As groundwater drains from fine-grained aquitards into coarser-grained aquifers, either elastic (recoverable) or inelastic (unrecoverable) compaction occurs, depending on the amount of the pressure change and the aquitards' stress history.

Because of their compressibility, aquitards within and around the aquifer system are particularly prone to massive compaction. Aquitard matrix compressibility (and thus storativity) is often many orders of magnitude more than coarser-grained aquifer compressibility, which is typically much greater than water compressibility. As a result, much of the water from aquitard storage comes through matrix deformation. As a result, aquitard storativity and drainage control aquifer compaction and account for the majority of the land subsidence that occurs as a result of groundwater development in these aquifer systems (Holzer and Galloway, 2005).

2.1.2.2 Land Subsidence due to Oil and Gas Extraction

Unlike aquifer systems, petroleum reservoir deformation often entails significant compaction of sandy sections. Sands compact at the higher effective stresses generally seen in oil fields, according to laboratory research and observations of deformation in oil wells. Sand grains are crushed during compaction (Holzer and Galloway, 2005).

Compaction is the loss of volume in a reservoir as a result of reduced pressure due to fluid production (water, oil and gas). Compaction and subsidence are two terms that refer to two different processes. Subsidence is a change in the level of a surface, whereas compaction is a volumetric change in a reservoir. The compacting reservoir functions as a support for boosting petroleum in some fields. The rock-drive in the North Sea's weak chalks and California's diatomites can be many times stronger than the fluid-expansion drive. However, the subsequent subsidence can cause serious damage to pipelines, roadways, and other buildings unless they are engineered to withstand the strain (Uko et al., 2018).

One of the most well-known cases of subsiding hydrocarbon fields is the Ekofisk field. The seafloor beneath the operational platform had sunk over 3 meters in 1984, and the restoration effort cost over a billion dollars. Ekofisk's subsidence peaked at 6.7 meters at the end of 2000, and has been steadily declining at a rate of roughly 0.4 meters per year since then. The Wilmington oil field in California, which has endured 9 meters of subsidence, is another well-known example of oil field subsidence. In the Wilmington field, the annual rate of surface subsidence reached up to 70 cm (Taherynia et al., 2013).

For Ekofisk field, it also demonstrated a fall in formation pressure from 7200 psi at discovery to 3200 psi at prospective abandonment, resulting in a decrease in porosity from 38% to 33%.

On another note, (Benetatos et al., 2020) states that a particular area of the oil and gas business is the study of ground movements brought on by underground natural gas storage (UGS). Natural gas is kept in underground geological formations (such as depleted hydrocarbon reservoirs, aquifers, and salt caverns) during UGS activity. The UGS is a global

solution that has been used to ensure real-time reaction to market gas demand, high levels of elasticity in the management of production and transport infrastructure, and the maintenance of "strategic" reserves. The phenomenon known as "earth breathing" is caused by the seasonal and cyclical withdrawal and injection of gas, which causes a similar seasonal and cyclical oscillation (subsidence/rebound) of the ground surface, which indicates a possible uplift, the reverse of subsidence, due to gas injection operations.

2.1.3 Measuring Land Subsidence

Land subsidence can be measured by some methods showed by (Galloway et al., 2008) that are summarized in Table 2.2.

In general, the approaches are used to measure changes in the position of the ground surface. The visible position is usually a geodetic reference mark that has been developed to ensure that any shift is due to deep-seated ground movement rather than surface phenomena like frost heave. Any movement of a reference mark, whether vertical or horizontal, is monitored in respect to other observation sites or related to a global reference frame. When the reference mark is presumed to be stable or its movement is known and measured, it can be used as a control point to determine the absolute positioning of the observation point. Land subsidence has been measured using this method, which involves repetitive surveys of bench marks that are referred to a known and considered stable reference frame.

Table 2.2. Methods of Land Subsidence Monitoring (Galloway et al., 2008)

[GPS—Global Positioning System; InSAR—Interferometric Synthetic Aperture Radar; LiDAR—Light Detection and Ranging; PSI—Permanent Scatterer Interferometry; SAR—Synthetic Aperture Radar]

Method	Component displacement	Resolution (mm)	Spatial density (samples/survey)	Spatial scale
Spirit level	vertical	0.1-1	10-100	line-network
Geodimeter	horizontal	1	10-100	line-network
Borehole extensometer	vertical	0.01-0.1	1-3	point
Horizontal extensometer				
Tape	horizontal	0.3	1-10	line-array
Invar wire	horizontal	10^{-4}	1	line
Quartz tube	horizontal	10^{-5}	1	line
GPS	vertical horizontal	20 5	10-100	network
Satellite SAR interferometry				
InSAR	range	1-10	10^{5}-10^{7}	map pixel

PSI	range	1	variable	map pixel
LiDAR				
Tripod	vertical horizontal	10 10	10^6-10^8	3D point cloud
Airborne	vertical horizontal	300 360	variable	map pixel

2.2 Natural Subsidence and Uplift in the Po Plain (Italy)

As shown in the previous section, northern Italy is one of the major subsidence areas in the world. This area has witnessed major subsidence and uplift through its geological age.

(Gambolati et al., 2000) shows that the sea created a vast gulf during the start of the Quaternary period, and the current plain was underwater as far as Turin, as shown in Fig. 2.4 (a) (Gambolati et al., 2000). The slow filling of this depression was caused by the gradual disintegration of the mountains, soil erosion, and sediment transport by surface runoff, which continued until quite recently. Large areas formed during the Würm glaciation. The sea level was approximately 100 meters lower than it is now 20,000 years ago, and the Po river valley extended deep into the Adriatic Sea as shown in Fig. 2.4 (b) (Gambolati et al., 2000). The sea began to rise after the end of the Würm glaciation, pushing the coastline northward until it reached its current form some 6000 years ago. Since then, the water level has fluctuated just slightly and has remained rather steady.

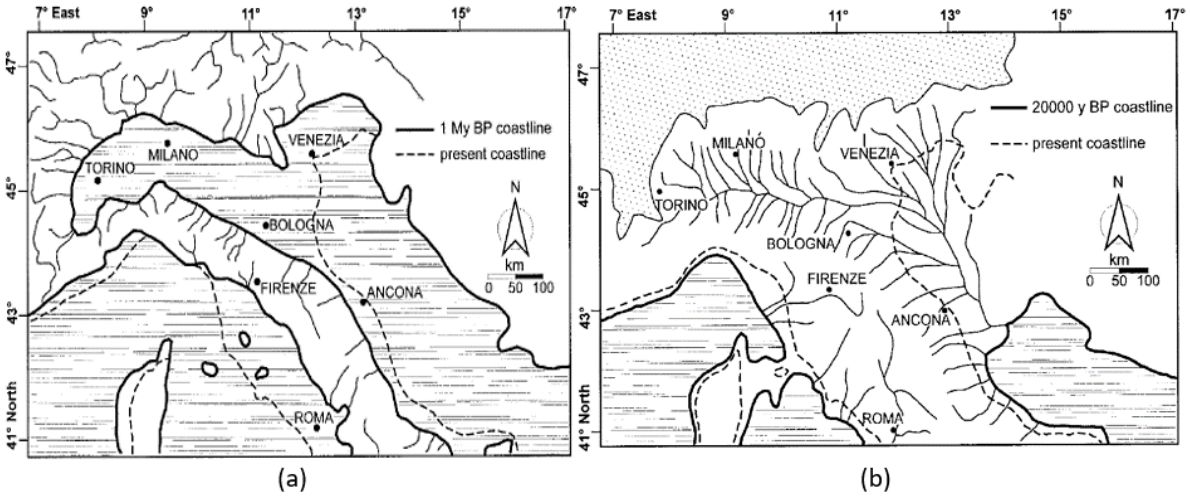

Fig. 2.4. Map of northern Italy for: (a) 1 million years before present and (b) 20,000 years before present. (Gambolati et al., 2000)

While the entire Po Valley is subjected to a long-term natural subsidence of a few millimetres per year caused by the consolidation of the self weight of the thick alluvial deposits, in the period after 1950 some cities in northern Italy (Milan, Venice, Ravenna and Bologna are the most instructive cases) suffered very strong subsidence, which in some cases reached rates of several tens of centimetres per year (Carminati and Martinelli, 2002).

Bologna, a major city in the Po Plain, has also been affected by land subsidence. Between 1897 and 1957, data from optical leveling revealed surface movements of up to 2-3 mm/y (Stramondo et al., 2007).

Then, After world war II, anthropogenic land subsidence has increased dramatically basically due to groundwater pumping from a shallow well-developed multiaquifer system due to the rapid growth of inhabitants, cultivation and industrial use (Modoni et al., 2008) and subordinately due to gas production from a number of onshore and offshore reservoirs (Teatini et al., 2006).

Fig. 2.5 shows the present-day subsidence rate per year (Carminati and Martinelli, 2002).

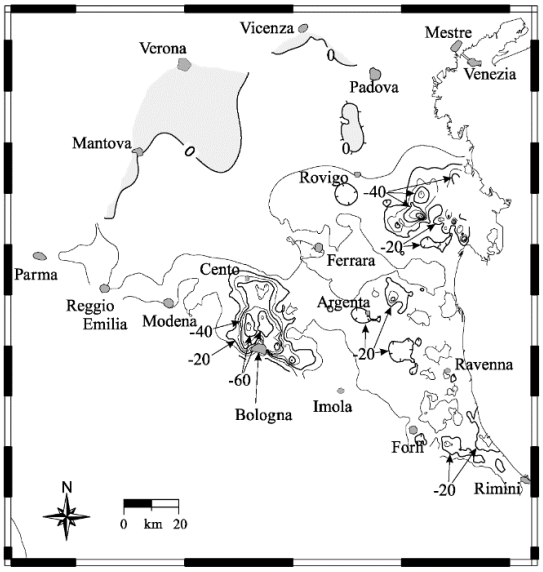

Fig. 2.5. Rate of vertical movements (in mm/yr). Negative values mean subsidence, while positive values mean uplifting (Carminati and Martinelli, 2002).

3 Theoretical background for the analysis of land subsidence

3.1 Constitutive Laws and Poroelasticity

Constitutive laws are a set of equations that describe the relationship between applied stresses and the resulting deformation of a rock medium. This section discusses several key principles, parameters related to the theory of elasticity and poroelasticity.

Stresses and strains are the pillars of geomechanics and they were illustrated by (Fjaer, 2008) as follows in this section.

Consider the scenario depicted in Fig. 3.1. A is the cross-sectional area at a). If the force applied through this area is indicated by F. Then, the stress σ at this cross-section is defined as:

$$\sigma = \frac{F}{A} \qquad (3.1)$$

Then, at the cross-section b), the force acting through it is the same as that acting through a). However, the area A' of the cross-section at b) is less than A. As a result, the stress at b) is greater than the stress at a), indicating that the stress is dependent on the position inside the stressed sample.

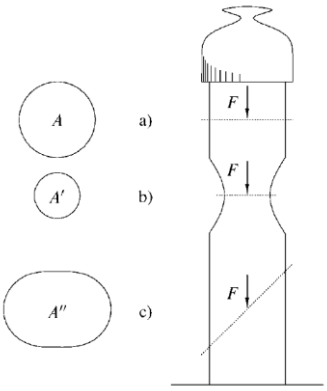

Fig. 3.1. Relationship between Stress and Force(Fjaer, 2008)

Finally, at the cross-section c), the force is no more perpendicular to the area. The force can therefore be decomposed into one normal to the cross-section component F_n and one parallel to the section component F_p as shown in Fig. 3.2. Then, we have two kinds of stress; the *normal stress* is equal to the quantity:

$$\sigma = \frac{F_n}{A''} \qquad (3.2)$$

While the *shear stress* is equal to the quantity:

$$\tau = \frac{F_P}{A''} \qquad (3.3)$$

The magnitude of each is determined by the surface's orientation.

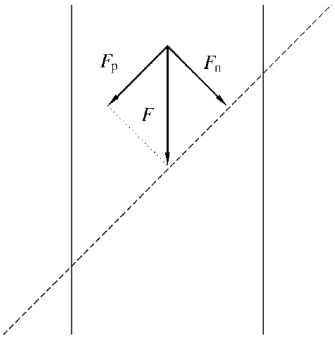

Fig. 3.2. Force Decomposition (Fjaer, 2008)

In three-dimensional problems, three normal stresses and six shear stresses components form altogether the *stress tensor*.

$$\sigma_{ij} = \begin{bmatrix} \sigma_x & \tau_{xy} & \tau_{xz} \\ \tau_{yx} & \sigma_y & \tau_{yz} \\ \tau_{zx} & \tau_{zy} & \sigma_z \end{bmatrix} \quad (3.4)$$

Where, $\tau_{xy} = \tau_{yx}$, $\tau_{xz} = \tau_{zx}$, and $\tau_{yz} = \tau_{zy}$, giving rise to six independent values of stresses.

Fig. 3.3 shows a simplified example of a square subjected to the different types of stresses.

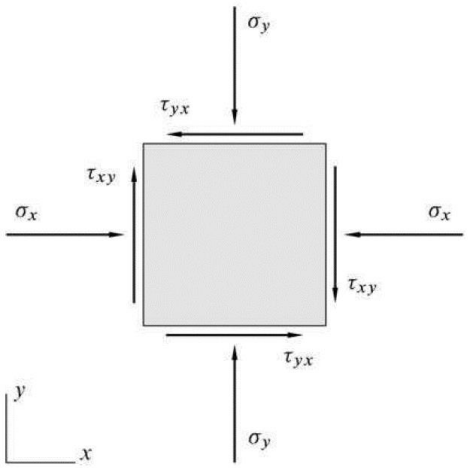

Fig. 3.3. Two-Dimensional Stress Components (Fjaer, 2008)

As a result of the applied stresses on the sample, the relative positions of the particles inside it are modified in such a way that the new positions cannot be achieved simply by rigid translation and/or rotation of the sample. Hence, the sample is strained.

As shown by (Fjaer, 2008) and represented in Fig. 3.4, The material shows two different reactions for the stresses applied. The first one is called the *longitudinal strain* ε, and is calculated as:

$$\varepsilon_x = \frac{\partial u_x}{\partial x} \quad (3.5)$$

$$\varepsilon_y = \frac{\partial u_y}{\partial y} \quad (3.6)$$

$$\varepsilon_z = \frac{\partial u_z}{\partial z} \quad (3.7)$$

The other response is called the *shear strain γ,* which is half of the change of the angle between two coinciding material fibers lined up with the coordinate axes on the reference system.

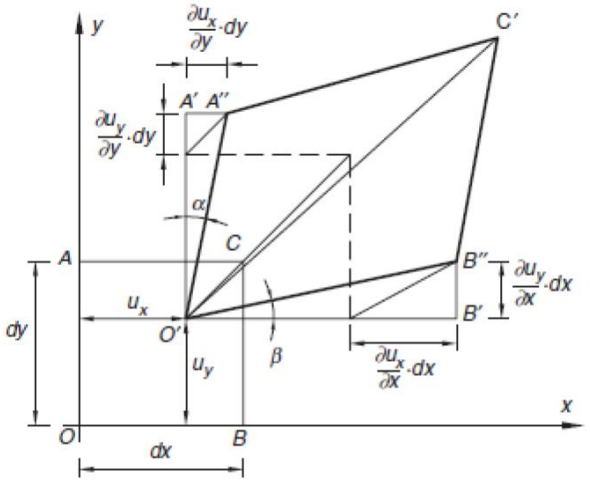

Fig. 3.4. Longitudinal and Shear Strains (Fjaer, 2008)

Shear strain can be calculated by the following equation:

$$\varepsilon_{xy} = \frac{1}{2}\left[\frac{\partial u_x}{\partial y} + \frac{\partial u_y}{\partial x}\right] \tag{3.8}$$

But the engineering shear strain can be represented as:

$$\gamma_{xy} = 2\varepsilon_{xy} = \left[\frac{\partial u_x}{\partial y} + \frac{\partial u_y}{\partial x}\right] \tag{3.9}$$

Similarly,

$$\gamma_{yz} = 2\varepsilon_{yz} = \left[\frac{\partial u_y}{\partial z} + \frac{\partial u_z}{\partial y}\right] \tag{3.10}$$

$$\gamma_{xz} = 2\varepsilon_{xz} = \left[\frac{\partial u_x}{\partial z} + \frac{\partial u_z}{\partial x}\right] \tag{3.11}$$

Strains are also represented by the strain tensor:

$$\varepsilon_{ij} = \begin{bmatrix} \varepsilon_x & \gamma_{xy} & \gamma_{xz} \\ \gamma_{yx} & \varepsilon_y & \gamma_{yz} \\ \gamma_{zx} & \gamma_{zy} & \varepsilon_z \end{bmatrix} \tag{3.12}$$

3.2 Elasticity

(Fjaer, 2008) shows that a material body's behavior is classified as "elastic" if, when loaded, it has potential energy that can be released during unloading, causing it to fully recover to its former shape. The elastic constitutive law takes into consideration the elastic body's stress-strain relationship and is written as:

$$\sigma_{ij} = \frac{\partial \psi}{\partial \varepsilon_{ij}} \tag{3.13}$$

where σ_{ij} represents tiny stresses, ε_{ij} represents infinitesimal strains, and ψ represents the stress potential (strain energy per unit volume). According to (Fjaer, 2008), if we examine a linear stress-strain connection (Fig. 3.5 a), with the body's starting condition being undeformed and in equilibrium, the aforementioned function may be expressed as:

$$\sigma_{ij} = C_{ijhk}\varepsilon_{hk} \tag{3.14}$$

Where C_{ijhk} is the stiffness tensor. It is an ensemble of independent scalars that relate stresses to subsequent strains and are known as elastic constants.

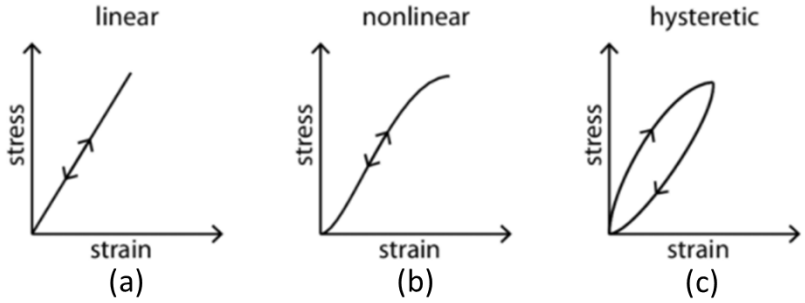

Fig. 3.5. stress-strain relationsships for: (a) linear elasticity, (b) nonlinear elasticity and (c) hysteresis. (Fjaer, 2008)

The Generalized Hooke's law (equation (3.15) is the most well-known constitutive law. It describes the behavior of a linear elastic material which is also isotropic. The latter means that when a material is subjected to a state of stress, its behavior does not depend on the orientation of the stress applied. The law describes such materials with only two elastic constants; E, young modulus, and v, poisson's ratio.

$$\begin{bmatrix} \sigma_x \\ \sigma_y \\ \sigma_z \\ \tau_{xy} \\ \tau_{yz} \\ \tau_{zx} \end{bmatrix} = \frac{E(1-\nu)}{(1+\nu)(1-2\nu)} \begin{bmatrix} 1 & \frac{\nu}{1-\nu} & \frac{\nu}{1-\nu} & 0 & 0 & 0 \\ \frac{\nu}{1-\nu} & 1 & \frac{\nu}{1-\nu} & 0 & 0 & 0 \\ \frac{\nu}{1-\nu} & \frac{\nu}{1-\nu} & 1 & 0 & 0 & 0 \\ 0 & 0 & 0 & \frac{1-2\nu}{2(1-\nu)} & 0 & 0 \\ 0 & 0 & 0 & 0 & \frac{1-2\nu}{2(1-\nu)} & 0 \\ 0 & 0 & 0 & 0 & 0 & \frac{1-2\nu}{2(1-\nu)} \end{bmatrix} \begin{bmatrix} \varepsilon_x \\ \varepsilon_y \\ \varepsilon_z \\ \gamma_{xy} \\ \gamma_{yz} \\ \gamma_{zx} \end{bmatrix} \tag{3.15}$$

(Zoback, 2007) stated that for homogeneous isotropic rocks, there exist common five elastic moduli. Elastic moduli relate the material's stresses and the corresponding elastic deformation. These elastic moduli include,

- **Young's modulus E:** is a measure of the material's stiffness. It is calculated from uniaxial compression test by dividing the longitudinal stress by the strain.

$$E = \frac{\sigma}{\varepsilon} \tag{3.16}$$

- **Poisson's ratio *v*:** is the ratio between the lateral expansion and the longitudinal shortening.

$$v = -\frac{\varepsilon_y}{\varepsilon_x} \tag{3.17}$$

- **Lamé's constants λ, μ:**

Lamé's constant λ: related to the young's modulus and the poisson's ratio through the equation;

$$\lambda = \frac{vE}{(1+v)(1-2v)} \tag{3.18}$$

Lamé's constant μ: it is equal to the shear modulus G. Both express the ability of the material to withstand shear deformation and are calculated as the ratio between the shear stress and the corresponding shear strain.

$$G = \frac{E}{2(1+v)} \tag{3.19}$$

- **Bulk Modulus K:** it represents the stiffness of the material in hydrostatic conditions and its reciprocal (1/K) defines the compressibility.

$$K = \lambda + \frac{2}{3}G \tag{3.20}$$

The above elastic characteristics are strongly dependent on the material's depositional history, stress-strain history, and material type. When measured using acoustic velocities, they are categorized as dynamic moduli, and when measured using stress-strain measurements, they are classified as static moduli.

Table 3.1 (Gould, 2013) shows the mechanical properties for some common rocks and materials.

Table 3.1. Mechanical properties for common rocks and materials (Fjaer, 2008)

Material	Density ρ 10^3 (kg/m^3)	Young's modulus E (GPa)	Poisson's ratio ν
Unconsolidated sands	1.5–1.7	0.01–0.1	~0.45
Sandstone	2.0–2.65	0.1–30	0–0.45
Clay	1.9–2.1	0.06–0.15	~0.40
Shale	2.3–2.8	0.4–70	0–0.30
High porosity chalk	1.4–1.7	0.5–5	0.05–0.35
Low porosity chalk	1.7–2.0	5–30	0.05–0.30
Basalt	2.7–2.9	50–100	0.2–0.3
Granite	2.6–2.8	5–85	0.1–0.34
Dolomite	2.4–3.2	10–100	0–0.5
Limestone	1.4–2.9	2–100	0–0.3
Gneiss	2.7–3.1	40–100	0.1–0.3
Marble	2.7–3.2	5–90	0–0.3
Ice	0.9	8	0.35
Steel	7.9	200	0.28

3.3 Poroelasticity

As stated by (Fjaer, 2008), the poroelasticity principle deals with the body as it is heterogeneous in the microscopic level, and thus constructs constitutive models based on the behavior of a saturated material body subjected to loading while considering the role of the void space in both fluid flow and deformation.

The first work regarding poroelasticity was conducted by (Terzaghi, 1923). He assumed that the grains that constitute the porous medium are incompressible and so can be treated as an elastic body. Also, his work was built on oedometric conditions (one-dimensional compression test). His principle states that the total stress on a point in a porous medium equals the sum of the total effective intergranular stress and the pore pressure;

$$\sigma' = \sigma - \delta p_f \qquad (3.21)$$

Where σ' and σ are the effective and total stress respectively, p_f is the pore pressure and δ is the Kronecker delta, that is used because the ability of the fluid to hold shear stress is negligible.

After this, (Biot, 1941) expanded the work of Terzaghi to three-dimensional compression. He also removed the assumption that the solid grains are incompressible, made by Terzaghi. Eq. (3.21) was formulated to be;

$$\sigma' = \sigma - \alpha\delta p_f \qquad (3.22)$$

Where α is Biot coefficient. Biot coefficient can be calculated from the equation;

$$\alpha = 1 - \frac{K'}{K_s} \qquad (3.23)$$

Where;

- K' is the bulk modulus of the rock skeleton. K' is estimated from the drained hydrostatic test (also called jacketed test). In such test conditions, shown in Fig. 3.6

(a) (Fjaer, 2008), the fluid in the pore spaces is free to escape out of the pores so that the pore pressure is kept constant.

- K_s is the bulk modulus of the solid grains. $K_s$is estimated from the undrained hydrostatic test (also called the unjacketed test) as shown in Fig. 3.6 (b). Undrained conditions mean that the fluid in the pore spaces is trapped inside and is not allowed to escape, so that the pore pressure increases by the same value as the hydrostatic stress $\Delta\ \sigma\ = \Delta\ p_f$. This allows the characterization of the solid grains stiffness.

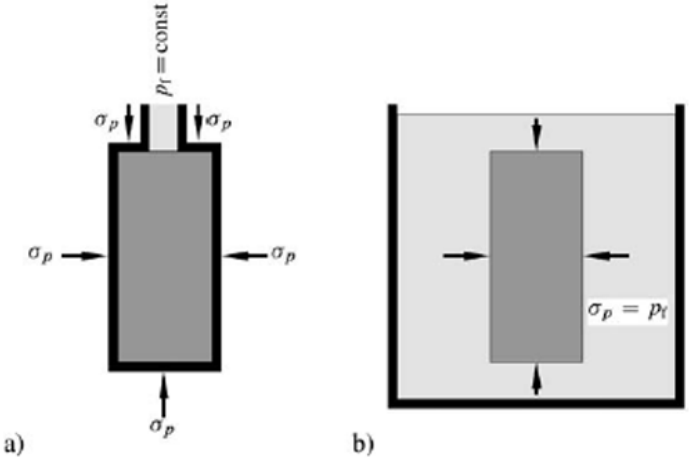

Fig. 3.6. (a) "Drained" test, (b) "Undrained" test (Fjaer, 2008)

Regarding Biot's work described in equations (3.22) and (3.23), we should differentiate two types of rocks;

- Weakly-framed rocks or *soils*: soils have very small value of the ratio $(\frac{K'}{K_s})$, making α=1.
- Stiff-framed *rocks*: stiff rocks have values of K' comparable to that of K_s, making α<1. The skeleton of the hard rocks carries most of the loads.

3.4 Plasticity

Plasticity theory is a constitutive model that describes a material's non-elastic behavior. This behavior is ductile, meaning the material can deform permanently without losing its load-bearing capacity.

(Fjaer, 2008) demonstrated that the total strain is composed of an elastic strain and a plastic strain.

$$d\varepsilon_{ij} = d\varepsilon_{ij}^{e} + \varepsilon_{ij}^{p} \qquad (3.24)$$

The elastic strain can be calculated by the constitutive equations and that is the part recovered when the load is removed, while the plastic strain is not recovered and is permanent even after the stress removal.

(Fjaer, 2008) shows that the yield point is the point above which a permanent change in the material occurs, even after the removal of the load. So, it is the starting point of the plastic strain. In Fig. 3.7, σ_p is the yield point.

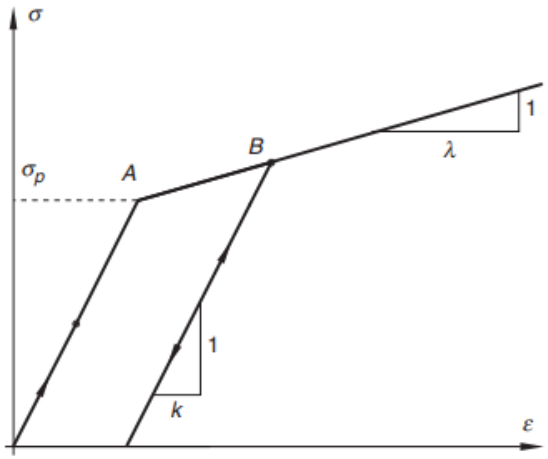

Fig. 3.7. Elastic and plastic behavior (Fjaer, 2008)

(Fjaer, 2008) explains the term "failure" in the context of soils as the "slide" on any plane inside the soil mass that happens when the ratio of the shear stress to the effective normal stress exceeds a critical point, i.e. We can assume that the critical shear stress for which shear failure occurs relies on the normal stress operating across the failure plane because it is widely known that friction regulates soil strength. The Mohr-Coulomb criterion is most typically used to describe soil failure.

$$|\tau| = \sigma' \tan\phi' \qquad (3.25)$$

Where τ is the shear stress, σ' is the effective normal stress, and ϕ' is the friction angle.

According to Mohr's hypothesis, the minimum and maximum primary stresses alone determine pure shear failure, not the intermediate stress. As a result, many experimental tests must be carried out by increasing the normal stresses and drawing the corresponding Mohr circles in order to ascertain the strength parameters of the soil. The failure envelope shown in Fig. 3.8. is referred to as the envelope of these circles and is illustrated as follows:

$$\tau = c' + \sigma' \tan\phi' \qquad (3.26)$$

Where c' is the cohesion, the intercept with the shear axis.

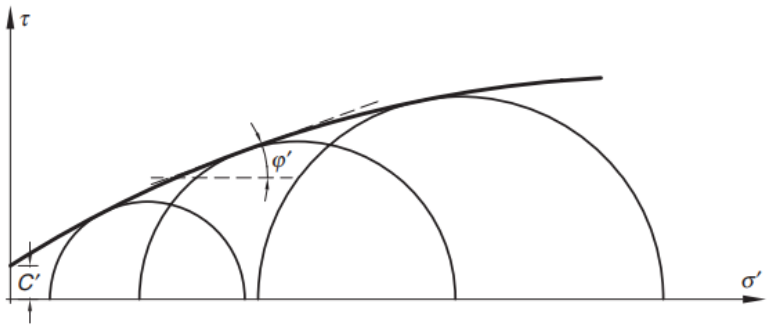

Fig. 3.8. The Failure Envelope (Fjaer, 2008)

As stated by (Laloui and Rotta Loria, 2020), the idea of perfect plasticity was first employed by Coulomb (1773) and Rankine (1857) to address geotechnical stability issues involving geomaterials, and it was then used by Saint Venant (1870) and Lévy (1870) to analyze various materials, including metals.

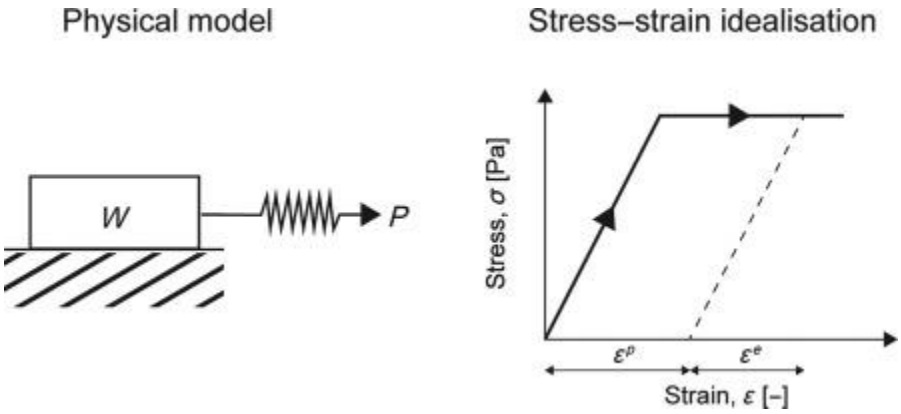

Fig. 3.9. Perfect Plasticity (Laloui and Rotta Loria, 2020)

The yield surface of materials that behave in accordance with the notion of perfect plasticity is uniform in size and shape as plastic deformations develop. The yield function in these circumstances is solely a function of the stress condition. In other words, the elastic domain that defines the mechanical behavior of materials that are fully plastic is constant.

3.4.1 CAM Clay Model

(Fjaer, 2008) shows that for systems with no or little cement between the individual grains, soil mechanics was created. Because clay meets this description, its behavior was investigated under various test settings, leading to the development of the Cam-Clay (CC) and Modified Cam-Clay (MCC) models. It's crucial to start by defining two key terms in soil mechanics:

- Void ratio *e:* is the ratio between the voids volume and the volume of the solid grains.

$$e = \frac{V_{void}}{V_{solid}} = \frac{n}{1-n} \qquad (3.27)$$

- Specific volume *v:* it is the total bulk volume (grains plus solid grains) divided by the volume of the grains.

$$v = \frac{V_{solid} + V_{void}}{V_{solid}} = 1 + e \qquad (3.28)$$

- The relationship between e and v with the porosity n

$$n = \frac{e}{1+e} = \frac{v-1}{v} \qquad (3.29)$$

The CC and MCC models are models that are capable of simulating realistic volume changes caused by soil deformations. They go through three key characteristics of soil behavior:

1) Strength
2) Dilatancy or compression (the change in volume that accompanies shearing)
3) Critical state in which soil elements can be distorted indefinitely without any changes in stress or volume.

Fig. 3.10 (Fjaer, 2008) shows the loading and unloading and the accompanying changes in void ratio. The deposition process (loading), shown in Fig. 3.10 as A-B-C, adds an extra overburden weight to the soil sample, increasing the effective vertical stress σ'_v. This causes loose sediments to consolidate, resulting in a reduction in the voids volume, i.e. the void ratio *e*. The applied effective vertical load decreases with a corresponding decrease in void ratio during erosion (unloading), indicated by segment DC; however, it can be observed on the graph that points B and D have differing void ratios for the same effective stress. This demonstrates that residual strain exists after unloading.

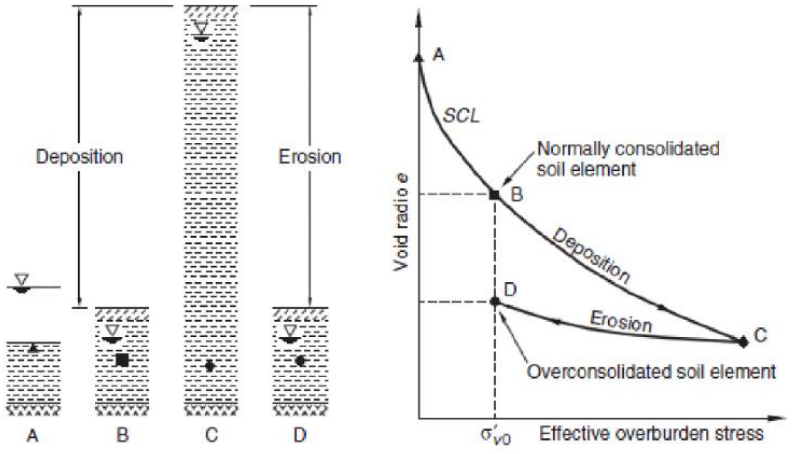

Fig. 3.10. Relation between loading/unloading and the void ratio in a soil sample (Fjaer, 2008)

The *Overconsolidation Ratio (OCR)* is used to evaluate the level of consolidation of soil samples. It is calculated by dividing the preconsolidation pressure, i.e. the maximum stress level ever experienced by the soil which is represented by point C in Fig. 3.10 by the current mean effective stress which is represented by point D in the figure above.

$$OCR = \frac{\sigma_p'}{\sigma_{vo}'} \qquad (3.30)$$

- The soil is considered normally consolidated when $OCR = 1$, which means the maximum stress level a material has previously encountered is not more than the current stress level.
- The soil is considered overconsolidated if $OCR > 1$, suggesting that the material's maximal stress level is greater than the current level of stress.

Mean effective stress p', deviatoric stress q and specific volume ν are the soil parameters that are used in the CC and MCC models.

3.4.1.1 Normal Consolidation vs. Swelling

A soil sample is steadily squeezed under drained conditions and isotropic stress conditions ($\sigma_1' = \sigma_2' = \sigma_3' = p'$). Under these conditions, a straight virgin consolidation line and a series of straight swelling lines, which represent the unloading-reloading conditions, can be established, as shown in Fig. 3.11 (Fjaer, 2008).

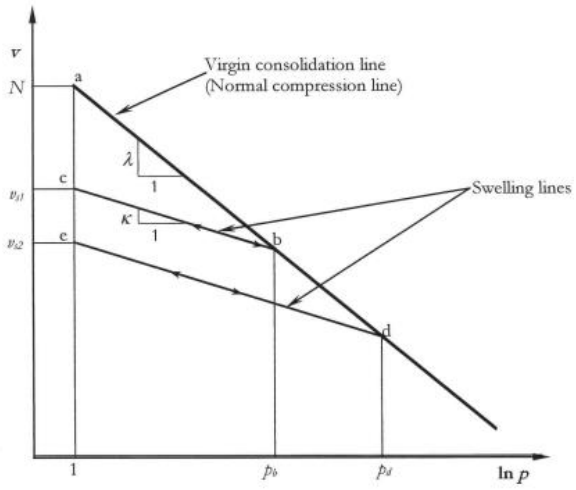

Fig. 3.11. Soil Sample Behavior under Drained, Isotropic Compression (Fjaer, 2008)

In the above figure, suppose the soil sample with initial conditions at point a is exposed to an isotropic stress equals p_b', then it follows the normal consolidation line alone the ab path. Then, if the stress is removed at point b, then the response of the soil follows the swelling line bc. Now, if the soil is reloaded again from point c, then it follows the swelling line again till it reaches the point b stress conditions (maximum stress level ever experienced), with any stress addition exceeding the p_b' value, the soil response again follows the normal consolidation line. So, if the new stress level equals p_d', the soil response follows the normal consolidation line up to point d. After this, if the soil sample is again unloaded, it again follows the swelling line de.

The normal consolidation line in Fig. 3.11. is expressed by the following equation according to (Fjaer, 2008)

$$v = N - \lambda lnp' \quad (3.31)$$

Also (Fjaer, 2008) defined the swelling line is by the following equation:

$$v = v_\kappa - \kappa lnp' \quad (3.32)$$

Where λ and κ are the slopes of the normal consolidation line and the swelling line, respectively. N is the specific volume at unit pressure, located at the normal consolidation line. Its value varies according to the units of measurement. These metrics describe the characteristics of a certain soil.

The soil is classified as normally consolidated if its current state is on the normal consolidation line, indicating that its stress-strain behavior is largely elasto-plastic. When a soil is unloaded, it becomes overconsolidated, which means it has a smaller void ratio than a normally consolidated soil for the same applied effective stress. Soil does not exist outside of the normal consolidation line in general, and when it does, it is in an unstable state.

Overconsolidated soils have a stiffness that is higher than that of normally consolidated soils (slope of swelling lines is less than that of the virgin consolidation line).

3.4.1.2 One-Dimensional Compression and Swelling

(Terzaghi et al., 1996) showed that the one-dimensional drainage and deformation process can be approximated by oedometer tests. In oedometer tests, a strong ring encircles the specimen. A stiff cap is used to apply vertical load to the top of the soil specimen, and the compression is monitored with a dial indicator. Through rigid porous rocks, drainage can be enabled from both the top and bottom faces of the specimen.

The relationship between the stress and strain in the z-direction is shown by (Fjaer, 2008) in Fig. 3.12,

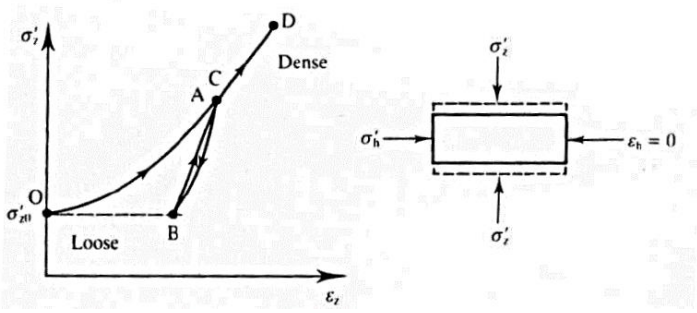

Fig. 3.12. Oedometer Test Conditions (Fjaer, 2008)

The following parameters can be obtained from the oedometer test (Fjaer, 2008):

1- The preconsolidation stress σ'_p, and the recompression, compression, and swelling indices can be obtained as shown in Fig. 3.13.

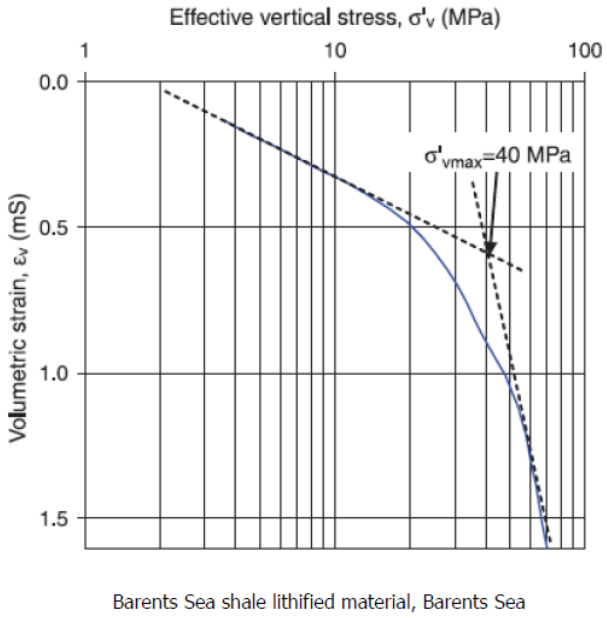

Fig. 3.13. Preconsolidation Stress Determination from Oedometer Tests (Fjaer, 2008)

2- The recompression index, compression index, and swelling index, indicated in Fig. 3.14 by sections A-B, C-D, and E-F, respectively.

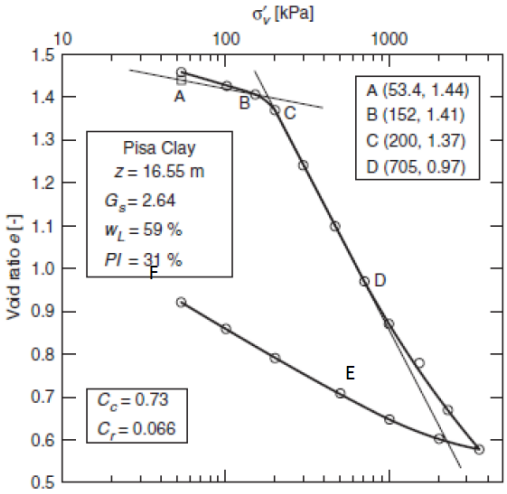

Fig. 3.14. Recompression, Compression, and Swelling Indices (Fjaer, 2008)

The compression and the swelling indices are the slopes of the $e - log\sigma'_v$ graph as shown in Fig. 3.15.

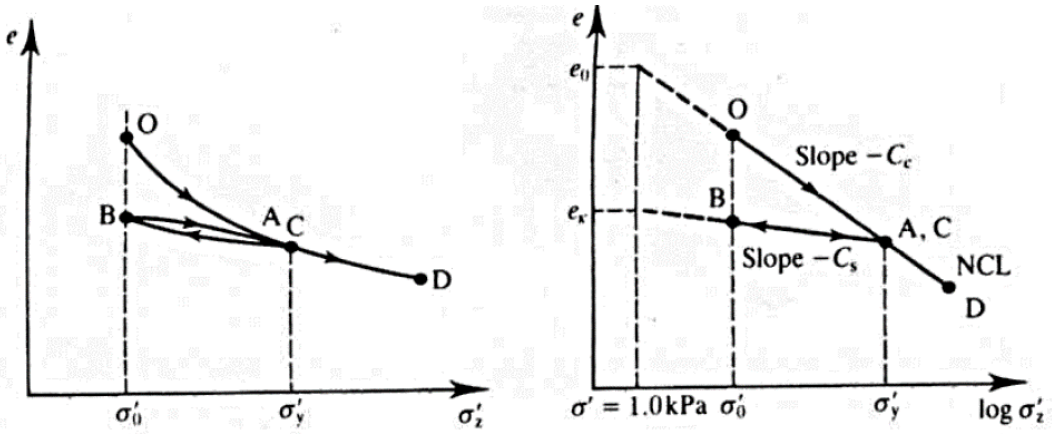

Fig. 3.15. Void Ratio vs. Effective Vertical Stress (Fjaer, 2008)

$$e = e_0 - c_C \log \sigma'_v \tag{3.33}$$

$$e = e_\kappa - c_s \log \sigma'_v \tag{3.34}$$

Since $dv = de$ and $\log x = 0.43 \ln x$, we have,

$$c_C = 2.3\lambda \tag{3.35}$$

$$c_S = 2.3\kappa \tag{3.36}$$

3- Uniaxial compressibility or compaction coefficient, c_M, which equals:

$$c_M = \frac{d\varepsilon_v}{d\sigma_v} \tag{3.37}$$

For an isotropic soil it equals,

$$c_M = \frac{(1+\nu)(1-2\nu)}{(1-\nu)E} \tag{3.38}$$

In fact, (Gambolati and Teatini, 2015) showed that technicians measure the following quantity in the lab:

$$c_b = \frac{de}{dp}\frac{1}{1+e} \tag{3.39}$$

which is the inverse of the oedometric modulus:

$$E'_{ed} = \frac{d\sigma'_v}{d\varepsilon_v} = -\frac{d\sigma'_v}{de}(1+e) \tag{3.40}$$

They also showed that it is related to the actual 1-D vertical compressibility as:

$$c_M = \frac{e^{p_f c_b} - 1}{p_f} \tag{3.41}$$

3.4.1.3 Critical State Conditions

When sustained shearing of a soil sample leads to a state where more shearing can occur without any changes in stress or volume, this is known as the critical state condition (Fjaer, 2008). The Critical State Line (CSL) is what distinguishes it.

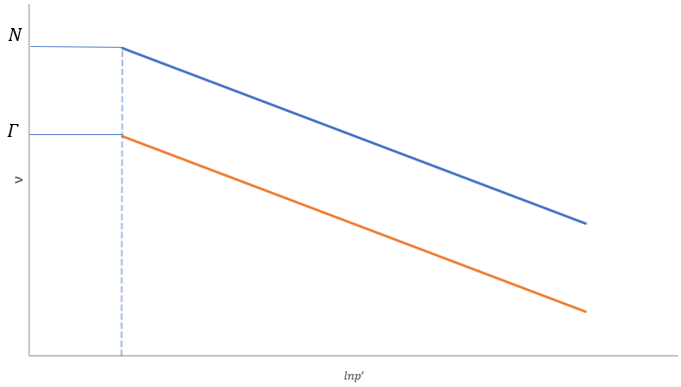

Fig. 3.16. CSL (orange) and normal consolidation line (blue) (Fjaer, 2008)

Where Γ is the CSL's specific volume at unit pressure. Its value also depends on the measuring units, just like *N.*

Γ can be related to *N* according to the model used as follows;

CC model:

$$\Gamma = N - (\lambda - k) \tag{3.42}$$

MCC model:

$$\Gamma = N - (\lambda - k)ln2 \tag{3.43}$$

3.4.2 Land Subsidence Calculation

The theory of consolidation by Biot in 1941, which states that consolidation is the response of a compressible porous medium to changes in the flow field acting within it, has long been accepted as the best way to understand land subsidence as demonstrated by (Gambolati and Teatini, 2015).

(Shen et al., 2006) showed that because the hydraulic conductivity of an aquifer is significantly higher than that of aquitards, a groundwater seepage problem is typically simplified as a quasi-three-dimensional problem. That is, groundwater in aquifers is assumed to flow horizontally, whereas in an aquitard, only vertical seepage is evaluated and treated as the source/sink flux. As groundwater withdrawal produces groundwater head decline across a vast area, one-dimensional consolidation analysis was commonly used to estimate land subsidence owing to groundwater withdrawal. However, predicting the entire area's sinking is challenging. A two-step method has typically been used to anticipate land subsidence over a vast area. First, a groundwater seepage model based on the assumption of horizontal flow in aquifers and vertical flow in aquitards is used to simulate the change in groundwater head. The effective stress and soil deformation are next estimated using the

groundwater head calculated in the first stage. The sum of each soil layer's compression is land subsidence.

The method for calculating land subsidence and the relevant equations used were presented by (Gambolati and Teatini, 2015).

The elastic body deformation is controlled by the change in σ' in Terzaghi equation (3.21). Cauchy equations show the incremental effective stress and pore pressure for the initial conditions of undisturbed material.

$$\begin{aligned}\frac{\partial \sigma_{xx}}{\partial x}+\frac{\partial \tau_{xy}}{\partial y}+\frac{\partial \tau_{xz}}{\partial z}&=\frac{\partial p}{\partial x}\\ \frac{\partial \tau_{yx}}{\partial x}+\frac{\partial \sigma_{yy}}{\partial y}+\frac{\partial \tau_{yz}}{\partial z}&=\frac{\partial p}{\partial_y}\\ \frac{\partial \tau_{zx}}{\partial x}+\frac{\partial \tau_{zy}}{\partial y}+\frac{\partial \sigma_{zz}}{\partial z}&=\frac{\partial p}{\partial z}\end{aligned} \qquad (3.44)$$

Where σ_{ii} is the incremental normal stress, and τ_{xz} is the incremental shear stress. Also, τ_{xy}=τ_{yx}, τ_{yz}=τ_{zy}, and τ_{xz}=τ_{zx}

The relationship between the incremental stress tensor and the incremental strain tensor is the same as the one in eq. (3.15).

The geomechanical properties along the vertical direction are typically different from those in the horizontal direction in layered aquifer systems formed in a depositional environment. Five independent parameters—$E_v, E_h, \upsilon_v, \upsilon_h, and\, G_v$—completely define the geomechanical characteristics of a transversally isotropic porous material. The well-known equation shows that G_h depends on E_h and υ_h:

$$G_h=\frac{E_h}{2(1+\nu_h)} \qquad (3.45)$$

For isotropic soils, the vertical compressibility is calculated by the following equation:

$$c_M=\frac{(1+\nu)(1-2\nu)}{(1-\nu)E} \qquad (3.46)$$

If we substitute the aforementioned relationships between the effective stress and strain into the Cauchy equations, we get the equilibrium equations for an isotropic media (a porous medium sensitive to pore pressure changes p):

$$G\nabla^2 u + (\lambda + G)\frac{\partial \epsilon}{\partial x} = \frac{\partial p}{\partial x}$$
$$G\nabla^2 v + (\lambda + G)\frac{\partial \varepsilon}{\partial y} = \frac{\partial p}{\partial y} \qquad (3.47)$$
$$G\nabla^2 w + (\lambda + G)\frac{\partial \varepsilon}{\partial z} = \frac{\partial p}{\partial z}$$

Where ∇^2 is the Laplace operator, u, v, and w are the incremental position vector components in the x, y, and z directions, and λ is the Lamé constant shown in equation (3.18). Finally, ε is the total volumetric strain and is calculated from the following equation:

$$\varepsilon = \varepsilon_{xx} + \varepsilon_{yy} + \varepsilon_{zz} \qquad (3.48)$$

From the equations (3.47), there are three equations in four unknowns u, v, w, and p. So, a fourth equation is needed. This equation is provided by the equation that governs the ground water flow in the aquifer.

The fourth equation is:

$$\frac{1}{\gamma}\nabla \cdot \left(K_{ij}\nabla\right) = n\beta\frac{\partial p}{\partial t} + \frac{\partial \varepsilon}{\partial t} \qquad (3.49)$$

Where

γ= water specific weight,

∇= gradient operator=$\frac{\partial}{\partial x} + \frac{\partial}{\partial y} + \frac{\partial}{\partial z}$,

n= porosity,

β= water compressibility, and

$$K_{ij} = k_{ij}\frac{\gamma}{\mu} \qquad (3.50)$$

Is the hydraulic conductivity tensor, where:

K_{ij} is the hydraulic conductivity tensor, k_{ij} is the intrinsic permeability, and μ is the water viscosity.

1- The equations (3.47) and (3.49) give the so-called ***coupled model.***
As stated by (Gambolati et al., 2000), the incremental effective stresses and the fluid dynamic gradients that form inside the porous medium are closely related when an aquifer, an oil/gas reservoir, or a confining bed suffers a change of the internal flow

and stress fields (usually owing to fluid withdrawal). Biot [1941] provided the first mathematical explanation of this intricate relationship. A coupled model is one that uses the Biot equations to represent both flow and stress.

2- For the ***uncoupled theor***: introduced by Theis [1935]:
   a. The flow equation is firstly solved for p, independently of the stress equation, using the specific elastic storage parameter, using the diffusion equation he introduced.
   b. Then, the pressure variation's gradient is integrated into the equilibrium equation (3.47).

   The uncoupled formulation:

$$\nabla\left(k_{ij}\frac{\nabla p}{\gamma}\right)=\gamma(n\beta+c_M)\frac{\partial p}{\partial t} \qquad (3.51)$$

   When the medium is transversally isotropic and with the axes aligned with the main directions of anisotropy, equation (3.51) becomes:

$$\frac{\partial}{\partial x}\left(K_{xx}\frac{\partial p}{\partial x}\right)+\frac{\partial}{\partial y}\left(K_{yy}\frac{\partial p}{\partial y}\right)+\frac{\partial}{\partial z}\left(K_{zz}\frac{\partial p}{\partial z}\right)=S_s\frac{\partial p}{\partial t} \qquad (3.52)$$

   With S_s is the specific elastic storage coefficient, which is calculated as follows:

$$S_s=\gamma(n\beta+c_M) \qquad (3.53)$$

According to (Gambolati and Teatini, 2015), the uncoupled equation has served as the foundation for classical groundwater hydrology since the very beginning of the creation of quantitative hydrogeology [e.g., Theis, 1935; Jacob, 1940; Todd, 1960; Bear, 1972]. The uncoupled pressure solution can be used safely to predict land subsidence in compacting sedimentary basins, with the coupled and uncoupled solutions being virtually indistinguishable at any time of practical interest.

In fact, Geo-technicians define and measure the following compressibility for soil samples from aquifers and aquitards in the laboratory:

$$c_b=\frac{de}{dp}\frac{1}{1+e} \qquad (3.54)$$

Where e is the void ration defined in equation (3.27).

Consider a 1-D soil sample that has a length Δz at the beginning and is deformed vertically by $\delta(\Delta z)$. The vertical compressibility an in the classical elastic theory is defined as:

$$c_M = \frac{\delta(\Delta z)}{\Delta z}\frac{1}{p} = \frac{\varepsilon}{p} \tag{3.55}$$

Where p in the sample compaction $\delta(\Delta z)$ is negative, equivalent to and opposing the incremental effective stress. The void ratio allows us to write:

$$\delta(\Delta z) = [\Delta z + \delta(\Delta z)]\frac{e}{1+e} - \Delta z\frac{e_0}{1+e_0} \tag{3.56}$$

Where e_0 is the initial void ratio prior to the compaction.

Since the individual soil grains are assumed to be incompressible in equation (3.56), the sample volume $\delta(\Delta z)$ is equal to the variation of the porous volume as shown in Fig. 3.17. (Gambolati and Teatini, 2015). Divide both sides of equation (3.56) by Δz, then rearrange to get:

$$\varepsilon = \frac{\delta(\Delta z)}{\Delta z} = \frac{e - e_0}{1 + e_0} \tag{3.57}$$

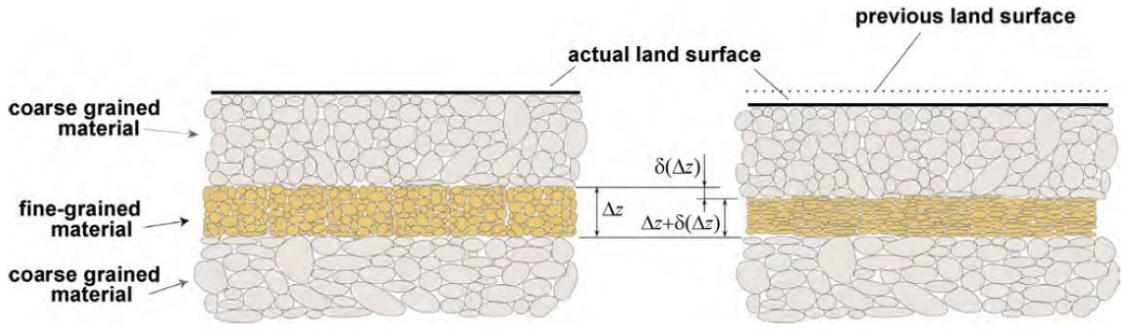

Fig. 3.17. Compaction of a Soil with Incompressible Grains (Gambolati and Teatini, 2015)

Also:

$$c_M = \frac{\varepsilon}{p} = \frac{e - e_0}{p(1 + e_0)} \tag{3.58}$$

If c_M is independent of p, then we have:

$$\frac{de}{dp} = c_M(1 + e_0) \tag{3.59}$$

In other words, the void ratio is inversely related to the incremental pressure p (for any given initial e_0). Equation (3.59) is substituted into equation (3.54) to produce:

$$c_b = c_M\frac{1 + e_0}{1 + e} = c_M\frac{1 + e_0}{1 + e_0 + c_M p(1 + e_0)} = \frac{c_M}{1 + c_M p} \tag{3.60}$$

c_M and c_b don't coincide until the incremental pressure p gets close to zero. The two compressibilities, c_M and c_b, are typically not equal and cannot be regarded as constants at the same time. From equation (3.57), the expression for c_b versus c_M is as follows:

$$c_b = \frac{1+e_0}{1+e}\frac{d\varepsilon}{dp} = \frac{1}{1+\varepsilon}\frac{d\varepsilon}{dp} \tag{3.61}$$

If c_M is constant, then $\frac{d\varepsilon}{dp} = constant$ and we have:

$$c_b = \frac{c_M}{1+\varepsilon} = \frac{c_M}{1+c_M p} \tag{3.62}$$

(Gambolati and Teatini, 2015) states that it is simple to eliminate the assumption of constant c_M and obtain the general accurate relationship between c_M and c_b:

$$c_b = \frac{p\frac{dc_M}{dp} + c_M}{1+c_M p} \tag{3.63}$$

With constant c_b, equation (3.63) can be integrated to get:

$$c_M = \frac{e^{pc_b} - 1}{p} \tag{3.64}$$

Neglecting the compressibility of the individual grain is fully justified by the fact that the order of magnitude of any aquifer system's compressibility is orders of magnitude greater than the compressibility of a single grain. (Gambolati and Teatini, 2015) state that Geerstma in 1975 estimated that $c_M = 0.16x10^{-5}$ bar^{-1} for the silicate grains. To have a comparison with the vertical compressibility values encountered in the sedimentary basin of the Po Plain, refer to Fig. 5.4.

On another note, the difference between c_M and c_b does not exceed 2-3% and the two definitions are essentially equivalent if the ultimate relative compaction ap does not exceed 5% of the compacting unit (which is quite common in real geologic formations, particularly in shallow formations).

3.5 Dynamic and Mechanical Simulations and Coupling Techniques

The estimation of land subsidence requires the use of the dynamic and geomechanical simulations. In this work, we adopted the standard for hydrocarbon reservoir simulation.

As stated by (Fanchi, 2018), a reservoir simulator is a computer made to simulate fluid flow in rock. The use of these programs for applied reservoir simulation is to address reservoir flow issues and have an impact on reservoir management choices.

(Abdoljalal, 2010) states that the dynamic model workflow follows five steps:

a. Data acquisition

In this step, data collection and quality control is performed.

b. Model design

Then, the model is designed according to several factors like the complexity of the phenomon to be studied and the study objectives. Immiscible black oil programs are the most popular simulators.

c. Initialization

Initialization means to assign the initial pressure and saturation values to each cell. Also, the hydrocarbon volumetric evaluations using the static model and material balancing approaches are verified.

d. History matching

By adjusting the input parameters, the model is calibrated during the history matching phase using the available measured pressure and production data.

e. Forecast

Finally, if needed, forecasts of production and recovery are made for various field development scenarios after the model has been correctly calibrated.

(Longuemare et al., 2002) shows that changes in the stress state within and around the reservoir are brought on by variations in reservoir pressure, saturation, and temperature brought on by reservoir production. For some reservoirs, such as weakly compacted reservoirs and fractured or faulted reservoirs, geomechanical impacts can be particularly noticeable.

Stress variations can improve fluid recovery in reservoirs with inadequate reservoir compaction. Reservoir compaction, however, can also lessen reservoir permeability, result in surface subsidence, and harm well machinery.

So, (Abdoljalal, 2010) shows that geomechanical models of a hydrocarbon reservoir are used to enable the prediction of the stress state perturbations caused by hydrocarbon production and storage operations in the reservoir as well as in the immediate environment, such as the cap rock. The approach is also adopt to face production effect in term of land movements.

Through numerical modeling techniques, (Giani et al., 2018) states that assessments of compaction and subsidence can be carried out with varying degrees of coupling between fluid-flow and stress-strain processes.

Due to its simplicity and low cost, the one-way coupling technique (or uncoupled approach) is a popular choice for subsidence analysis because it depicts the lower degree of coupling (in terms of required input parameters and computational time). However, only a two-way coupling or a

completely coupled method can fully account for the impact of rock deformation on petrophysical properties (such as porosity/permeability) and, consequently, on pressure evolution. This effect is especially prominent in shallow, poorly cemented formations.

(Giani et al., 2018) mentions that the methods for coupling geomechanics and fluid flow are primarily divided into fully coupled and partially coupled approaches. The fluid flow and displacement calculations are carried out simultaneously in the fully coupled technique, also known as implicit, and the software is able to solve both the fluid-dynamic and the geomechanical variables. However, compared to other strategies, this strategy necessitates more code development.

(Giani et al., 2018) also states that; if iterated to full convergence, the partially coupled strategy can solve the issue as precisely as the fully coupled solution. For each time step, the fluid-flow and stress-strain equations are individually solved using the partially coupled method. A typical reservoir simulator and geomechanical software are coupled using an interface code to enable communication. Different approaches, such as explicit coupling (one-way coupling) or iterative coupling, can be used to create these interface codes (two-way coupling).

According to (Giani et al., 2018); for the one-way coupling, it is assumed that the formation's petrophysical properties do not change.

Separate reservoir and geomechanical simulators are used to solve the fluid-flow and stress-strain equations. Due to its relatively short processing time, ease of use, and accuracy in both predicting and simulating phenomena, the one-way coupling approach is the most common method for calculating subsidence. Additionally, standard geotechnical laboratory investigation for determining strength and deformation parameters can successfully characterize the geomechanical model.

On the other side, the two-way coupling approach enables modelling the impact of the petrophysical variation brought on by the rock mass deformation on pressure evolution.

According to (Giani et al., 2018), dynamic software and geomechanical software are used to individually and sequentially solve the fluid flow and stress-strain equations for each chosen time step of the investigation.

An interfacial code is used to communicate data back and forth, and eventually an iterative technique is used to update the porosity/permeability. The latter is typically taken into account as a coupling variable because pressure and stress/strain become a function of them. It is typically employed for the analysis of thin, poorly-consolidated formations. However, this method can be computationally time-consuming, and finding the coupling law that defines how petrophysical parameters change in proportion to pressure/deformation requires specialized laboratory study.

When applying small time increments and strict convergence tolerances, the coupling strategy should result in the same outcomes. The selection of time step size in an elastic domain is mostly influenced by the size of the pore pressure variation.

4 Geological Framework

4.1 Geology of the Po Plain

The Po River is the longest river in Italy with 652 km of length and its basin, from a geological standpoint, is a large subsident area between the Alps and the Apennines, generated by tectonic thrusts between the two chains, which cause a lowering in the central part. Fig. 4.1 shows the location of the Po plain with the highlight of Emilia/Romagna region and Bologna within it (semenda.it, n.d.).

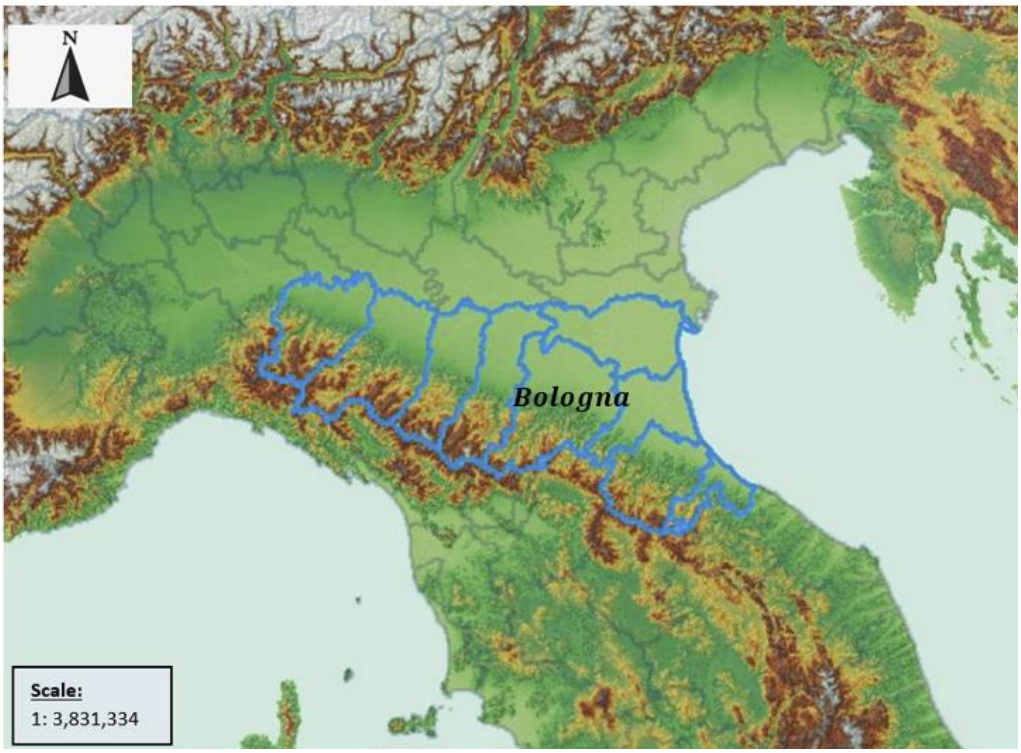

Fig. 4.1. Map of northern Italy with the Alpine and Appennine mountains. Emilia Romagna provinces are shown in blue with Bologna highlighted (semenda.it, n.d.)

The area of the basin is about 38,000 km^2 and is made up of sediments from the Alps and Apennines. Within the basin, (Carminati and Martinelli, 2002) showed that there are two structural environments: a north-verging Apennine fold-and-thrust belt system buried beneath the Plio–Quaternary layer, and a platform gradually dipping from the Alpine into the basin as shown in Fig. 4.2. They also stated that the principal causes of sedimentation, which has filled the basin with alternate layers of sand and clay, are local tectonics and climatological fluctuations. Gravel is only found near the Apenninic chain in alluvial fan deposits and in foothills fans which lie between the Alps and the Po River, which stretch from the Alpine rivers' discharges into the plain.

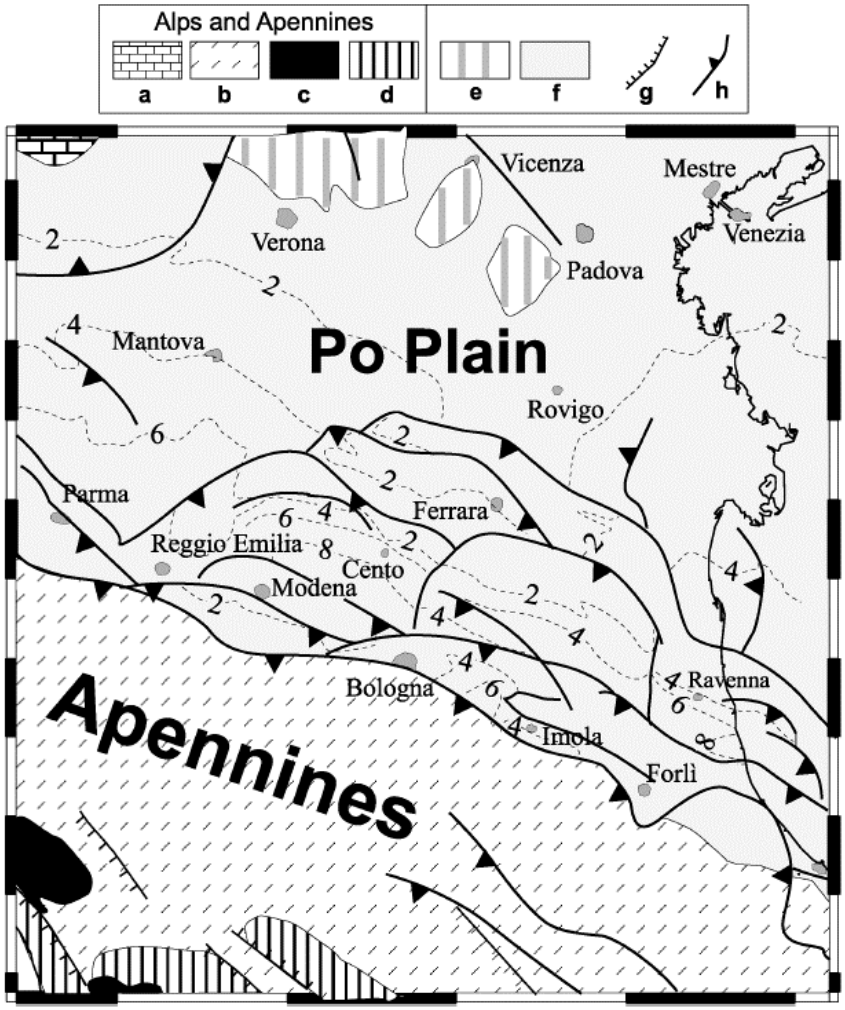

Fig. 4.2. Geological Scheme of the Surface and Subsurface Major Structures (semenda.it, n.d.)

Where (a) Cover units of South Alps; (b) Cover units of the Apennines; (c) Basement and metamorphic apenninic covers; (d) Post-Orogenic sediments; (e) Foreland sediments; (f) Pliocene– Quaternary clastic deposits from the Apenninic and South Alpine foreland basins (dashed lines represent Pliocene depth in kilometers).

The Po Plain is divided into five physiographic units as shown in Fig. 4.3 and stated by (Castaldini et al., 2019), which are described below in stratigraphic sequence:

1- The Holocene deposits in the central block of the basin form the Holocene Floodplain unit, generated by aggradation of the River Po and its right tributaries. The Holocene Floodplain unit is found on the left and right sides of the River Po.
2- Near the Apennine edge of the Po Plain, there is a smaller surface that consists of a set of coalescent fluvial fans emerging in the Apennine foothills, known as the Late Pleistocene bajada unit, which is linked to the massive amount of sediments deposited during the LGM (Last Glacial Maximum).
3- The Main Level of the Plain unit has been located in the northern section of the Po Plain, near to the glacial amphitheatres. It is made up of fluvioglacial and river sediments and has its apex on the Alpine foothill.

4- A sequence of fluvioglacial and fluvial terraces have been included in the Old Terraces unit throughout the Alps and Apennines' margins.
5- The Glacial Amphitheatres unit can be found in the Alps' foothills. This physiographic unit comprises glacier-carved moraines and valleys from the Pleistocene.

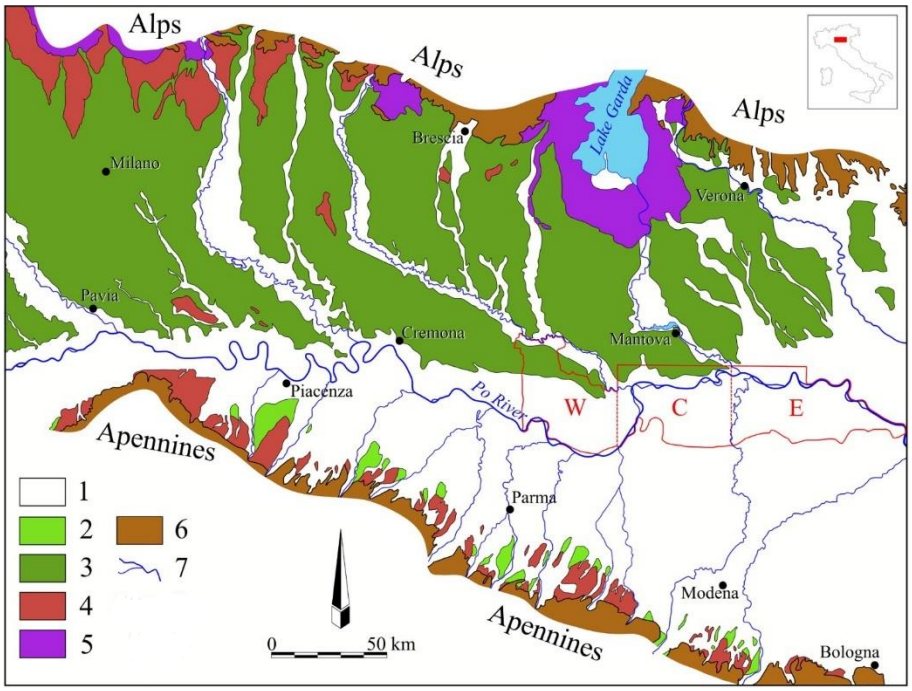

Fig. 4.3. The Po Plain's Physiographic Units (Castaldini et al., 2019)

Where: (1) Holocene Floodplain unit; (2) Late Pleistocene bajada unit; (3) Main Level of the Plain unit; (4) Old Terraces unit; (5) Glacial Amphitheatres unit; (6) Bedrock; (7) Hydrography

The subsident area in which the Po Plain is located is a sedimentary basin filled in its lowest part by sea sediments and more on the surface by river sediments caused by flooding of the rivers that cross the Po Valley, such as the Po and its Alpine and Apennine flows. With regard to the Emilia-Romagna plain, the fluvial sediments have a thickness of several hundred meters; below these deposits are coastal sediments, which are gradually followed by ancient and deeper marine deposits. The deepest area of the Emilia-Romagna plain is affected by active thrusts system generated by compression between the Alps and the Apennines (Farina et al., 2014).

Research conducted to understand the stratigraphic sequence of the depositional units outcropping at the Po Basin included: I) the examination of 30,000 km of seismic reflection profiles given by ENI-AGIP, ii) sedimentological and stratigraphic interpretation of more than 11,000 km of continuously cored boreholes, and iii) logging measurements from roughly 600 boreholes (Amorosi et al., 2004).

Such research has led to the identification of three third-order depositional phases. These phases correspond to the depositional cycles P (middle-late Pliocene) and contains deep sea sedimentations, Qm (Quaternary marine) and represents coastal deposits, and Qc (Quaternary continental) and this one has the fluvial sediments as shown in Fig. 4.4. The Qm

layers are separated from the Qc sediments by a regional unconformity, making the Qc deposits form the Emilia-Romagna Supersynthem. There is also another unconformity that extends laterally within this supersynthem that divides it into two lower-rank synthems, the "*Lower Emilia-Romagna Synthem"* and the "*Upper Emilia-Romagna Synthem"* (Amorosi and Pavesi, n.d.) . Both Qm and Qc stratigraphic units contain aquifer systems, but deeper sediments contain hydrocarbon accumulations.

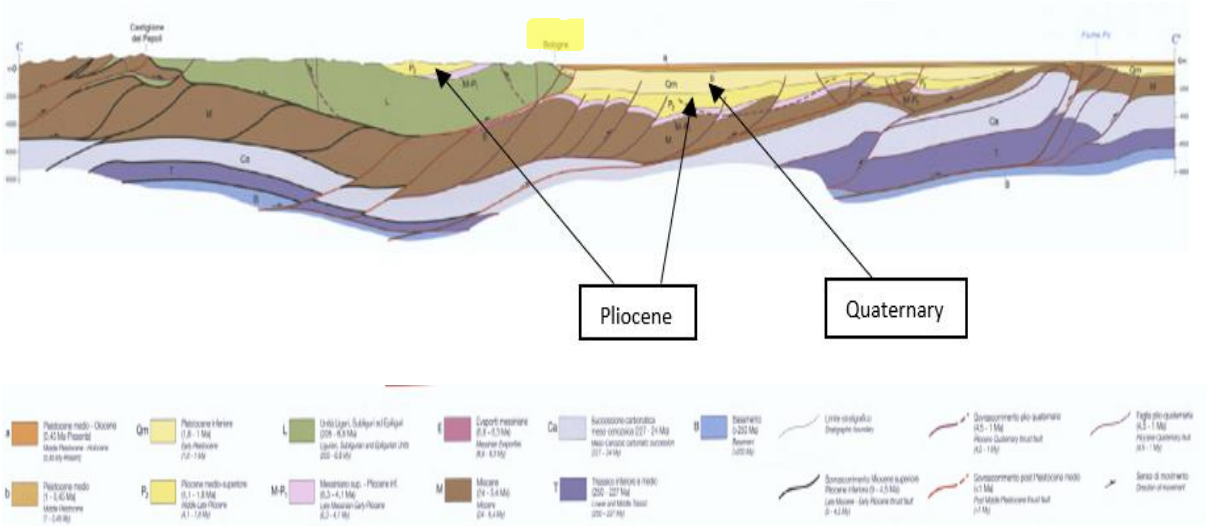

Fig. 4.4. A geological section showing the underground structure of the Po plain in Bologna area (highlighted in yellow) " (Amorosi and Pavesi, n.d.)

4.2 Aquifer System

The Emilia-Romagna plain's aquifers are mostly made up of alluvial deposits in the most superficial region of the plain, with a thickness of around 400-500 m, and, to a lesser extent, marginal marine deposits. The distribution of these sedimentary formations in the subsurface is depicted schematically in Fig. 4.5 by (Marcaccio and Lucchini, 2020) in a stretch that runs from south (sud) to north (nord) across the plain, or from the Apennine margin, which separates the mountain aquifers from those of the plain, to the River Po.

Proceeding from the south to the north of the plain, (Severi and Bonzi, 2012) illustrated that we can see in order: the *alluvial fans*, then the *Apenninic alluvial plain*, and finally the *alluvial and delta plain of the Po*.

(1) The *alluvial fans* are generated by the sediments deposited by the river at the valley's exit, where the water is no longer laterally confined and the topographical slope drops dramatically.
    a. The *proximal fans* are near the edge at the river mouth into the plain and they contain coarse-grained gravels that can even extend in the subsoil to some hundreds of meters. Here fine-grained deposits are scarce.
    b. Going farther into the plain, *distal fans* present which are extensive tabular bodies that consist of fine deposits alternating with buried gravelly deposits.

Alluvial fans, with their permeable and thick deposits, are the primary aquifers of the Emilia-Romagna plain from a hydrogeological standpoint. The proximal fans, in particular, are home to a large groundwater aquifer that is refreshed directly by river and rainwater surface waters, whereas the distant fans are a complex system of multilayer aquifers with confined and semi-confined aquifers.

(2) The *Apenninic alluvial plain* is formed by fine sediments transported by rivers to larger distances. So, it consists of clays, clayey silts, and silty sands alterations. It has a lower topographical slope and it starts when the gravelly bodies join and pass laterally to sands.

We occasionally come across clayey strata rich in organic matter, which testify to a series of Pleistocene sea incursion events that impacted Emilia-coastal Romagna's area, and which serve as true guiding levels.

The aquifers here are of little interest from a hydrogeological standpoint; because the sand deposits are rare and discontinuous and also because the aquifers' recharge is scarce and is solely from water that infiltrates the recharge areas of the fans and flows very slowly to the plain.

(3) Finally to the north comes the *alluvial and delta plain of the Po*, which is made up of a mix of very huge sandy bodies and fine sediments. The sands come from the Po River's sedimentation and are found in layers that have been merged with one another to form layers that are several tens of meters deep and spread for several kilometers. These deposits always have an alluvial origin in the western part of the Region, whereas in the east they represent the different delta systems that the Po created during the Pleistocene. The fine sediments that alternate with the sandy layers are made up of clayey silts, clays, silty sands, and rarely sands. There are also some clayey layers rich in organic content which serve as guide levels in *the alluvial plain of the Po*.

Here the deposits of the *alluvial plain and delta of the Po* are exceptionally permeable and vast, making them major confined aquifers. The most superficial are in direct touch with the river, which recharges them, whereas the deeper ones receive a remote recharge that comes in part from the Po itself (from locations beyond the Emilia-Romagna Region) and in part from the Apennine and Alpine recharging areas, which are located much further south and north, respectively.

Above the pre-described deposits, except for the *proximal fans,* lies the *lowland phreatic aquifer,* a thin layer of mostly fine sediments that extends northwards over the entire plain. These are river channel, embankment, and floodplain deposits that are in direct touch with surface waters and the ecosystems that rely on them, as well as all anthropogenic activity. Due to its fine lithology and the small thickness (in order of 10 m), the *lowland phreatic aquifer* plays a minor role in the resources management on a regional scale. However, it is widely used in rural contexts for domestic purposes.

As shown in Table 4.1 (Amorosi and Pavesi, n.d.), aquifers in the Po plain exist in three groups. The Aquifer Group A is the most recent and is consistent with the “Upper Emilia-Romagna Synthem”, ranging in age from the present to 350,000-450,000 years. It is subdivided into four aquifer systems, named A1, A2, A3, and A4. Then comes the Aquifer Group B, which ranges in age from 350,000 to 450,000 years up to around 650,000 years. This group of aquifers lie in the “Lower Emilia-Romagna Synthem” and it also consists of four aquifer systems, named B1, B2, B3 and B4. Finally, the Aquifer Group C ranges in age from 650,000 to over 3 million years, which in turn is comprised of three aquifer systems; C1, C2, and C3.

Table 4.1. Generalized stratigraphic framework for the Po Basin's Quaternary deposits (Amorosi and Pavesi, n.d.)

<table>
<tr><th>Rieci Lucchi et al., 1982</th><th colspan="4">Regione Emilia-Romagna & ENI-AGIP, 1998</th></tr>
<tr><th rowspan="2">Stratigraphic Unit</th><th colspan="2" rowspan="2">Stratigraphic Unit</th><th rowspan="2">Age (Ma)</th><th colspan="2">Hydrostratigraphic Unit</th></tr>
<tr><th>Aquifer Group</th><th>Aquifer System</th></tr>
<tr><td rowspan="9">Cycle Qc</td><td rowspan="9">Emilia-Romagna Supersynthem</td><td rowspan="4">Upper Emilia-Romagna Synthem</td><td rowspan="4">~0.12</td><td rowspan="4">A</td><td>A1</td></tr>
<tr><td>A2</td></tr>
<tr><td>A3</td></tr>
<tr><td>A4</td></tr>
<tr><td rowspan="5">Lower Emilia-Romagna Synthem</td><td rowspan="5">~0.35-0.45</td><td rowspan="4">B</td><td>B1</td></tr>
<tr><td>B2</td></tr>
<tr><td>B3</td></tr>
<tr><td>B4</td></tr>
<tr><td rowspan="3">Cycle Qm</td><td colspan="2" rowspan="3"></td><td rowspan="3">~0.80</td><td rowspan="3">C</td><td>C1</td></tr>
<tr><td>C2</td></tr>
<tr><td>C3</td></tr>
</table>

The Upper Emilia-Romagna Synthem's stratigraphic architecture exhibits unique cyclic variations in lithofacies and channel stacking patterns in river deposits, allowing them to be divided into *transgressive-regressive (T-R) phases*. Each sequence starts with silt-clay overbank deposits with thin and lenticular fluvial-channel sands, then progresses upward to laterally extensive fluvial-channel sand masses. The fluvial bodies in the regressive phase of T-R sequences reflect the primary aquifer systems, while the overbank fines serve as the

most critical permeability barriers. It extends down to about 350 m below sea level for the Bologna case.

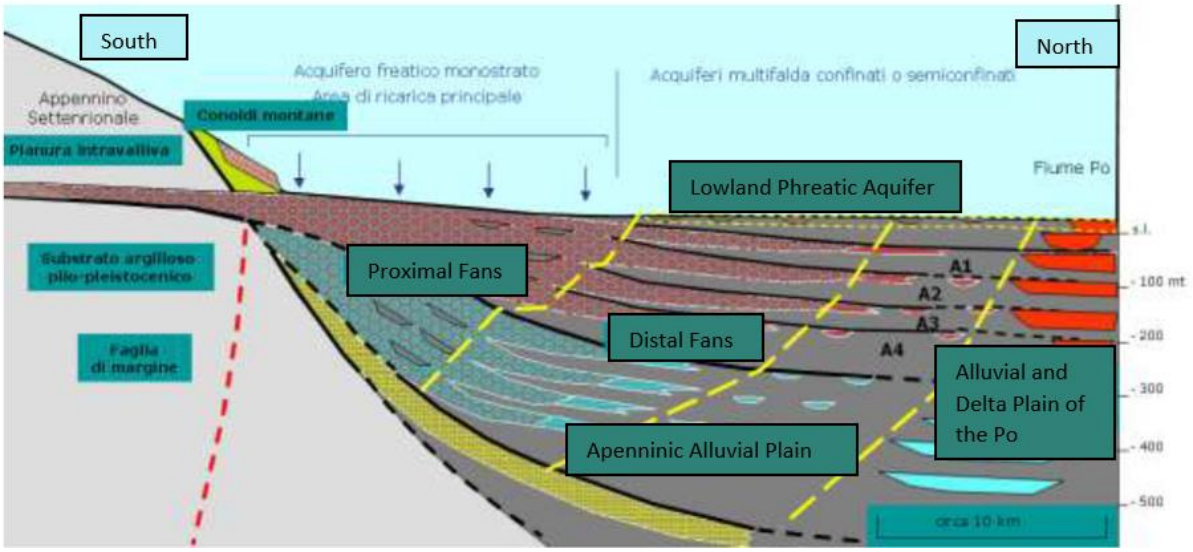

Fig. 4.5. Schematic geological section of the Emilia-Romagna Plain with the locations of the aquifer bodies

The aquifers, in fact, extend over large areas, as shown in Fig. 4.6. (Arpae, n.d.). For the area of this research, we focus on the water body named (Pianura Alluvionali Appenninica – Acquifero Confinato Superiore), which is the shallowest confined aquifer that lies in the Apennines alluvial plain.

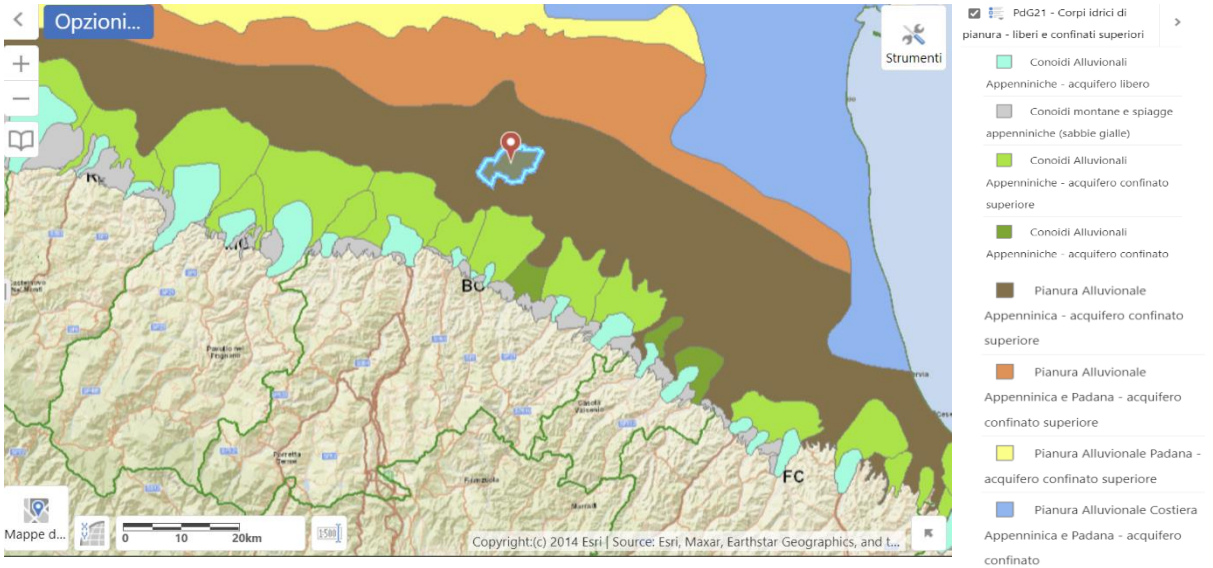

Fig. 4.6. Underground Water Bodies with Large Areal Extension (Arpae, n.d.)

5 Dataset Analysis

In this chapter, the dataset required for the fluid flow simulation and the mechanical simulation are discussed.

5.1 Aquifers and Aquitards Properties

As stated in the geological study, there exist sandy aquifers separated by impervious clayey layers in the Emilia-Romagna Po Plain. In Bologna, the research geographical area, data were collected regarding the aquifers and the aquitards. These data are based on the work done by (Gambolati, 1998). In this book he established a large database of geological, hydrological, and mechanical properties of sediments from the ground surface to the depths of the lowest reservoirs. He set this data based on soil samples retrieved from deep and shallow boreholes strewn across the Po river plain that have been subjected to a number of laboratory examinations. Some of these data were provided by AGIP, while others came from the Committee for the Study of Subsidence in Ravenna and were collected by them. Fig. 5.1. indicate the locations of the oil/gas reservoirs used in his study.

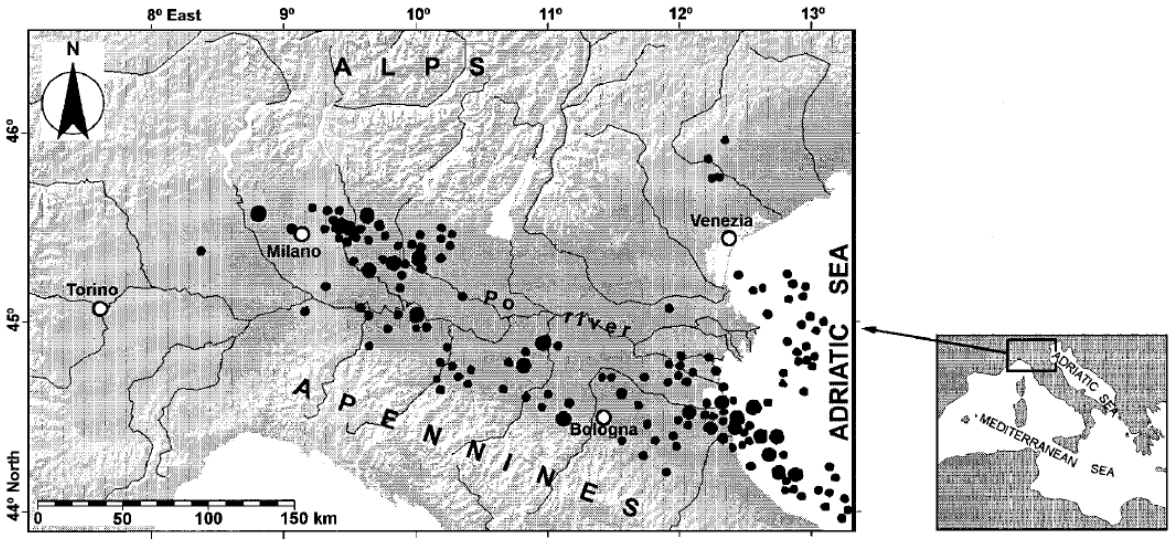

Fig. 5.1. The Po Plain with the Solid Circles Indicating the Locations of Oil/Gas Fields. Large Circles Ensemble Reserves with more than 3.5 Mtep (Millions of Equivalent Oil Tons) (Gambolati, 1998)

Then, Gambolati used the data collected to simulate the subsidence process in Ravenna. His study area is shown in Fig. 5.2.

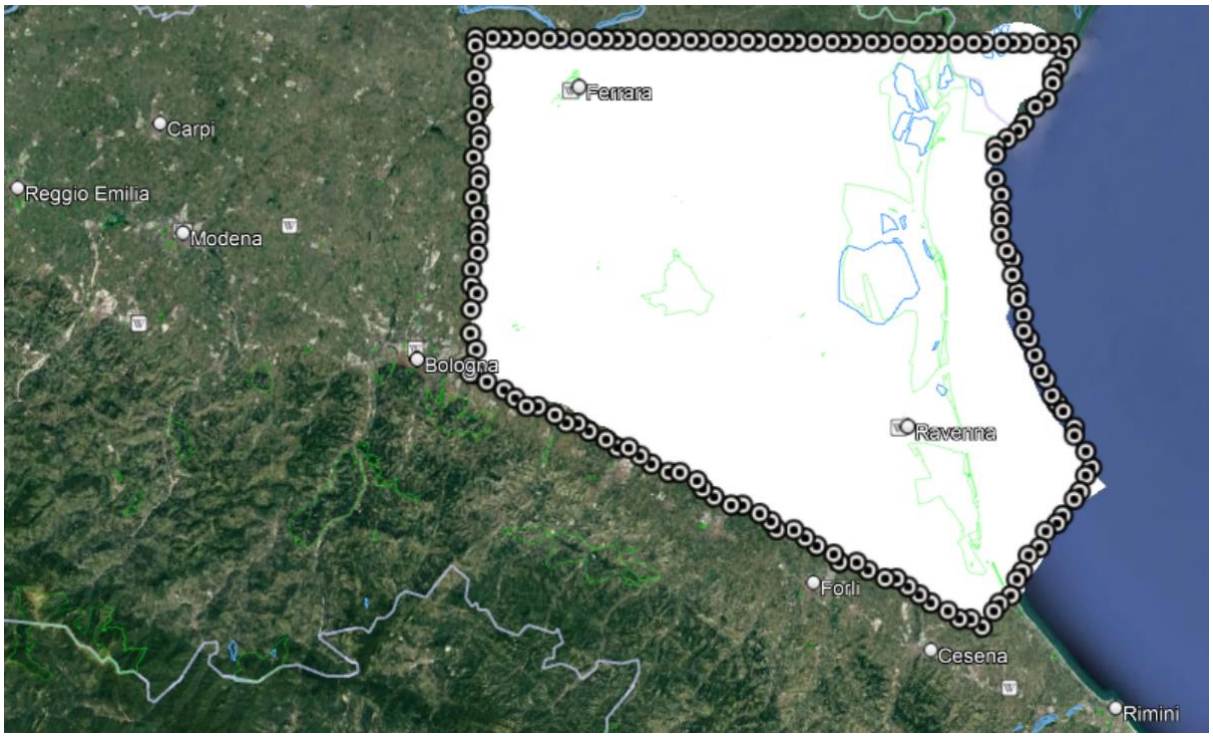

Fig. 5.2. Area of Gambolati's Work

Also, (Modoni et al., 2008) has worked on subsidence in Bologna. He focused his research on the uppermost aquifer group (A), which is thought to be the primary cause of observed subsidence due to its vast overall thickness and lower starting overburden stresses (Spacagna et al., 2020). Fig. 5.3. (Spacagna et al., 2020) shows the study area in which Modoni has done his studies.

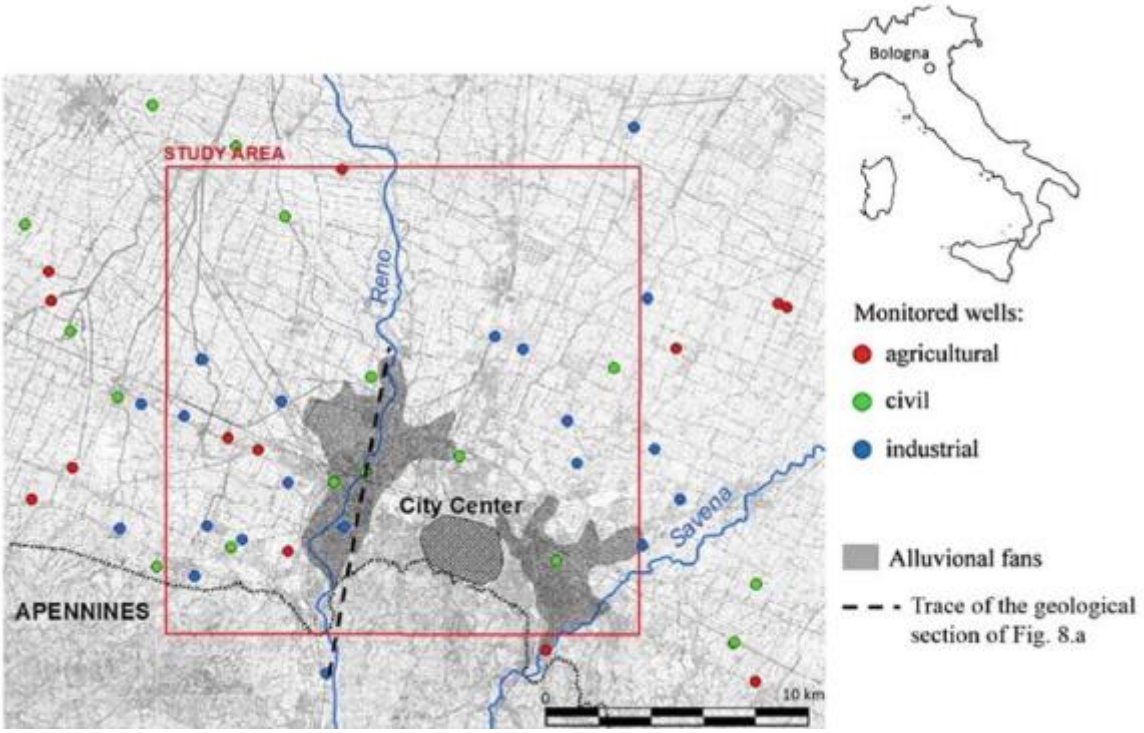

Fig. 5.3. Modoni's Study Area (Modoni et al., 2008)

5.1.1 Properties of Aquifer Layers

Aquifers are made up of coarse-grained deposits which have high hydraulic conductivity, so they are useful for water exploitation.

5.1.1.1 Density and Hydraulic Conductivity

a. Sand density was set to be 1.9 g/cm^3.
b. Table 5.1 (Teatini et al., 2006) shows the hydraulic conductivity of the aquifers based on the interpretation of pumping tests available in the area. These pumping tests have been conducted using about 250 wells and they were analysed with Theis-Jacob method. He also stated that the *anisotropy ratio* (K_h / K_v), where K_h is the horizontal hydraulic conductivity and K_v is the vertical component of the hydraulic conductivity, is about 10. It is also worth mentioning that he further subdivided the aquifers A1 and A2 into two sub-layers named A1.1, A1.2, and A2.1 A2.2, respectively.

Table 5.1. Hydraulic Conductivity of Some of the Emilia-Romagna Aquifers (Teatini et al., 2006)

Aquifer	Hydraulic Conductivity, m/s	
	Maximum	Minimum
A1.1	2.00E-03	2.00E-05
A1.2	3.00E-04	2.00E-05
A2.1	2.00E-03	2.00E-06
A2.2	1.00E-03	4.00E-06
A3	2.00E-03	1.00E-05
A4	7.00E-04	2.00E-05
B1	1.00E-03	1.00E-06

(Modoni et al., 2008) also set the hydraulic conductivity for the aquifer group A to be between 10^{-3} and 10^{-5} m/s, which is in the same range as the table above.

5.1.1.2 Compressibility and Young's Modulus

As discussed in section 3.4.2, uniaxial vertical compressibility c_M is a significant parameter to model land subsidence due to fluid withdrawal.

For relatively shallow formations ($z < 1000\ m$), as the depths encountered in this study, (Teatini et al., 2006) shows that c_M depends on:

1- The effective stress σ'_z: As the effective stress increases, compressibility decreases. Effective stress increases with depth and with excessive drawdown.
2- The loading conditions: As discussed in 3.4.1, when the preconsolidation stress σ'_p, the maximum stress ever-experienced by the porous medium, is reached, the

compression is inelastic, while the compression is elastic when the stress is lower than σ_p' and it is in the unloading-reloading region.

3- Lithology: Clay is up to two orders of magnitude more compressible than sand, especially in shallow rocks.

(Teatini et al., 2006) also could establish a relationship for the compressibility of sandy layers as follows:

For $Z < 1000\ m$: $c_M = 0.43Z^{-1.013}$ *(5.1)*

For $Z > 1000\ m$: $c_M = 29.2Z^{-(1/0.62)}$ *(5.2)*

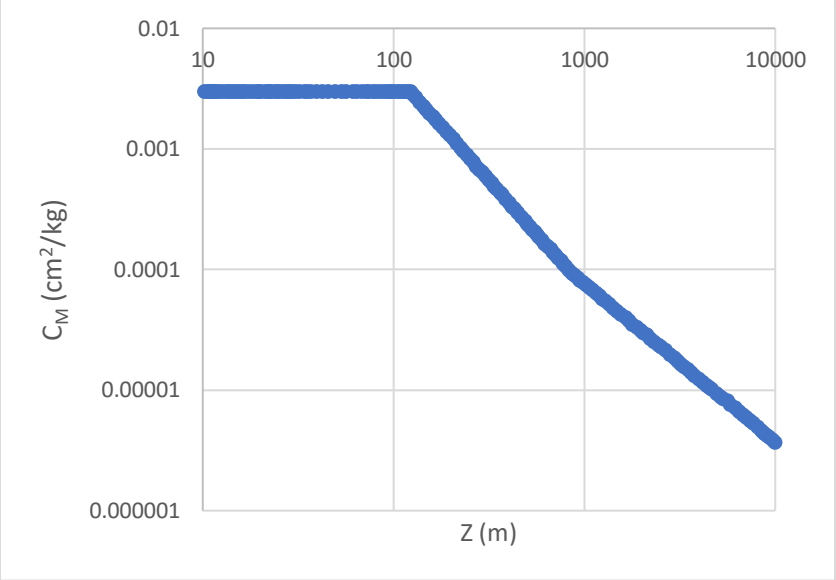

Fig. 5.4. Vertical Compressibility vs. Depth for Aquifers (after (Gambolati et al., 2000))

There are also two considerations to be taken into account as showed by (Teatini et al., 2006),

1- *The in-situ measurements yield a sand compressibility that is 5 to 10 times lower than the lab c_M shown in Fig. 5.4*, which is consistent with recent findings that laboratory testing overestimate the actual c_M due to sample disruption during coring, transit, and handling. So, they suggested to decrease the c_M values by one order while performing the simulation studies.

2- Fig. 5.4 shows the c_M profiles for rock compression under *virgin loading (inelastic) circumstances*. However, they set r to be *the ratio between the loading (inelastic) and the unloading-reloading c_M*. They also mentioned that the value of r is about 3 at $Z = 1000\ m$ as shown by an analysis conducted by ENI E&P. Then, *they assumed the value of r to be 10 for shallower depths.*

So, in our depths of interest, *c_M is constant and equals 0.003 cm^2/kg, which corresponds to 3.058 bar^{-1}.*

Young's modulus is related to the vertical compressibility through the equation (3.38), then in the first 100 m *Young's modulus is equal to 24.28313 MPa.*

5.1.1.3 Porosity

(Teatini et al., 2006) also showed the relationship between the porosity of the sandy layers that make up the aquifers and the depth.

Fig. 5.5 shows such relationship. As can be seen, porosity decreases with depth from about 0.34 near the ground surface ($Z = 10\ m$) and decreases down to about 0.27 at the bedrock depth (10,000 m).

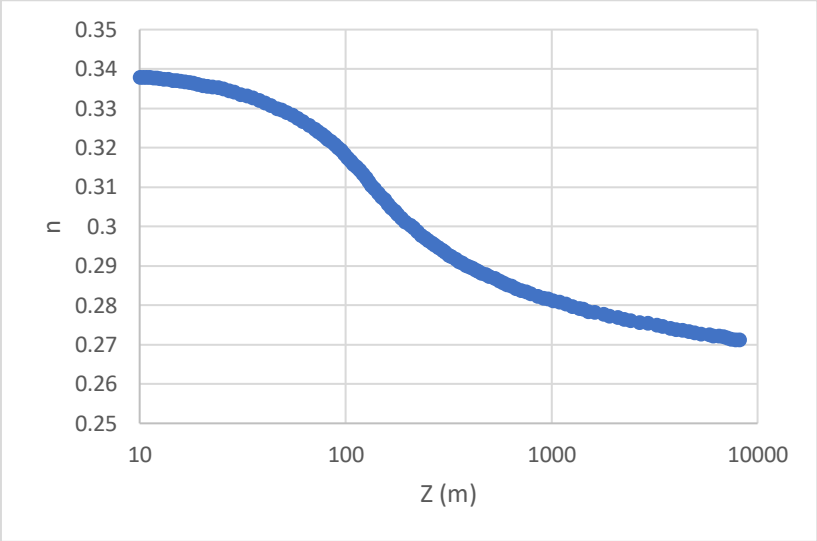

Fig. 5.5. Porosity vs. Depth for Sandy Layers (after (Gambolati et al., 2000))

5.1.2 Aquitard Properties

Aquitards are made up of fine-grained deposits like clays which have low hydraulic conductivity, so they act as the impervious barrier to prevent water escape.

5.1.2.1 Density and Hydraulic Conductivity

a. Clay's density of 1.9 g/cc was used.
b. Table 5.2 (Teatini et al., 2006) shows the hydraulic conductivity for the clay layers that make up the aquitards. It is seen that the hydraulic conductivity of clays is so low compared to that of sand.

Table 5.2. Hydraulic Conductivity of the Aquitards (Teatini et al., 2006)

	Hydraulic Conductivity, m/s	
	Maximum	Minimum
Aquitards	1.00E-09	1.00E-11

5.1.2.2 Compressibility

(Teatini et al., 2006) also provided the uniaxial vertical compressibility c_M for aquitards. They also expressed the Fig. 5.6 in a set of equations:

$$\text{For } Z < 1000\ m\text{:}\ \ c_M = 1.533Z^{-1.175} \qquad (5.3)$$

$$\text{For } Z > 1000\ m\text{:}\ \ c_M = 29.2Z^{-(1/0.62)} \qquad (5.4)$$

By comparing the compressibility of aquitards to that of sands, we can see that clays have higher compressibility at shallow depths and then at depths higher than 1000 meters, both deposits express the same compresibilties.

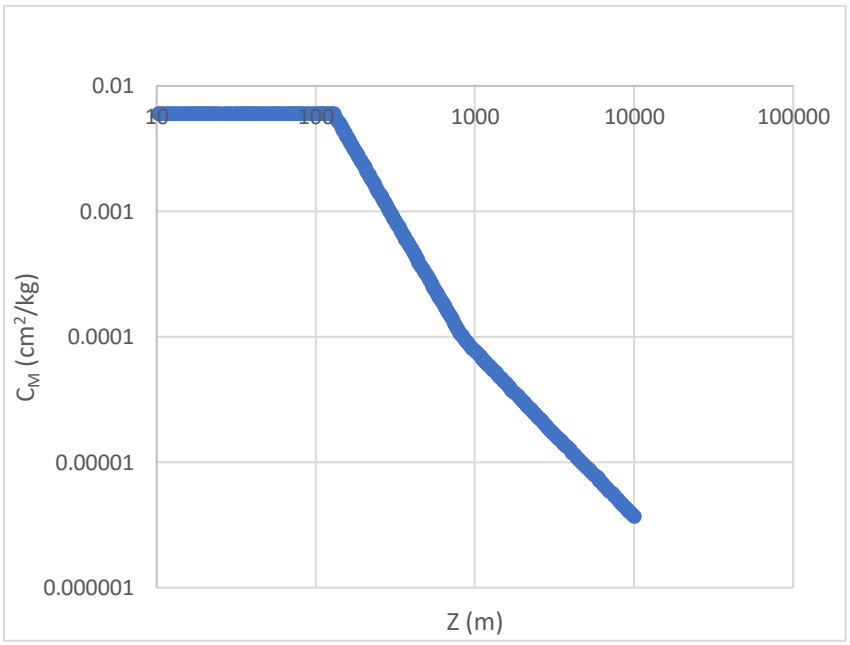

Fig. 5.6. Clays Vertical Compressibility vs. Depth (after (Gambolati et al., 2000))

For the clays, also the same considerations mentioned for the sand in section 5.1.1.2 apply also for the clay layers.

So, in our depths of interest, *c_M is constant and equals 0.006 cm^2/kg, which corresponds to 6.116 bar^{-1}.*

Young's modulus is related to the vertical compressibility through the equation (3.38), then in the first 100 m *Young's modulus is equal to 12.14157 MPa.*

Moreover, (Modoni et al., 2008) set some values for the aquitards that exist in aquifer group A as shown in

Table 5.3. Compressibility and Swelling Coefficients for Aquitards (Modoni et al., 2008)

	λ	κ
Average	0.12	0.03
St. Dev.	0.036	0.015

(Spacagna et al., 2020) also mentioned that OCR (Over-Consolidation Ratio) values estimated by oedometer tests reveal values equal to roughly six near the ground level dropping to one at about 20 m underground, which is typical of overconsolidation caused by water table fluctuation. So, the values are assumed to be normally consolidated.

They also showed the mean values and the standard deviation (CoV) of the compression and swelling indices for the $e - \log \sigma_z'$ curve as follows:

Table 5.4. Compression and Swelling Indices for Fine-Grained Deposits

	C_c		C_s	
	Mean	CoV	Mean	CoV
Shallow (0-30 m)	0.25	0.27	0.07	0.41
Deep (0-300 m)	0.35	0.35	0.07	0.61

With reference to equations (3.35) and (3.36), we can see that this applies for the values from the tables Table 5.3 and Table 5.4

5.1.2.3 Porosity

As shown in Fig. 5.7 (Gambolati et al., 2000), porosity of clays decreases with depth from about 0.38 near the ground surface (at 10 m) down to about 0.27 at the bedrock depth (10 kilometers). It should also be noted that clays have higher porosities than sands. However, they act as sealing layers for aquifers because of their much lower hydraulic conductivity.

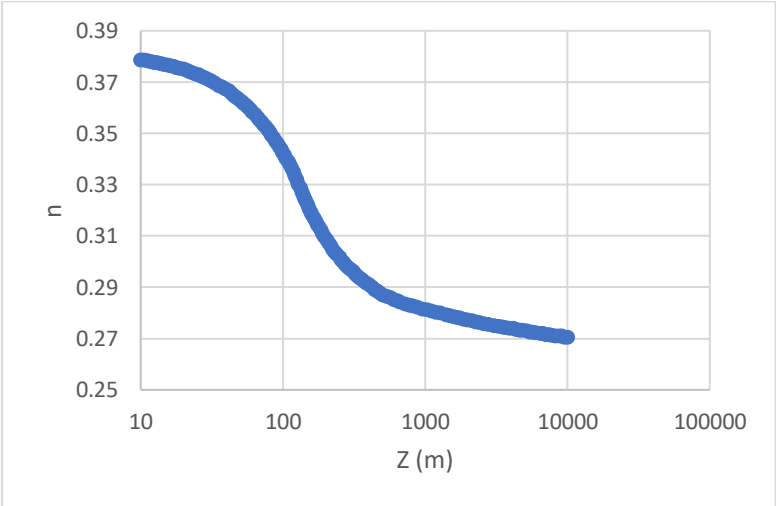

Fig. 5.7. Porosity vs. Depth for Clays (after (Gambolati et al., 2000))

5.1.3 Biot Coefficient

Reference to Biot's work discussed in section 3.3, Biot coefficient is the parameter that differentiates soils from rocks.

Based on the work of (Gambolati et al., 2000) shown in Fig. 5.8, we can notice that Biot coefficient is equal to one in the first 900 meters, then starts to decrease.

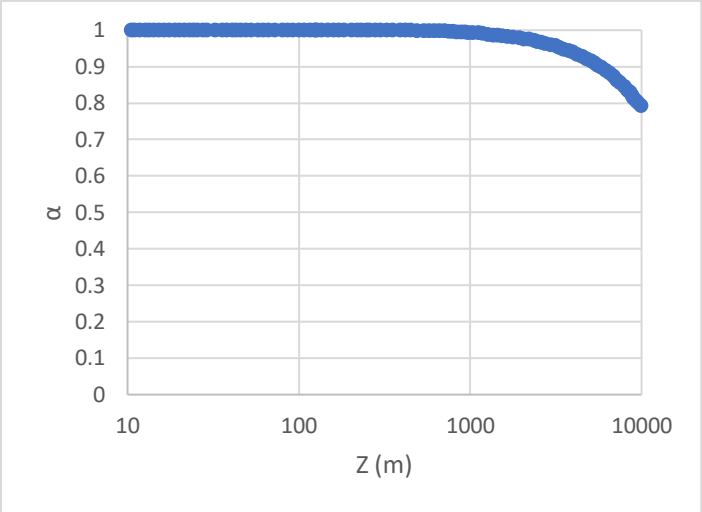

Fig. 5.8. Biot Coefficient (after (Gambolati et al., 2000))

5.1.4 Water Compressibility

As shown by (Gambolati et al., 2000), water compressibility, β, is almost constant in the range of depths of our interest. It is equal to 8×10^{-5} cm^2/kg, which corresponds to about 5.6×10^{-6} psi^{-1}. Note that in the range of depths of our interest, water compressibility is lower than that of both sand and clay.

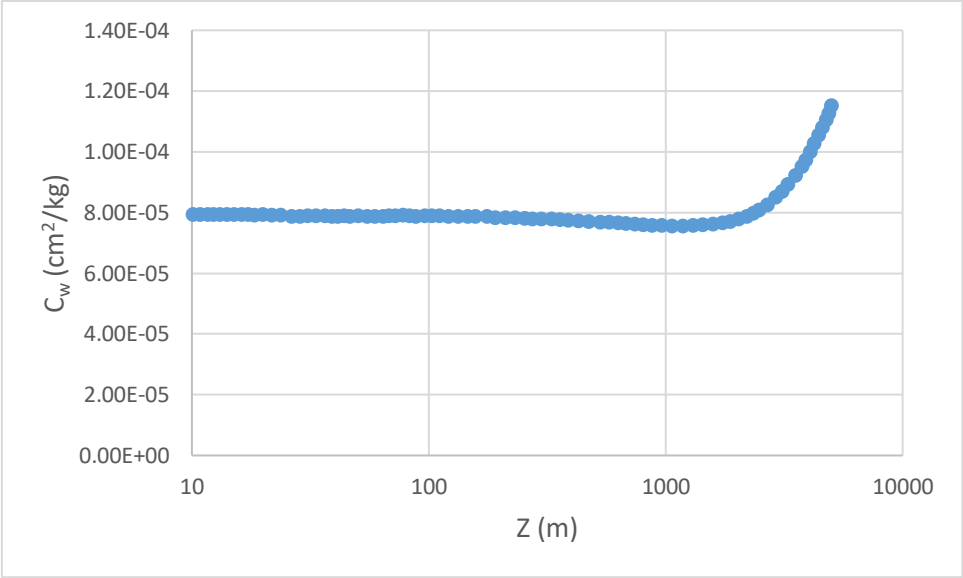

Fig. 5.9. Water Compressibility (after (Gambolati et al., 2000))

5.2 Groundwater Withdrawal

The water withdrawal data for the study area were available from years 2003 to 2018, with missing years in between. It is illustrated in Table 5.5.

Table 5.5. Water Flowrate in the Study Area

	Year(s)

	2003	2009-2011	2015-2018
Flowrate (*1000 m^3/yr)	1,236	1,266	633

According to that table, the flow rate continued to be about 1.23 million of m^3/year or slightly above this for nine years, from 2003 to 2011, then dropped abruptly in the following years until it stabilized at about half that value, more than 600 thousand m^3/year in 2015 and the subsequent years.

So, while performing the simulation, it was assumed that the years in between, from 2012 to 2014, the yearly water flow rate was in between these two extremes.

Water Table Level Data

Water table level is the distance between the ground level to the aquifer, measured in meters, increasing downward.

Data regarding the water table level were used to estimate the pressure of the aquifer.

These data included three sub-categories

a- Temporal Evolution for the Confined Superior Aquifer in Emilia Romagna
b- Regional maps from which an average water table level of the study area was estimated
c- Water Table Level Temporal Evolution of the Confined Superior Aquifer: Punctual Readings at wellbore

5.2.1 Temporal Evolution for the Confined Superior Aquifer in Emilia Romagna

As mentioned, to get the water table level, ("Livello delle acque sotterranee," n.d.) offers the yearly-averaged data for the water table level for the confined aquifers of Emilia-Romagn. The data are displayed in displayed in Fig. 5.10. It shows also the temporal evolution throughout the year seasons. Because the water table level fluctuates with both production and recharge. As it shows, the water table level followed an increasing trend due to the decreased water discharge in the last decades (Benetatos et al., 2020). However, it shows a sharp decrease in 2017 because there was a drought that year. Also, it is evident that the water table level is higher in the spring (primavera) than in the autumn (autunno)

due to the recharge.

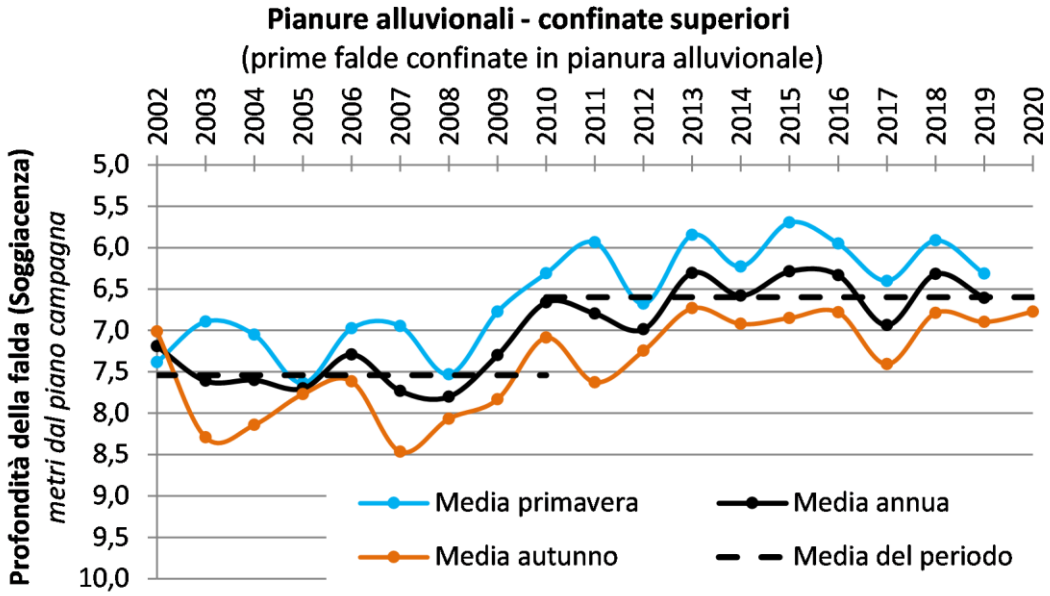

Fig. 5.10. Water Table Level in 2002-2020 for Emilia-Romagna for the (Pianura-Alluvionale-Confinate Superiori) , ("Livello delle acque sotterranee," n.d.)

5.2.2 Water Table Level of the Study Area

Then, to get a closer look on the investigation area, the groundwater table level values for Emilia-Romagna were used. There are 535 stations that measure the properties of the confined superior aquifers in Emilia-Romagna, as shown in Fig. 5.11. ("La rete di monitoraggio," n.d.). Then, ("Livello delle acque sotterranee," n.d.), in figures from Fig. 5.12. to Fig. 5.17. gives an idea about the evolution of the water table level through almost a decade -from 2010 to 2018.

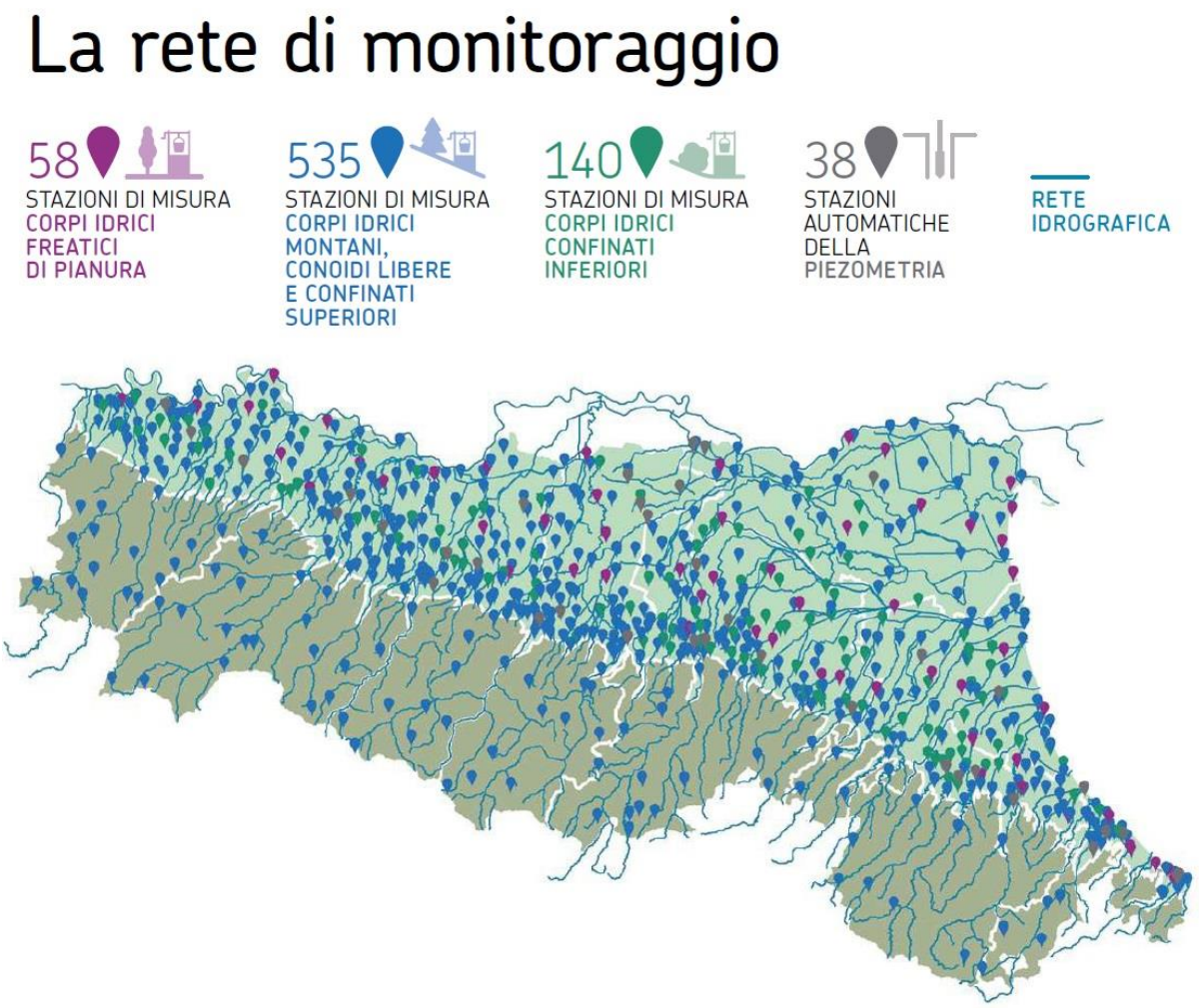

Fig. 5.11. Wells Used for Monitoring Aquifers ("La rete di monitoraggio," n.d.)

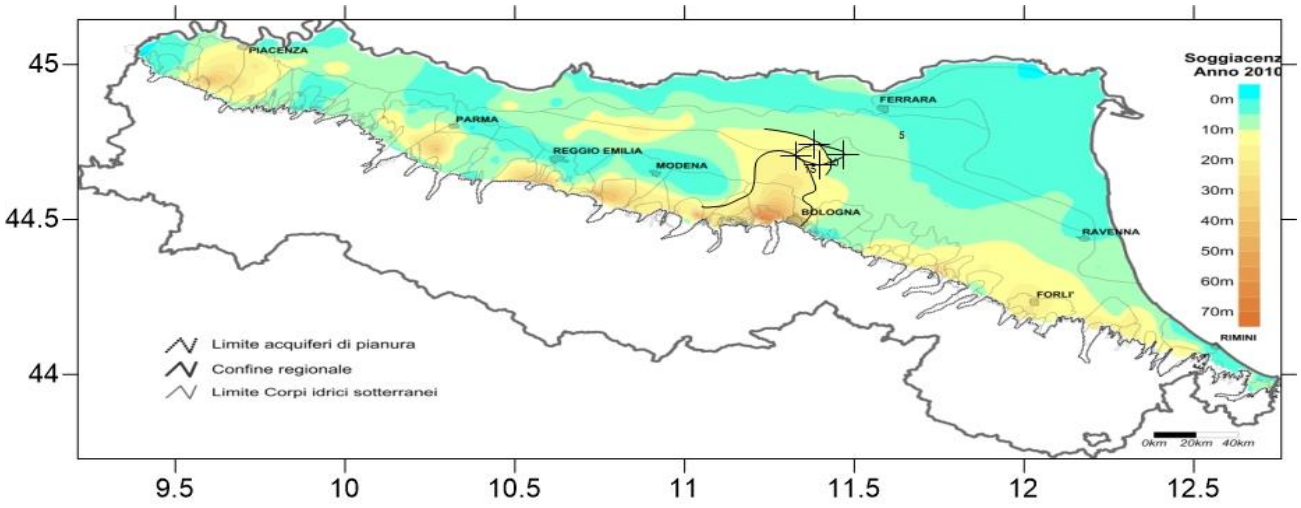

Fig. 5.12. Average Water Table Level Value in 2010 ("Livello delle acque sotterranee," n.d.)

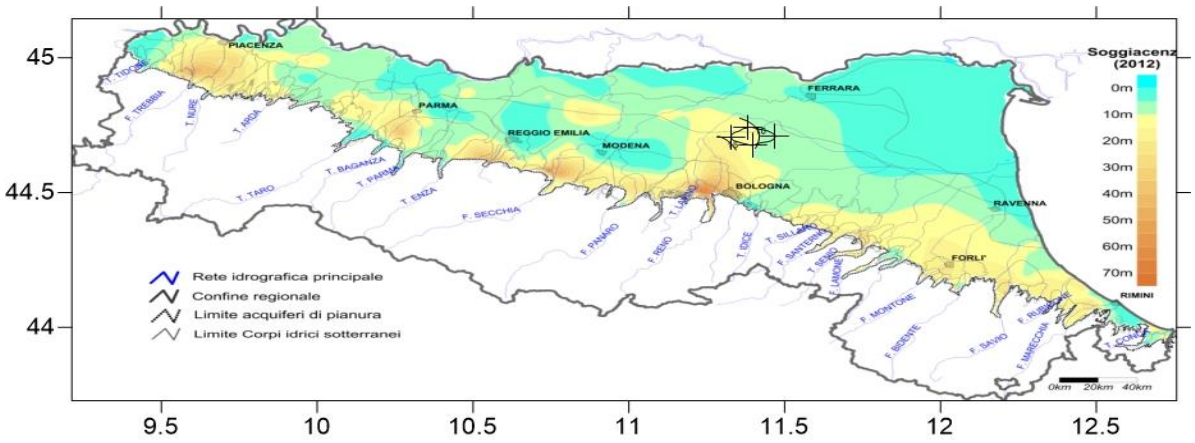

Fig. 5.13. Average Water Table Level Value in 2012 ("Livello delle acque sotterranee," n.d.)

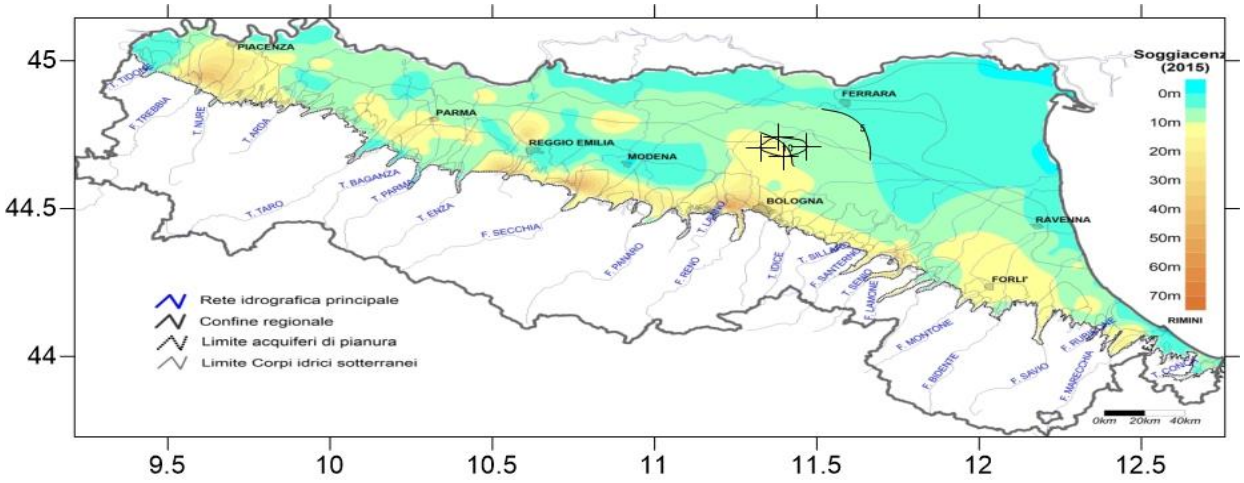

Fig. 5.14. Average Water Table Level Value in 2015 ("Livello delle acque sotterranee," n.d.)

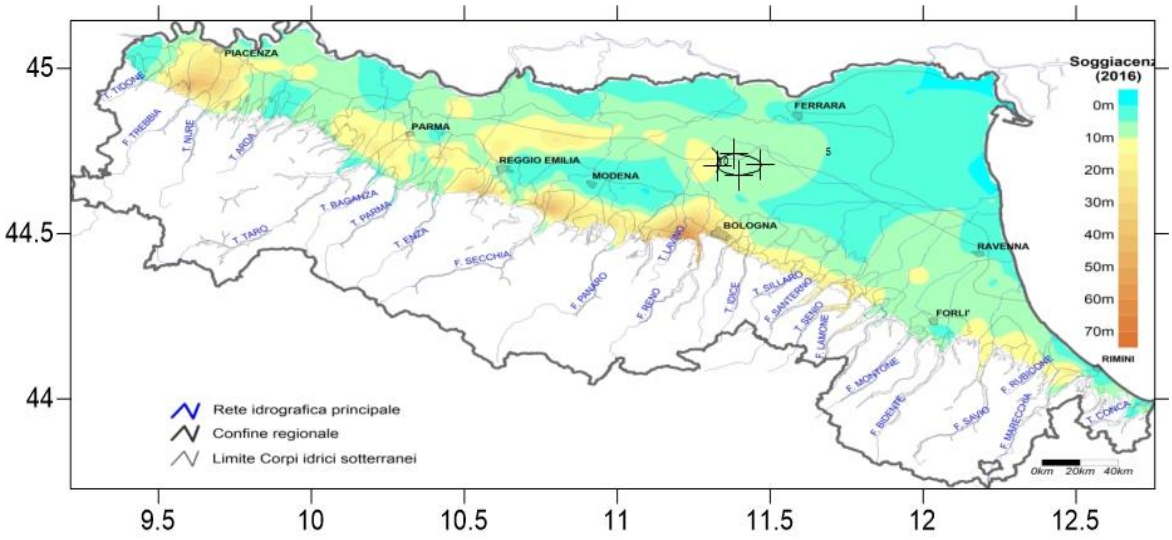

Fig. 5.15. Average Water Table Level Value in 2016 ("Livello delle acque sotterranee," n.d.)

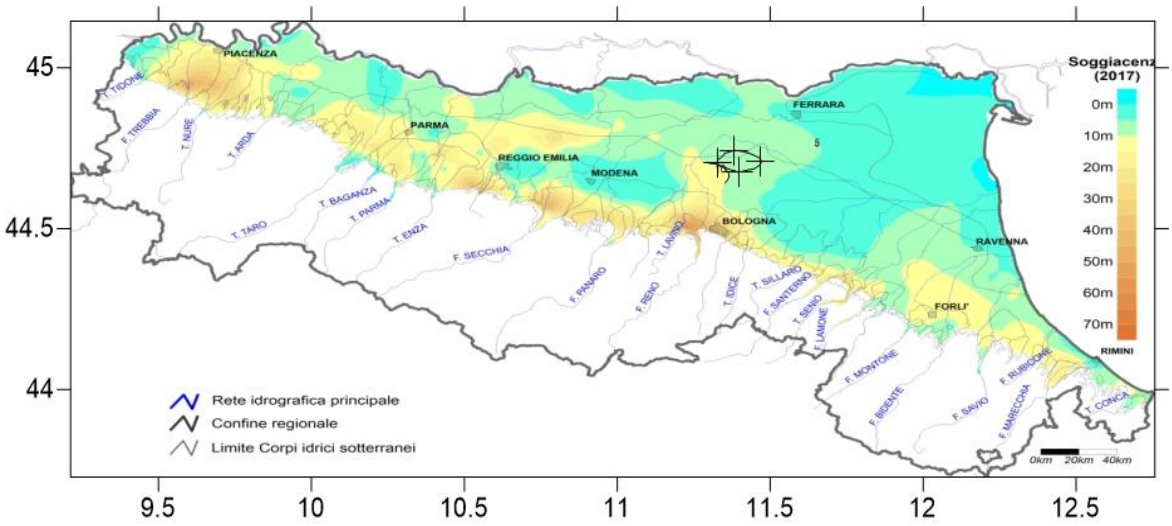

Fig. 5.16. Average Water Table Level in 2017 ("Livello delle acque sotterranee," n.d.)

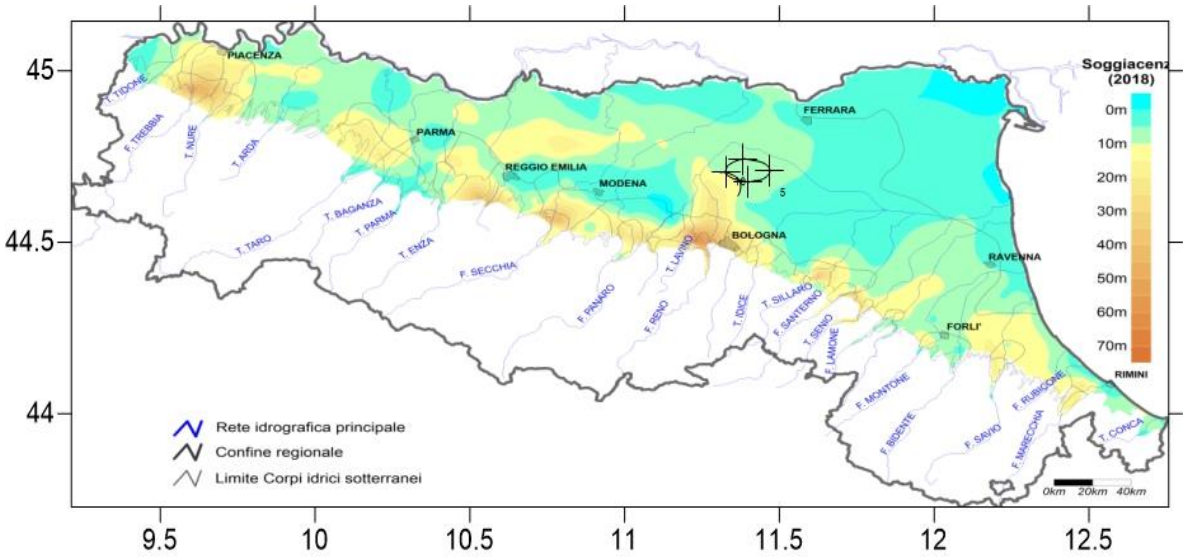

Fig. 5.17. Average Water Table Level in 2018 ("Livello delle acque sotterranee," n.d.)

From these graphs, the water table level was estimated for the study area. One average reference value was estimate for each available year The results are shown in Table 5.6.

Table 5.6. Water Table Level of the Study Area Estimated from the Maps

Year	2010	2012	2015	2016	2017	2018
Water Table Level (m)	11.96	11.46	10	8.25	8.80	8.89

This table can be represented in Fig. 5.18.

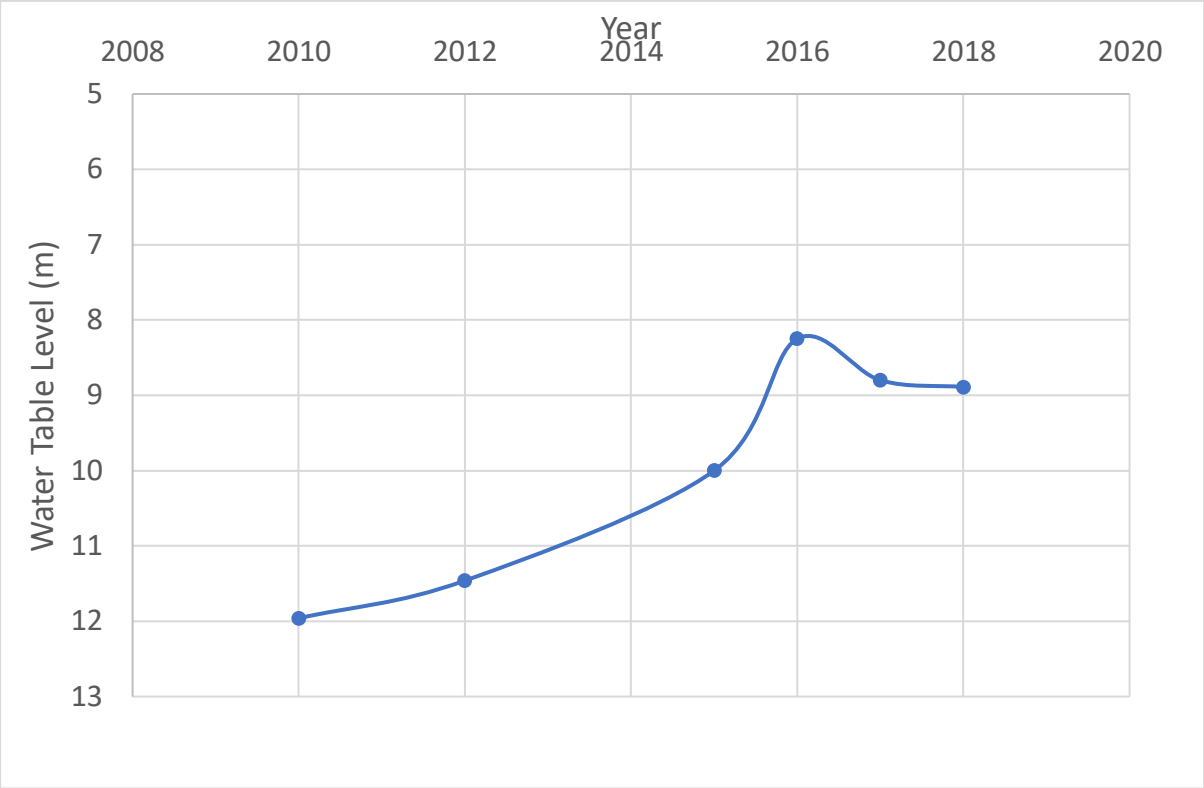

Fig. 5.18. Temporal Evolution of the Water Table Level in the Study Area from 2010 to 2018

As can be seen from the table and the graph, the water table level followed an increasing trend from 2010 to 2016, then again dropped due to the drought that has occurred in 2017, giving rise to a sudden decline in the water table level, until it again stabilized in 2018.

To have a clearer understanding of the trend, average values of Emilia-Romagna discussed in 5.2.1 and 5.2.2 were put together in Fig. 5.19.

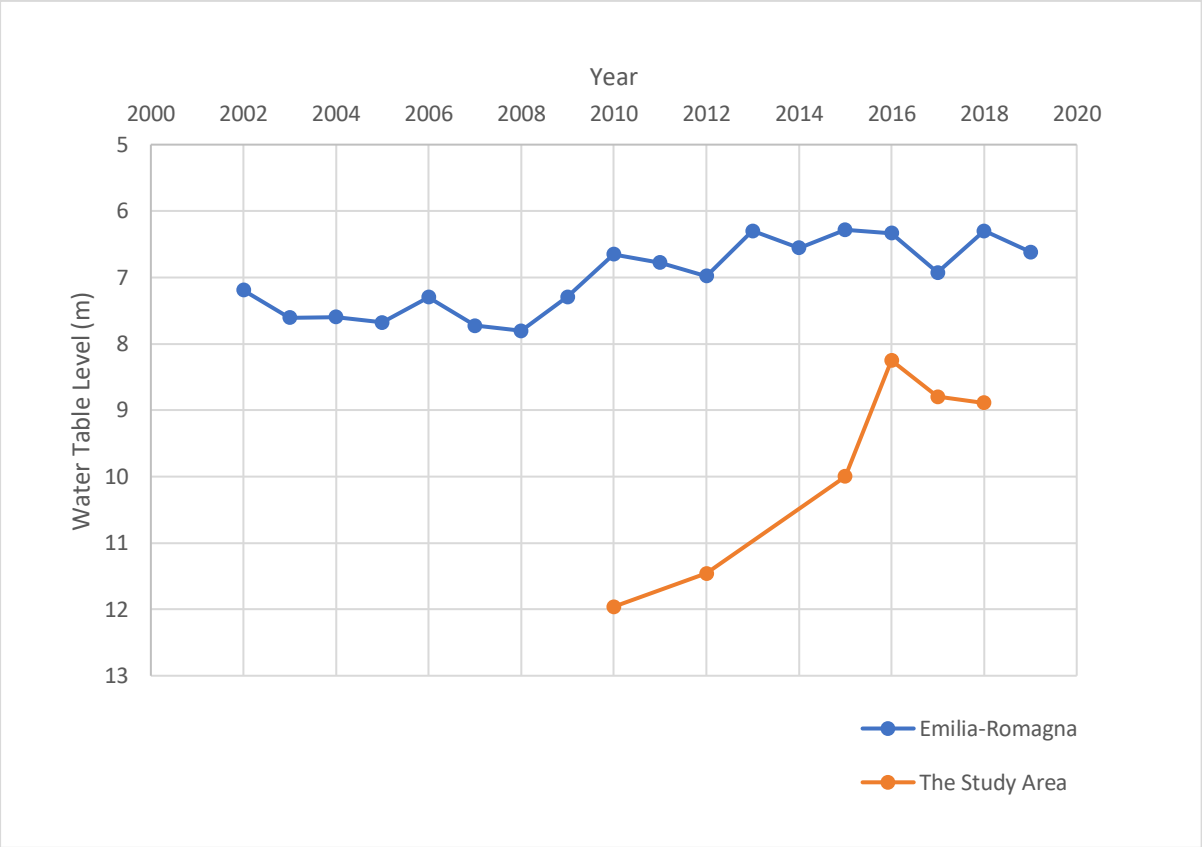

Fig. 5.19. Yearly Average of Water Table Level Evolution

5.2.3 Water Table Level Temporal Evolution of the Confined Superior Aquifer: Punctual Readings

Two wells used for industrial use, named BO03-01 and BO23-01, described in Table 5.7 and Table 5.8, were used to provide punctual readings of the water table level from 2002 to mid-2016. Both of these wells extract from the confined superior aquifers of the group A aquifers, which made them relevant to the scope of this research. Well BO03-01 extends down to 205 meters and exploits water from aquifer groups A1, A2, A3, and A4. Then, well B023-01 extracts water from the aquifers A1 and A2 and has a depth of 115 meters. Several sources from Arpae and the Emilia-Romagna geoportal were used for the purpose of collecting the water table level data.

Table 5.7. Well BO03-01 Characteristics (semenda.it, n.d.)

CODICE	**BO03-01**
COMUNE	**SAN PIETRO IN CASALE**
SIGLA_PROV	**BO**
PROFONDITA	**205**
ACQUIFERO	**A2,A3,A4**
TIPO_MISURA	**Analisi chimica e Livello piezometrico**
PROPRIETA_DATO	**Servizio Tutela e Risanamento Risorsa Acqua - Regione Emilia-Romagna**
GESTORE_DATO	**ARPA - Agenzia Regionale Prevenzione e Ambiente - Regione Emilia-Romagna**

USO	**Industriale**
DATA_INIZIO	**07-MAG-2002**

Table 5.8. Well BO23-01 Characteristics (semenda.it, n.d.)

Code	PB23-01
Name of the Database	Emilia-Romagna Region (Italy)
Depth of the well	115.0 meters
Share of the campaign plan	15.85 meters
Acquifero	A1, A2
Reference level	Average Adriatic Sea Level
Reference system	Coordinates UTM 32 Nord (Datum ED50)
X-coordinate	692344
Y Coordinate	4944360
Managing body	Water Resource Protection and Rehabilitation Service - Emilia-Romagna Region
Responsible body	ARPA - Regional Agency for Prevention and Environment - Emilia-Romagna Region
Use	Industrial
Date of first measure	12/05/1988

One well, BO03-01, is located inside the study are and the other one, B023-01, is only about five kilometers apart from the investigation area, as shown in Fig. 5.20.

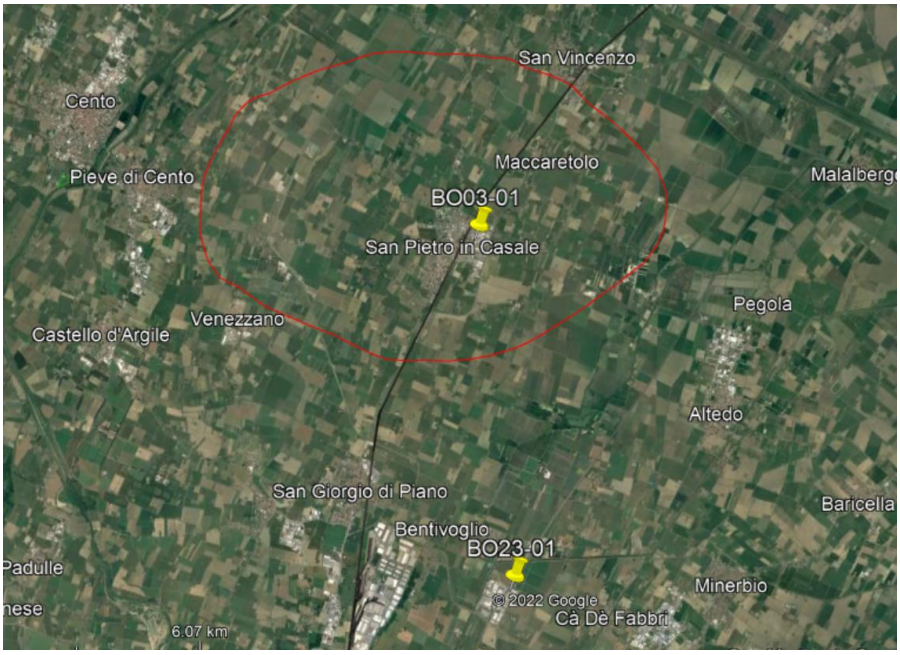

Fig. 5.20. Location of the Two Wells Selected for Punctual Readings

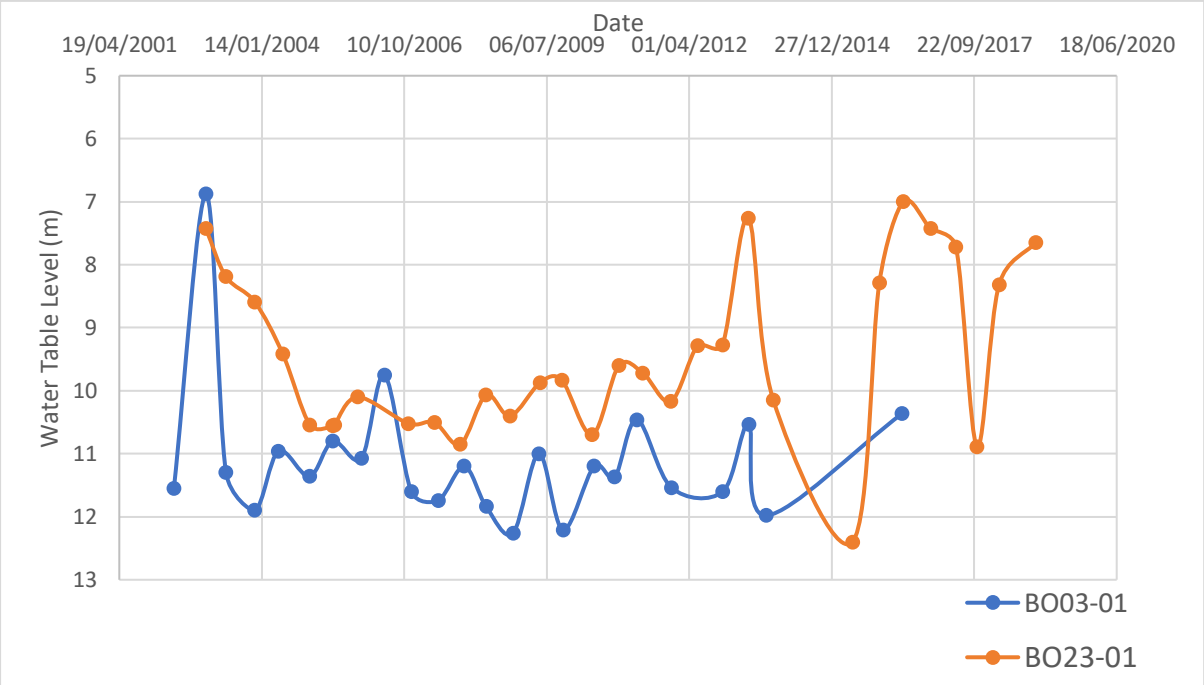

Fig. 5.21. Punctual Readings of the Waer Table Level

At the beginning, the well BO03-01 showed a sharp increase followed by a sharp decrease in the water table level, which is thought to be not representative of the actual behavior. However, it may be attributed to a some kind of a flood or stopping the production from nearby wells. As mentioned earlier, there are about 535 wells in Emilia-Romagna, so the wells can affect each other in readings. However, the two wells follow almost the same trend for most of the years. Then, again, an erroneous decrease followed directly by a sharp increase for the well BO03-01., which also can be illustrated as an error in the reading of May, 2005 or also a some effects from nearby wells, or finally due to a major drought, which is unlikely because the other well follows the opposite trend for that period of time.

Finally, to get a comprehensive look on the temporal evolution of the water table level data, Fig. 5.22 shows the water table level data for Emilia Romagna, Study area, and the punctual data for the superior aquifer compared in the same graph.

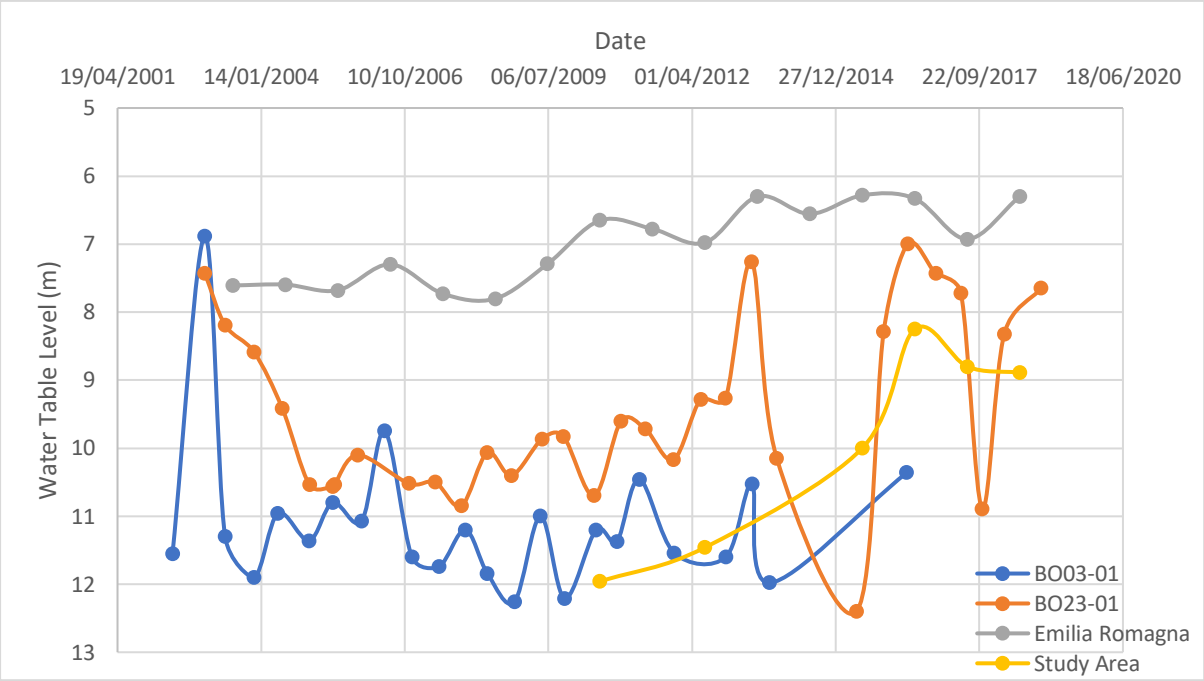

Fig. 5.22. Water Table Level for the wells, the study area, and Emilia-Romagna

By neglecting the first reading of the well BO23-01 and the May 2005 point of the well BO23-01, the outliers, we can then notice that for almost the entire period of time, the four graphs show almost the same trend.

For simulation purposes in this research, the two wells BO03-01 and BO23-01 were averaged together because they both exploit the same aquifer (confined superior aquifer), leading to more representative values, as shown in Fig. 5.23.

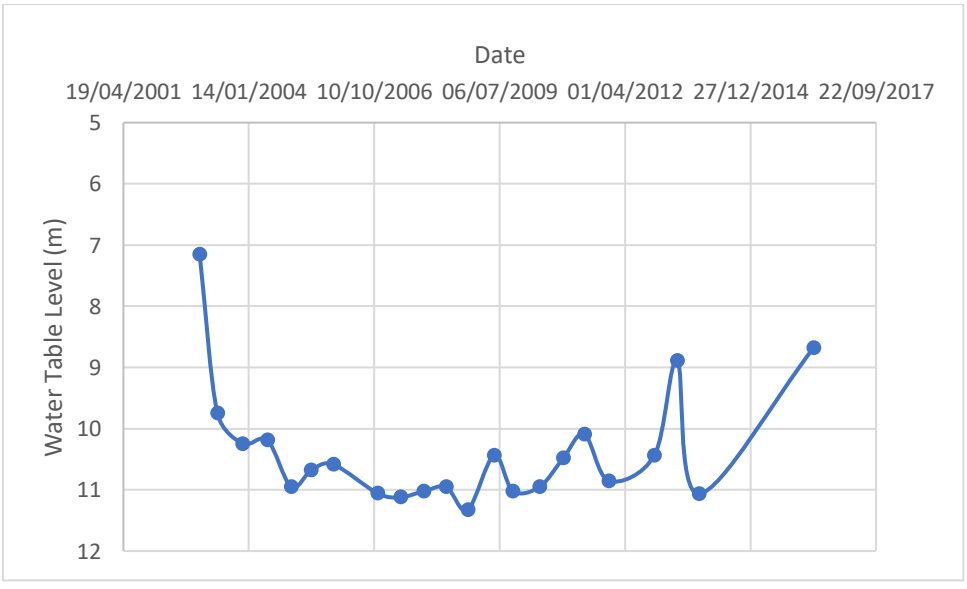

Fig. 5.23. Wells BO03-01 and BO23-01 Averaged

5.3 Pressure Calculations

Water table level the distance between the ground level and the water table.

Due to the fact that the range of flow rates of water in aquifers is as low as 0.098 mm/day (Yidana et al., 2015), which can be neglected. So, it is convenient to only consider the static component of pressure calculation.

So, to convert water table level values into pressures, the depth of the bottom of the aquifer is to be known. Then, the piezometric pressure readings, the rise of water in a well, it would be

$$p = \rho_w g(H - h)$$

Where H is the distance from the ground level to the bottom of the aquifer and h is the distance between the water table, both increasing downward.

Now we have already obtained the distance from the ground level to the water table, the water table level, so we also need to get the total distance to the bottom of the aquifer.

There were two sources for this purpose, aquifer bottom maps and geological sections.

5.3.1 Aquifer Bottom Map

The aquifer bottom map, shown in Fig. 5.24., derived from (Severi and Bonzi, 2011), shows that the aquifer bottom in the study area is about 150 m. Using this value led to an erroneously high value of initial pressure, because in the simulation, only aquifer A1 was accounted for. So, there was a necessity to get data from another source.

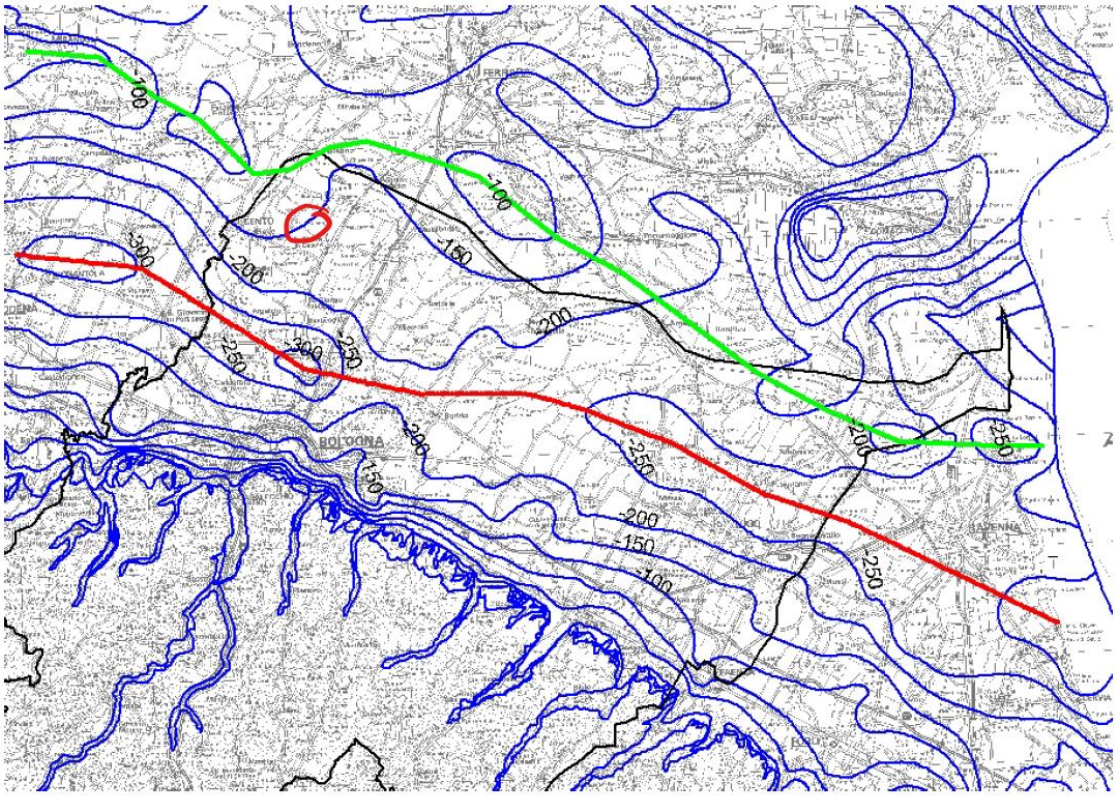

Fig. 5.24. Aquifers (A1, A2) Bottom Map with the Study Area Highlighted

5.3.2 Cross Sections

Using the (semenda.it, n.d.) website, three cross-sections could present the aquifer of interest.

Of these three, the cross section selected is number 122 (the second slanted cross section from the left), as shown in Fig. 5.25. It is further illustrated in Fig. 5.26.

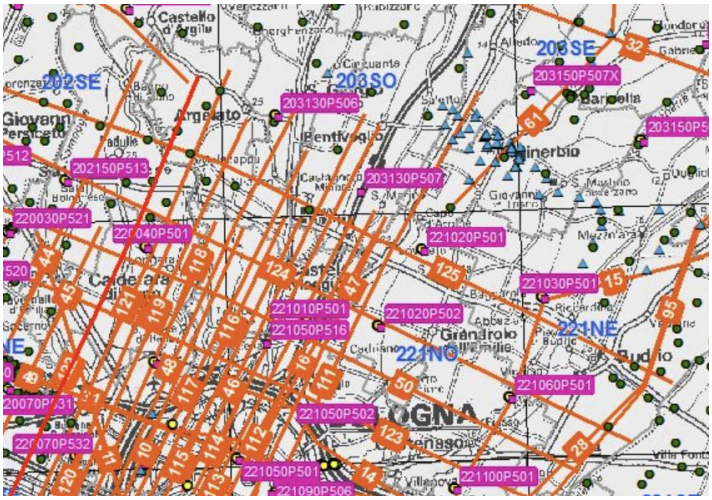

Fig. 5.25. Section 122 Location (semenda.it, n.d.)

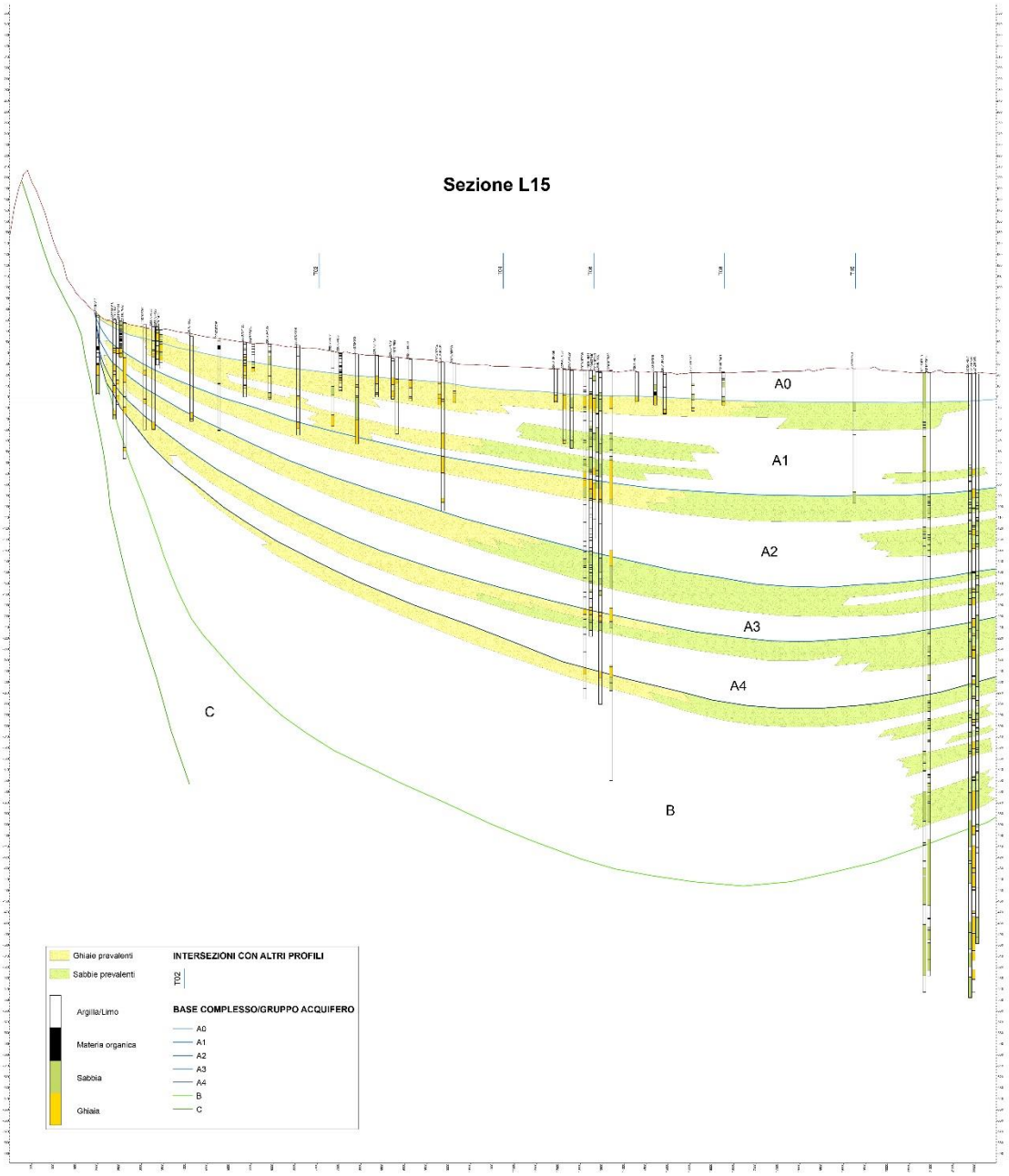

Fig. 5.26. Geological Section 123 (semenda.it, n.d.)

From this section, the well closest to the study area is the well to the far right in Fig. 5.27. was found to be (202120P605).

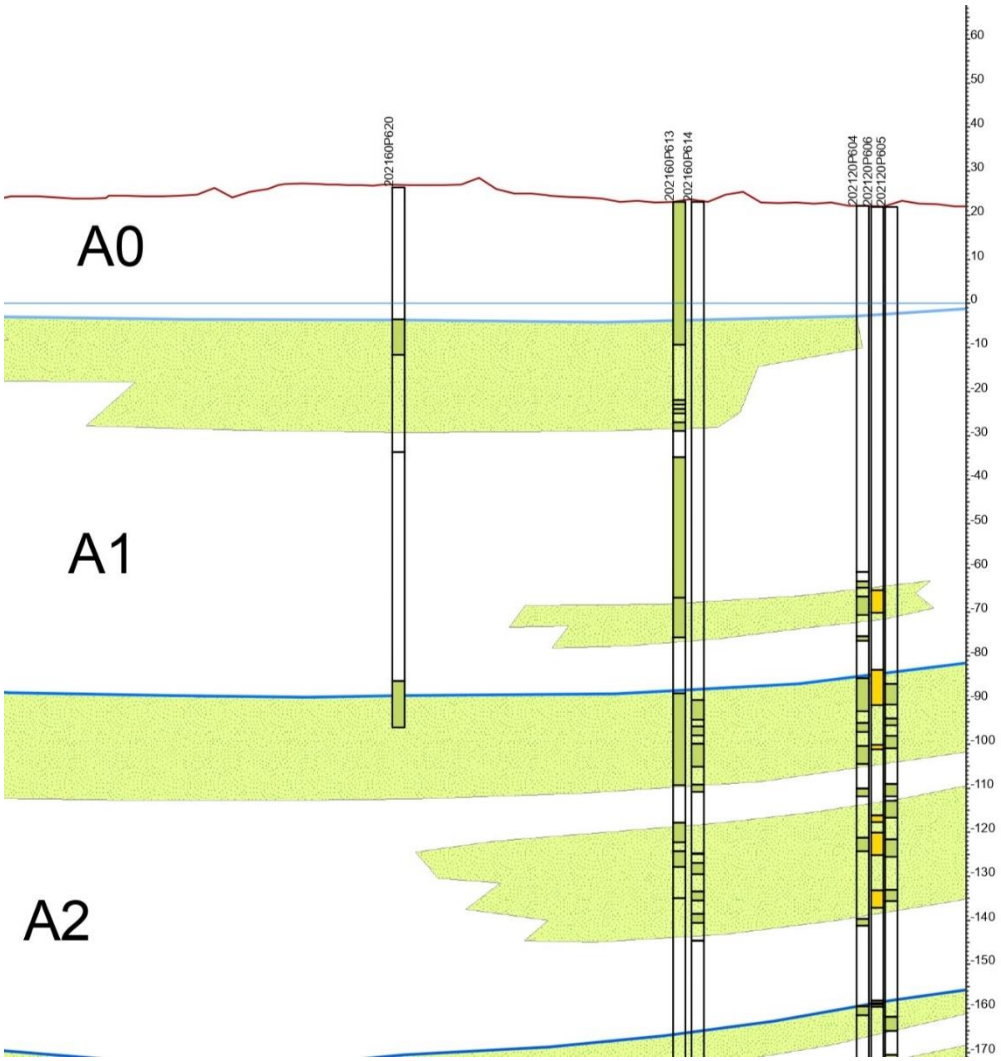

Fig. 5.27. Aquifer A1 Extension in Section 122 (semenda.it, n.d.)

From Fig. 5.27., aquifer A1 extends from 21 m above sea level to 71 m below sea level, with a total extension of 92 m from the ground surface.

6 Case Study

6.1 Fluid-Dynamic Modelling

In the first step, fluid-dynamic modelling was performed. Schlumberger Eclipse simulator was used for this step.

6.1.1 Model Setup

The study area is about 11.5 X 7.4 kilometers, norther of Bologna, as shown in Fig. 6.1. This was achieved using a grid block of the following (i X j X k = 228 X 151 X 5). The model was set up to contain the layers down to the depth of 139 m, as shown in Fig. 6.2

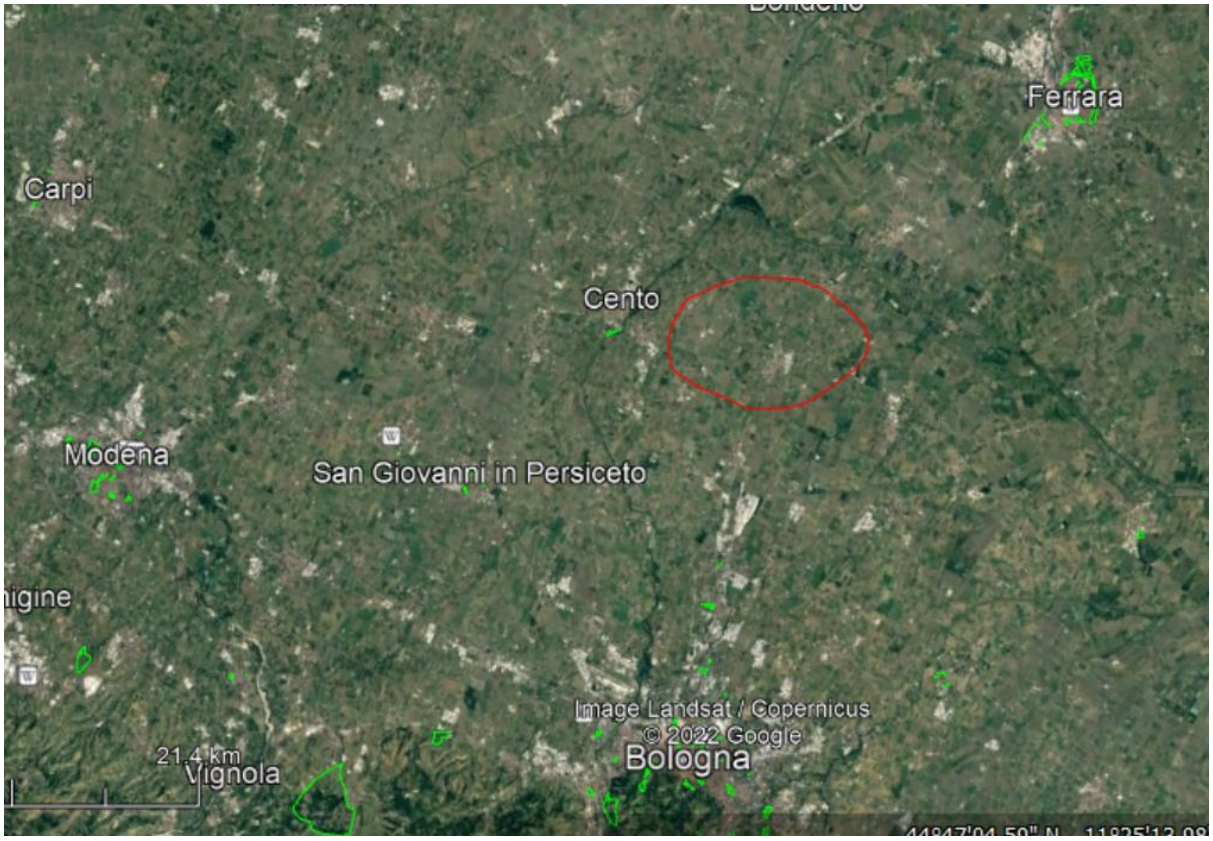

Fig. 6.1. The Study Area with the Producing Wells

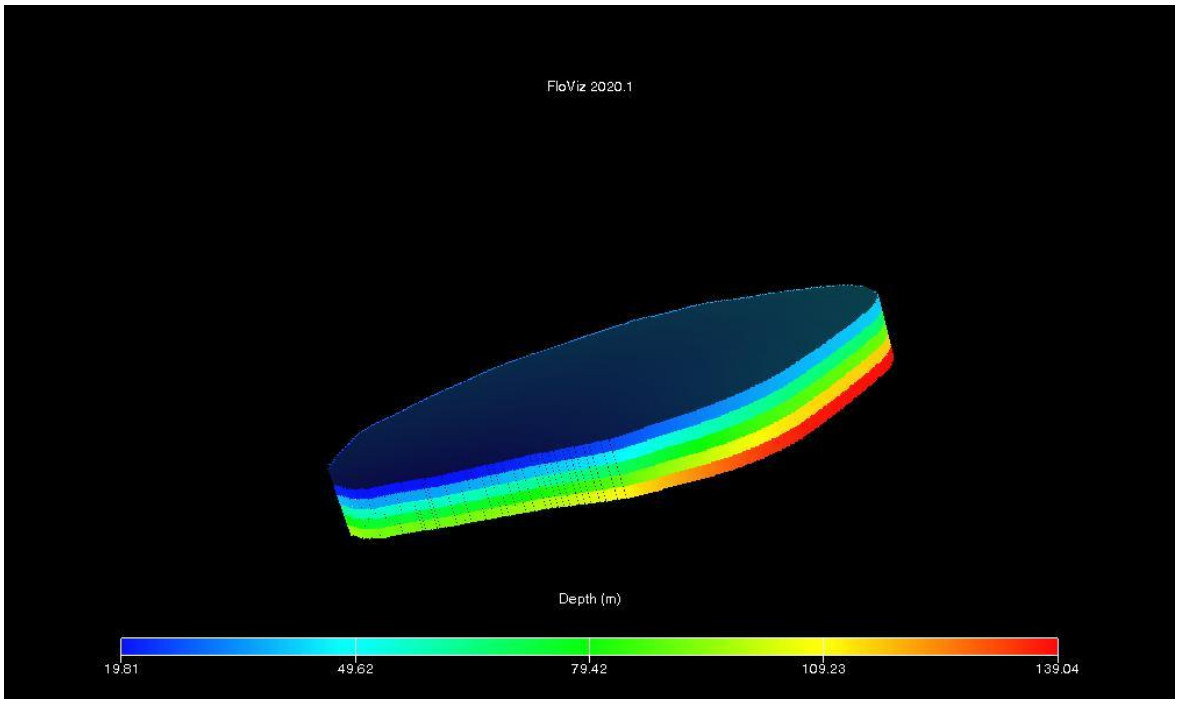

Fig. 6.2. The Aquifer Model

Then, the average porosity and compressibility values used for the simulation were estimated from the work from the previous sections to be 0.325 for sand porosity and $3.059*10^{-3}$ bar^{-1} for compressibility. Also, water compressibility was set to be equal to $8.045*10^{-5}$ bar^{-1}. Net-To-Gross ranged between 0.8 to 1. Water density was put to be 1.023 g/cm^3. Five wells, one producer and four injectors, were used for the simulation process. These wells are shown in **Error! Reference source not found.**. The injectors were introduced to account for the aquifer recharge. Analytical aquifer was not used because of numerical considerations. The analytical aquifer can not be controlled, but the injectors were better controlled.

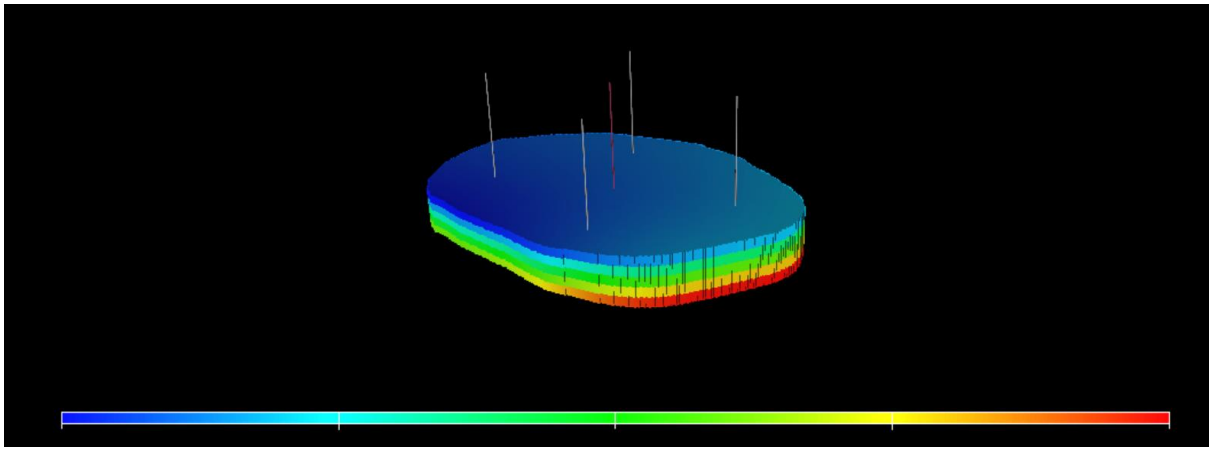

Fig. 6.3. The Model with the Wells Used

The petrophysical properties used for the simulation are summarized in the table

Table 6.1. Numerical Values of the Aquifer Properties

Property	Value
Porosity	0.325
Permeability	1.05 Darcy
Water Compressibility	8.045E-05 bar^{-1}
Water Density	1.023 g/cc
Rock Compressibility	3.05915E-03 bar^{-1}
NTG (Net To Gross)	0.8 to 1

6.1.2 History Matching

History matching is used to minimize the discrepancies between the real and the simulated data.

The flow rate to be matched was available already. However, for the pressure values, there were three choices, the Emilia-Romagna, the study area, and the two wells. For history matching, we selected the average of the two wells. This is because for the other two cases, many wells from areas that can be so far from, and thus irrelevant to, the study area.

In our study, static bottomhole pressure was selected to be matched, because it is always the same case as the dynamic pressure, as mentioned earlier, because of the nature of the low flow velocities of water in aquifers.

For this reason, injectors had been introduced and their maximum bottomhole pressures were set to be the control factor. It was selected not to exceed the initial pressure of the reservoir. Also, the

6.2 Geomechanical Modelling

For the geomechanical simulation runs, Visage software was used. It uses a Finite Element Model.

The model was built starting with the same aquifer grid in eclipse but then the geomechanical grid was created by extending the former one in all directions to be about 50 km X 50 km X 10 km (I X j X k).

For this to be done, three regions were defined; overburden, underburden, and sideburden.

1- The overburden: represents all the formation layers that lie above the study area (the grid block used in dynamic simulation).
2- The sideburden: represents all the soils and rock on the side of the main grid block used in eclipse.

3- The underburden: represents all the rocks that extend from the lower part of the main grid block down to the bottom part of the study (10 km in our case).

In all the three of these regions, in addition to the main grid block, the relevant mechanical properties were assigned according to Table 6.2.

Table 6.2. Geomechanical Characterization of the Layers Used in the Geomechanical Simulation

Geomechanical class	**Young Modulus (GPa)**	**Poisson ratio [-]**	**Bulk Density [g/cm^3]**	**Biot Coeff [-]**	Cohesion [bar]	**Friction angle [°]**	**Dilation Angle [°]**	**Tensile stress cut off [bar]**
Alluvium	**0.024**	**0.3**	**1.9**		**2**	**38**		
Gemoechanical Formation 1 - 1000m	**0.5**		**2**		**6**	**36**		
Geomechanical Formation 2 – 1200m	**5.5**		**2,.0**		**15**	**26**	**5**	**0**
Geomechanical Formation 3 - 1500m	**6**		**2.3**		**12**	**30**		
Geomechanical Formation 4 - 1600m	**13**	**0.3**		**1**				
Geomechanical Formation 5 - 1750 m	**30**							
Geomechanical Formation 6 >1750m	**40**							

We build our case on only the simple Biot and Terzaghi principle, shown in eqn. (3.22). Biot coefficient is given, and then we need to know the pore pressure to get the principal stresses.

Also, in our approach, we used the main principle stresses, assuming that

$$\sigma_H = \sigma_h = 0.8\sigma_v$$

Where σ_H, σ_h, and σ_v are the three principal stresses and σ_v is the principal vertical stress and the former two stresses are the principal horizontal stresses.

So, we needed to define only σ_v.

For initialization, the first pore pressure was established by the famous equation

$$p = \rho_w g h$$

where h here represents the cells depth.

Then, using this value, the initial principal stresses were identified.

For later steps, the pore pressure from the eclipse simulation were inserted into petrel using eclipse data file.

7 Results and Discussion

7.1 Dynamic Simulation Results

The main reason for making the dynamic simulation before the geomechanical simulation is to match the real pore pressures to be able to use the eclipse results into the geomechanical model.

The pressures to be matched are shown in

Table 7.1. Pore Pressures to be matched

Date	Average Water Table Level (m)	Total water column (m)	Water Pressure (bars)
01/01/2003	7.155	92	8.514730274
08/05/2003	9.745	92	8.254807457
26/11/2003	10.245	92	8.204629307
10/06/2004	10.19	92	8.210148903
16/12/2004	10.95	92	8.133878115
26/05/2005	10.68	92	8.160974316
17/11/2005	10.585	92	8.170508165
08/11/2006	11.06	92	8.122838922
09/05/2007	11.12	92	8.116817544
07/11/2007	11.025	92	8.126351393
06/05/2008	10.955	92	8.133376334
23/10/2008	11.33	92	8.095742721
21/05/2009	10.435	92	8.18556161
19/10/2009	11.02	92	8.126853174
20/05/2010	10.95	92	8.133878115
24/11/2010	10.485	92	8.180543795
12/05/2011	10.09	92	8.220184533
24/11/2011	10.855	92	8.143411964
20/11/2012	10.435	92	8.18556161
21/05/2013	8.895	92	8.340110312
12/11/2013	11.065	92	8.122337141
12/05/2016	8.68	92	8.361686916

As stated earlier, the static pressure was appropriate to choose for the matching process.

Error! Reference source not found.. shows the matching of the pressure. The reason for the unmatched data at the beginning and end of the period can be due to the fact that the sharp decrease in pressure values can be erroneous data because there are many wells that are close together, which means that they can affect the response of each other.

In the end of the period, there is a sharp decrease because one of the wells shows that sharp decrease, which can simply be attributed to a human error or a mechanical error of the monitoring device itself, or even the same reason as the spurious data at the beginning. Also, it should be noted that the pressure tends to be stabilized for the majority of the years of the study.

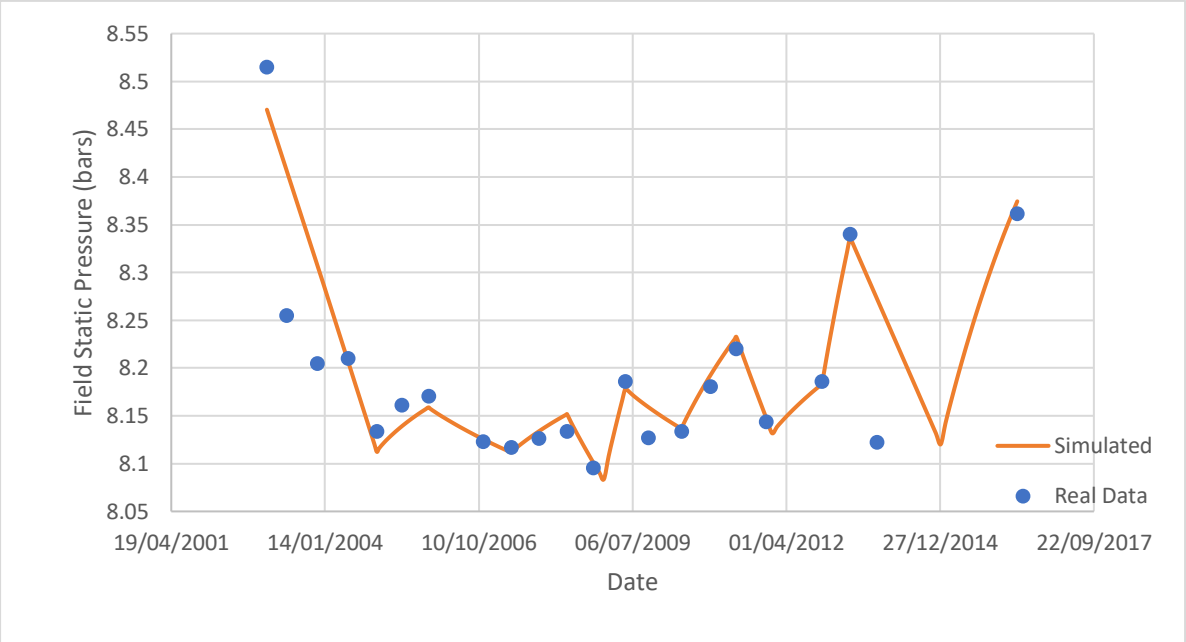

Fig. 7.1. History Matched Pressure Data

Finally, the production history was matched according to **Error! Reference source not found.**.

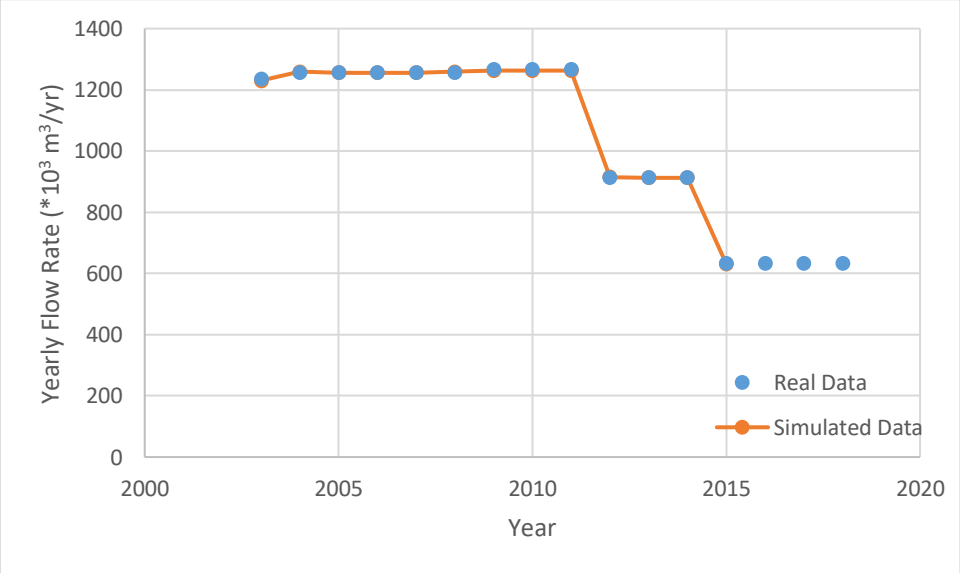

Fig. 7.2. History Matched Yearly Flow Rate

It should be noted that the simulation was stopped in May 2016, because the data of the pressure of both wells were available till May 2016.

On another note, it can be said that maybe the production decrease can be one of the reasons that contributed to the increase in the pressure from 2015.

7.2 Geomechanical Simulation

Geomechanical simulator was used for the calculation of the land subsidence.

For this purpose, with the first data point, four other points were selected.

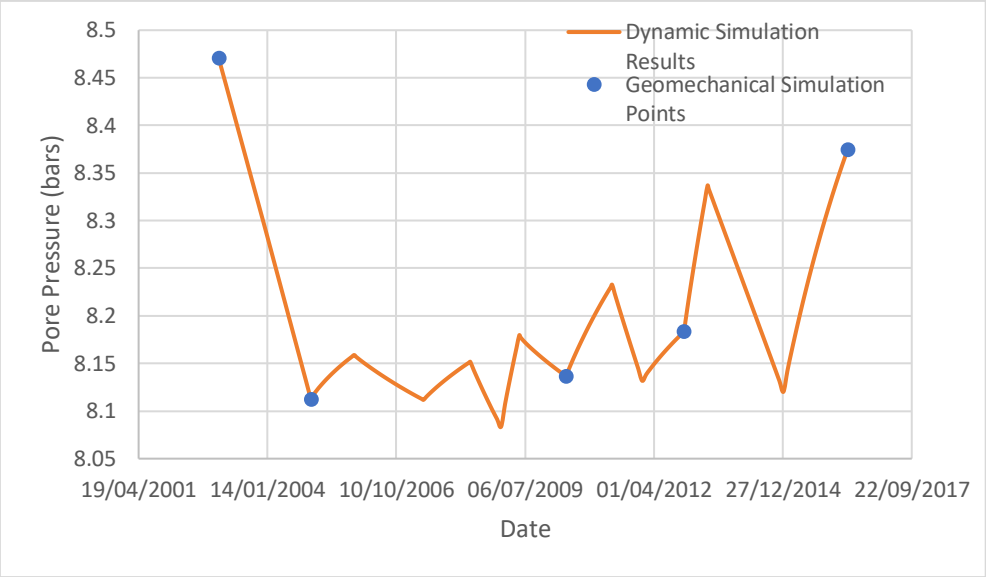

Fig. 7.3. The Selected Points for the Subsidence Calculation with respect to the Dynamic Simulation Results

The four points are on the following dates (dd/mm/yyyy)

16/12/2004, 20/05/2010, 20/11/2012, and 12/05/2016.+The reason behind this selection is as follows;

1- The first point shows a large decrease in pressure, whether is erroneous or not, so it shows the maximum subsidence.
2- Between the point of 2004 and that of 2010, the pressure shows small fluctuations in the same range of average pressure, so the points in between were not chosen. Also, the pressure differential between these two points is not so large, giving rise to low subsidence, or uplift in this case, magnitude.
3- Between the point of 2010 and that in November 2012, the recharge starts to become greater than the discharge, so it is the start of the actual uplift during this period.
4- Finally, the last point of May 2016 is the last point in the study that had a known pressure. So, it was necessary to choose it to terminate the study.

Fig. 7.4. shows the subsidence due to water production till 16/12/2004. It has a magnitude of about 24 centimetres. This is attributed again to the large pressure decrease during that period of time.

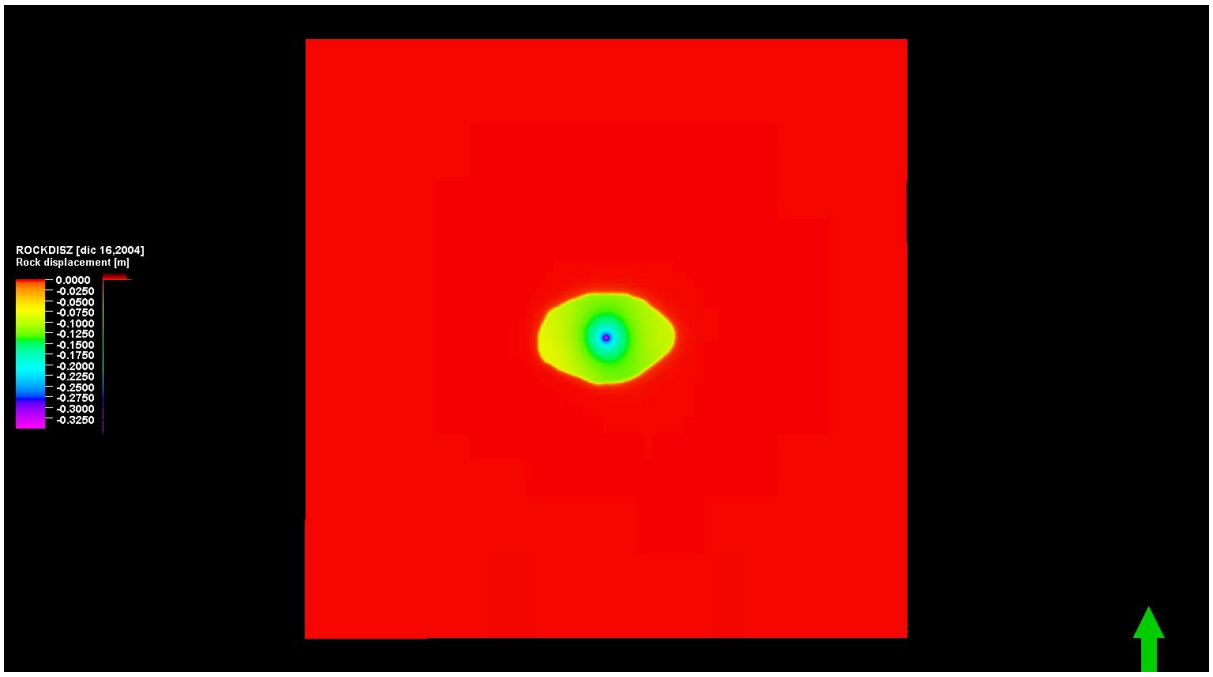

Fig. 7.4. Subsidence due to Water Production from January 2003 to December 2004

This can be also shown by the corresponding pressure map, shown in Fig. 7.5. Pressure decreased about 0.5 bars. So, it gives an indication of the subsidence occurred during that period of time.

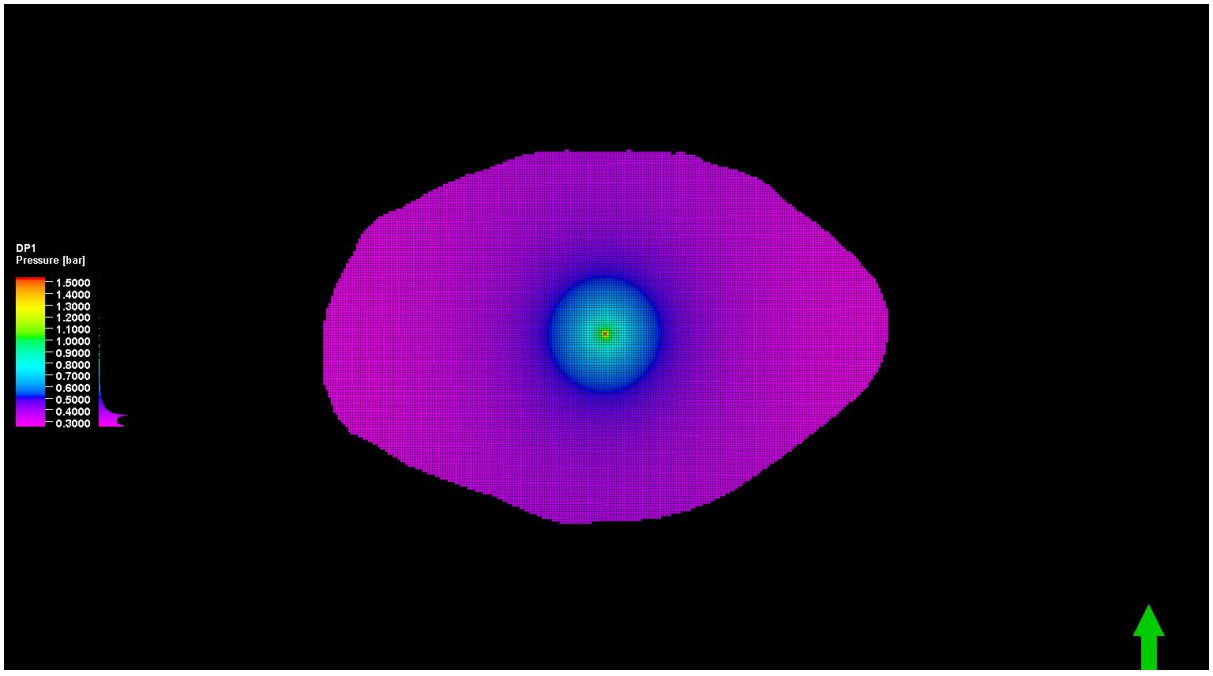

Fig. 7.5. Pressure Map from 01/01/2003 till 16/12/2004

Then, total subsidence from 01/01/2003 to May 2010 is shown in Fig. 7.6. It is noted that there was a very slight uplifting, barely noticeable. Giving rise to a total subsidence of about 18 cm.

It is also prudent to say that there are a huge uplift shown in the graph, but it is due to the fact that the injectors were used. Their position causes such an uplift because they were put into operation to account for the increase in pressure that occurred.

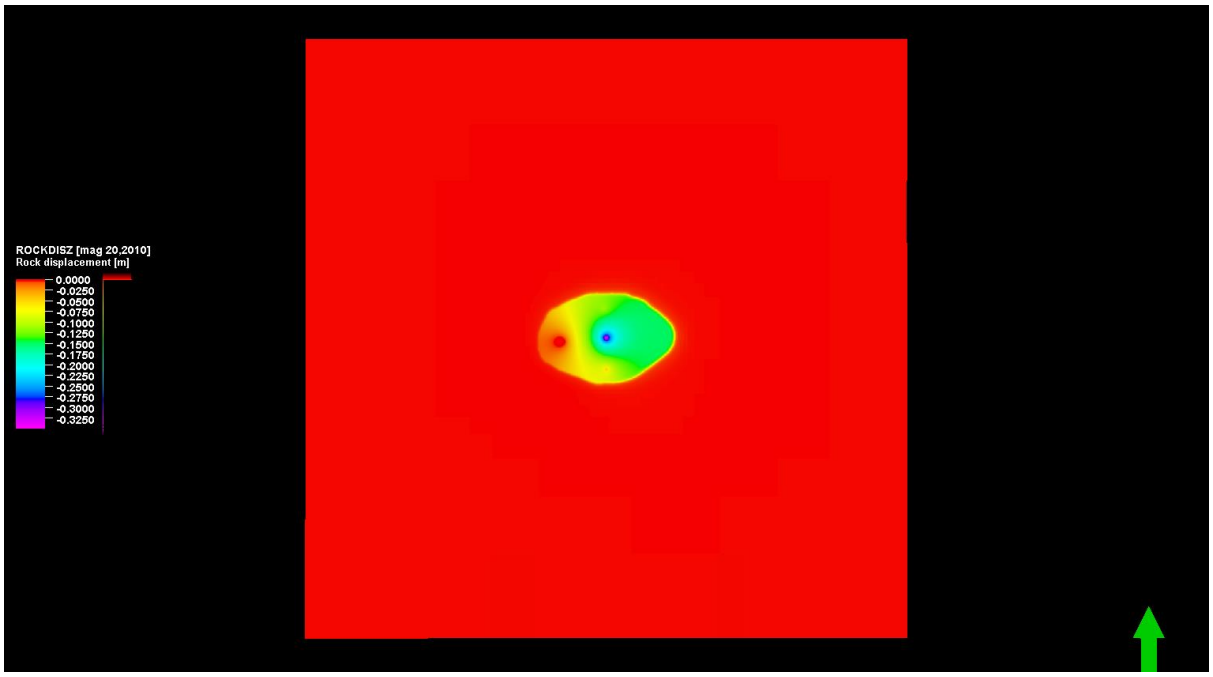

Fig. 7.6. Subsidence due to Water Production till May 2010

Again, Fig. 7.7. shows that the pressure readings coincide with the subsidence/uplifting results. Also, the effect of the injectors can be seen clearly here. The pressure seems to have increased by about 0.05 bars. Since we assume elastic-domain conditions, the pressure recharge causes the rock to return to its initial state, without showing plastic deformations.

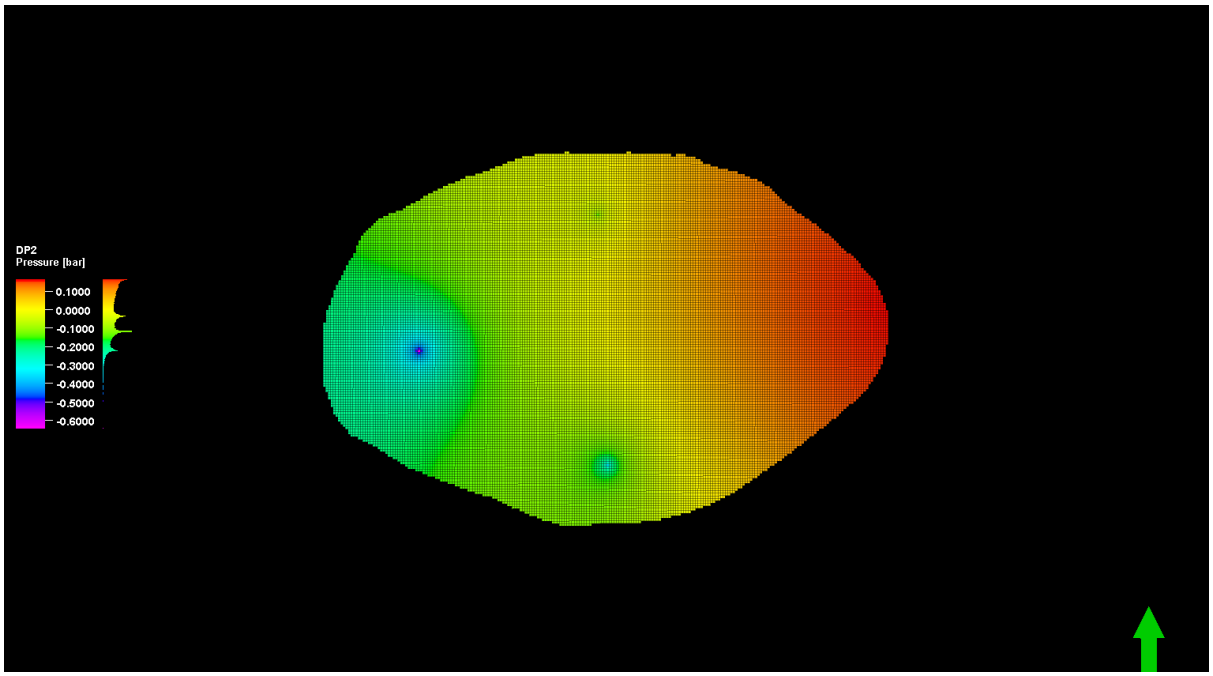

Fig. 7.7. Pressure Change from 16/12/2004 to 20/05/2010

Then, the total subsidence from the start till 20/11/2012 can be shown in Fig. 7.8. Again, further more uplift can be noticed.

The total subsidence from the beginning of January 2003 till November 2012 is about 17 cm. Again, decreased due to further pressure increase due to the aquifer recharge.

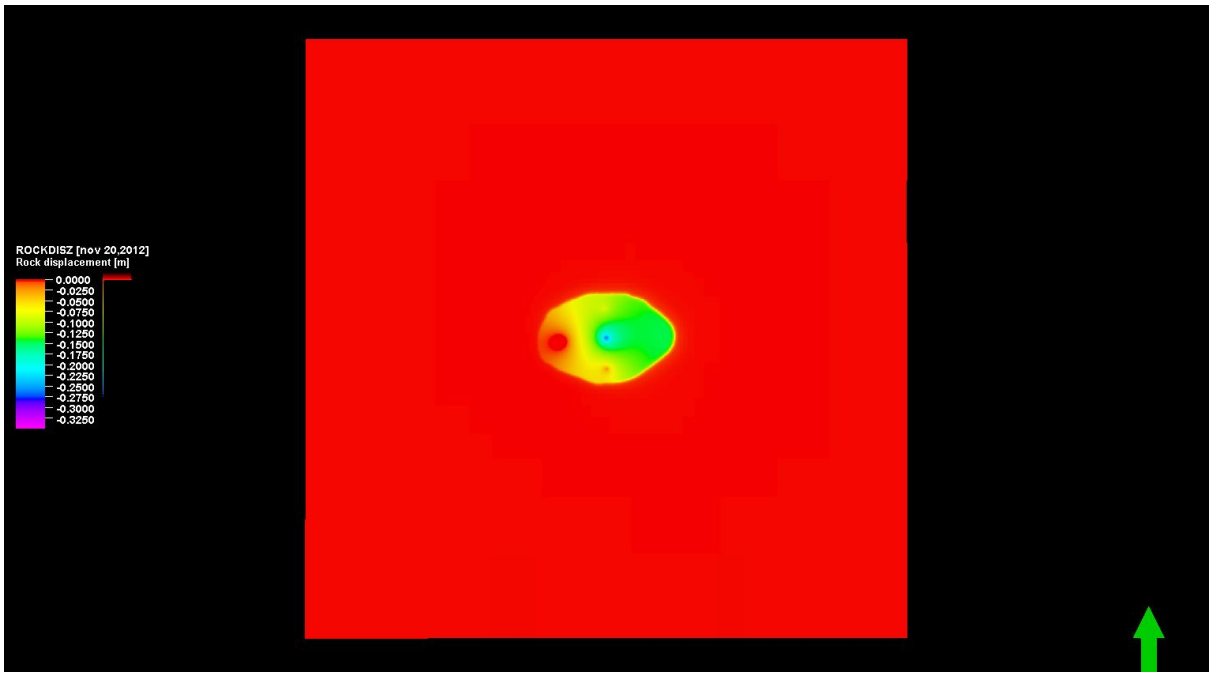

Fig. 7.8. Subsidence due to Water Production from 01/01/2003 to 20/11/2012

Also, here the pressure seems to further increase by about 0.05 bars. Which is an indication of the uplifting occurred.

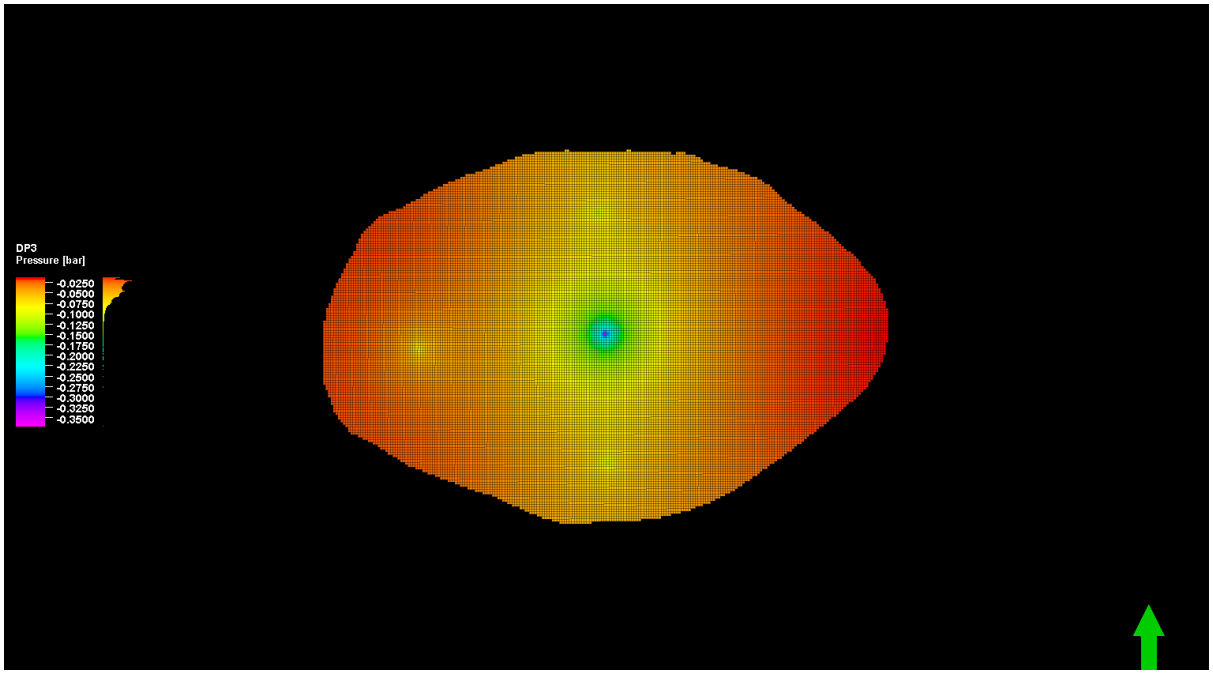

Fig. 7.9. Pressure Change from 20/05/2010 to 20/11/2012

Finally, Fig. 7.10. shows the total subsidence due to water production through the entire period of the study.

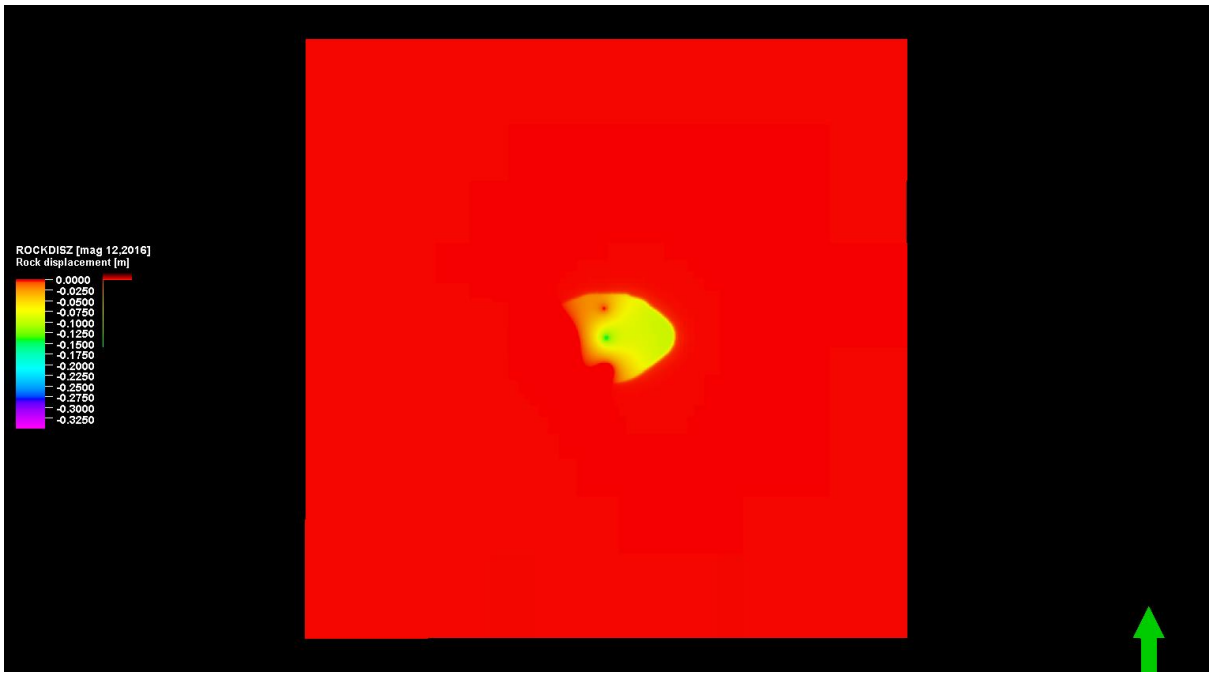

Fig. 7.10. Total Subsidence through the Entire Period of Time

It shows that the total subsidence due to water production during the entire study period of time, from 01/01/2003 to 12/05/2016 was about 8 cm. The decrease in subsidence can be attributed to the aquifer recharge.

Fig. 7.11. shows the last pressure map from 2012 to 2016. It shows an increase in pressure by about 0.2 bars, giving rise to the uplifting that was shown.

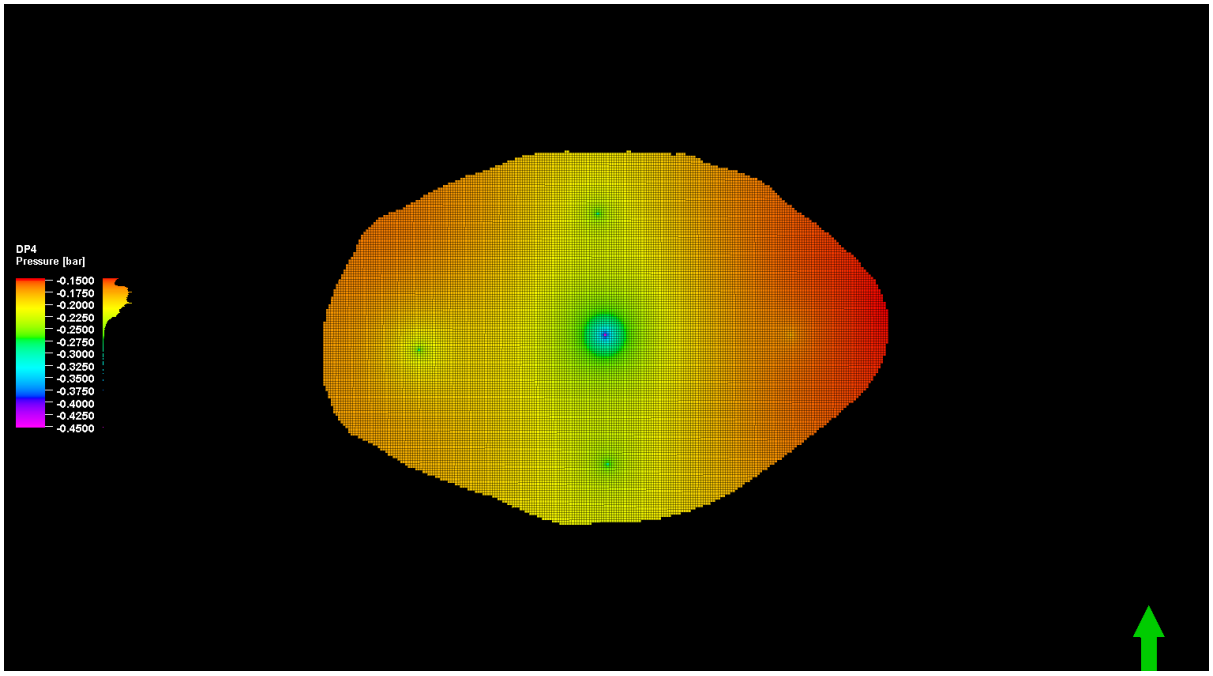

Fig. 7.11. Pressure Differential Map from 20/11/2012 to 12/05/2016

8 Conclusion

The dynamic and the geomechanical simulations of the shallow confined aquifer in a study area in Emilia-Romagna were conducted. To perform these simulations, a specific workflow was followed.

1. The geological framework of the Po plain aquifers was investigated. It was found that there are 3 major aquifer systems, A, B, and C aquifers that are separated by regional unconformities. Then, each group is subdivided into smaller aquifer systems. The aquifer of our interest in this study was the aquifer A1, which is the shallowest confined aquifer of aquifer group A. It extends down to about 100m.
2. For that aquifer, A1, the petrophysical characteristics, porosity, hydraulic conductivity, vertical compressibility, and the geomechanical properties were defined. These properties were assumed to be homogeneous across the study area. Also, production history over the last 20 years was collected. Moreover, the piezometric data for Emilia-Romagna, the study area, and the punctual data of two wells in the study area were collected over the period from 2003 to 2016, for the wells, and till 2018 for the production data and the piezometric data of Emilia-Romagna and the study area. Then, the average pressure values of the two wells were calculated and used as the real pressure to be matched by the dynamic simulation. This dataset was of utmost importance to get started with the dynamic simulation.
3. After that, the dynamic simulation was performed and initialized. Then, history matching was performed to reproduce the production and pressure data. We obtained a perfect match except for two points which were believed to have erroneous data affected by the nearby wells or by human or machine errors. Or maybe a flood has affected the investigation area during that time.
4. Finally, after matching the dynamic data, a geomechanical simulation was established using Finite Element software. The pressures from the dynamic simulation were used as an input for this simulation. When the pressure increased, an uplift rather than subsidence occurred. Also, pressure maps confirmed that, but there were injection wells that had been used earlier for the dynamic simulation match affected these pressure maps.

With this workflow, subsidence was calculated along the entire period to be about 8 cm. It was more than this in the first year of study due to a large drawdown, causing more subsidence. Then, uplifting occurred due to aquifer recharge. This is also justified by the pressure measurements. As the pressure decreased by about 0.4 bars in the first year, from 2003 to 2004, then, stabilized till 2012, with minor fluctuations and minor subsidence changes. Then, from 2012 to 2016, the period of uplifting started and the pressure increased for about 0.2 bars, recovering a large part of the subsidence through uplifting, causing a total subsidence of about 8 cm.

9 References

Abdoljalal, 2010. Fully Integrated Hydrocarbon Reservoir Studies: Myth or Reality? Am. J. Appl. Sci. 7, 1477–1486. https://doi.org/10.3844/ajassp.2010.1477.1486

Amorosi, A., Cibin, U., Severi, P., Stefani, M., Gabbianelli, G., Simeoni, U., Vincenzi, S., 2004. Field Trips Guide Books - From B16 to B33.

Amorosi, A., Pavesi, M., n.d. Aquifer stratigraphy from the middle-late Pleistocene succession of the Po Basin - Stratigrafia di sistemi acquiferi nella successione medio - e tardo pleistocenica del Bacino Padano, in: Memorie Descrittive Della Carta Geologica d'Italia Atti Del Secondo Workshop Nazionale: L'approccio Multidisciplinare Allo Studio Degli Acquiferi Porosi.

Arpae, n.d. Environmental Themes [WWW Document]. URL https://servizi-gis.arpae.it/Html5Viewer/index.html?locale=it-IT&viewer&viewer=Geoportal.Geoportalhttps://servizi-gis.arpae.it/Html5Viewer/index.html?locale=it-IT&viewer&viewer=Geoportal.Geoportal

Benetatos, C., Codegone, G., Ferraro, C., Mantegazzi, A., Rocca, V., Tango, G., Trillo, F., 2020. Multidisciplinary Analysis of Ground Movements: An Underground Gas Storage Case Study. Remote Sens. 12, 3487. https://doi.org/10.3390/rs12213487

Biot, M.A., 1941. General Theory of Three-Dimensional Consolidation. J. Appl. Phys. 12, 155–164. https://doi.org/10.1063/1.1712886

Carminati, E., Martinelli, G., 2002. Subsidence rates in the Po Plain, northern Italy: the relative impact of natural and anthropogenic causation. Eng. Geol. 66, 241–255. https://doi.org/10.1016/S0013-7952(02)00031-5

Cashman, P.M., Preene, M., 2013. Groundwater lowering in construction: a practical guide to dewatering, 2nd ed. ed, Applied geotechnics. Taylor & Francis, Boca Raton (Fla.).

Castaldini, D., Marchetti, M., Norini, G., Vandelli, V., Zuluaga Vélez, M.C., 2019. Geomorphology of the central Po Plain, Northern Italy. J. Maps 15, 780–787. https://doi.org/10.1080/17445647.2019.1673222

Cong, X., Mao, X., Su, M., Wu, N., Yu, X., Yang, R., 2015. Tectonic Subsidence Calculation Based on Seismic Data [1]: Presented at the 3rd International Conference on Mechatronics, Robotics and Automation, Shenzhen, China. https://doi.org/10.2991/icmra-15.2015.243

Fanchi, J.R., 2018. Introduction to Reservoir Simulation, in: Principles of Applied Reservoir Simulation. Elsevier, pp. 1–8. https://doi.org/10.1016/B978-0-12-815563-9.00001-X

Farina, M., Marcaccio, M., Zavatti, A., 2014. Esperienze e prospettive nel monitoraggio delle acque sotterranee. Il contributo dell'Emilia-Romagna. Unpublished. https://doi.org/10.13140/RG.2.1.3927.2725

Fjaer, E. (Ed.), 2008. Petroleum related rock mechanics, 2nd ed. ed, Developments in petroleum science. Elsevier, Amsterdam ; Boston.

Galloway, D., Bawden, G., Leake, S., Honegger, D., 2008. Land subsidence hazards. Landslide Land Subsid. Hazards Pipelines US Geol Surv Open-File Rep 1164.

Galloway, D., Erkens, G., Kuniansky, E., Rowland, J., 2016. Land Subsidence Processes. Hydrogeol. J. 24.

Gambolati, G., 1998. CENAS: Coastline Evolution of the Upper Adriatic Sea due to Sea Level Rise and Natural and Anthropogenic Land Subsidence. Springer Netherlands, Dordrecht.

Gambolati, G., Teatini, P., 2021. Land Subsidence and its Mitigation. The Groundwater Project.

Gambolati, G., Teatini, P., 2015. Geomechanics of subsurface water withdrawal and injection: GROUNDWATER GEOMECHANICS. Water Resour. Res. 51, 3922–3955. https://doi.org/10.1002/2014WR016841

Gambolati, G., Teatini, P., Baú, D., Ferronato, M., 2000. Importance of poroelastic coupling in dynamically active aquifers of the Po River Basin, Italy. Water Resour. Res. 36, 2443–2459. https://doi.org/10.1029/2000WR900127

Giani, G., Orsatti, S., Peter, C., Rocca, V., 2018. A Coupled Fluid Flow—Geomechanical Approach for Subsidence Numerical Simulation. Energies 11, 1804. https://doi.org/10.3390/en11071804

Gould, P.L., 2013. Introduction to linear elasticity, 3rd ed. ed. Springer, New York ; Heidelberg.

Greuter, Turco, M., Petersen, C., Wang, G., 2021. Impacts of Groundwater Withdrawal Regulation on Subsidence in Harris and Galveston Counties, Texas, 1978–2020 71, 109–118.

Herrera-García, G., Ezquerro, P., Tomás, R., Béjar-Pizarro, M., López-Vinielles, J., Rossi, M., Mateos, R.M., Carreón-Freyre, D., Lambert, J., Teatini, P., Cabral-Cano, E., Erkens, G., Galloway, D., Hung, W.-C., Kakar, N., Sneed, M., Tosi, L., Wang, H., Ye, S., 2021. Mapping the global threat of land subsidence. Science 371, 34–36. https://doi.org/10.1126/science.abb8549

Hirsch, K.K., Scheck-Wenderoth, M., van Wees, J.-D., Kuhlmann, G., Paton, D.A., 2010. Tectonic subsidence history and thermal evolution of the Orange Basin. Mar. Pet. Geol. 27, 565–584. https://doi.org/10.1016/j.marpetgeo.2009.06.009

Holzer, T.L., Galloway, D.L., 2005. Impacts of land subsidence caused by withdrawal of underground fluids in the United States, in: Humans as Geologic Agents. Geological Society of America. https://doi.org/10.1130/2005.4016(08)

Ingersoll, R.V., 2011. Tectonics of Sedimentary Basins, with Revised Nomenclature, in: Busby, C., Azor, A. (Eds.), Tectonics of Sedimentary Basins. John Wiley & Sons, Ltd, Chichester, UK, pp. 1–43. https://doi.org/10.1002/9781444347166.ch1

La rete di monitoraggio [WWW Document], n.d. URL https://webbook.arpae.it/export/shared/immagini/ACQUE-SOTTERRANEE/Rete-di-monitoraggio-acque-sotterranee-2019.jpg

Laloui, L., Rotta Loria, A.F., 2020. Analysis and design of energy geostructures: theoretical essentials and practical application. Academic Press, London San Diego Cambridge Oxford.

Livello delle acque sotterranee [WWW Document], n.d. URL https://webbook.arpae.it/indicatore/Livello-delle-acque-sotterranee-00001/?espandi=grafici&cat=mappe

Longuemare, P., Mainguy, M., Lemonnier, P., Onaisi, A., Gérard, C., Koutsabeloulis, N., 2002. Geomechanics in Reservoir Simulation: Overview of Coupling Methods and Field Case Study. Oil Gas Sci. Technol. 57, 471–483. https://doi.org/10.2516/ogst:2002031

Marcaccio, M., Lucchini, D., 2020. VALUTAZIONE DELLO STATO DELLE ACQUE SOTTERRANEE 2014 - 2019.

Modoni, G., Saroli, M., Croce, P., 2008. Land subsidence induced by groundwater extraction: the case of Bologna. Presented at the IEMSs 2008: International Congress on Environmental Modelling and Software, BARCELONA, CATALONIA, SPAIN.

Qin, H., Andrews, C.B., Tian, F., Cao, G., Luo, Y., Liu, J., Zheng, C., 2018. Groundwater-pumping optimization for land-subsidence control in Beijing plain, China. Hydrogeol. J. 26, 1061–1081. https://doi.org/10.1007/s10040-017-1712-z

Ritzema, H.P. (Ed.), 1994. Drainage principles and applications, 2. ed. (completely rev.). ed, ILRI publication. ILRI, Wageningen.

semenda.it, n.d. sezioni geologiche e prove geognostiche della pianura emiliano-romagnola.

Severi, P., Bonzi, L., 2012. Introduzione all'idrogeologia della pianura emiliano-romagnola.

Severi, P., Bonzi, L., 2011. Distribuzione degli acquiferi padani nel sottosuolo della pianura bolognese RELAZIONE GEOLOGICA.

Shen, S.-L., Xu, Y.-S., Hong, Z.-S., 2006. Estimation of Land Subsidence Based on Groundwater Flow Model. Mar. Georesources Geotechnol. 24, 149–167. https://doi.org/10.1080/10641190600704848

Spacagna, R.L., Modoni, G., Saroli, M., 2020. An Integrated Model for the Assessment of Subsidence Risk in the Area of Bologna (Italy). pp. 358–368. https://doi.org/10.1007/978-3-030-21359-6_38

Stramondo, S., Saroli, M., Tolomei, C., Moro, M., Doumaz, F., Pesci, A., Loddo, F., Baldi, P., Boschi, E., 2007. Surface movements in Bologna (Po Plain — Italy) detected by multitemporal DInSAR. Remote Sens. Environ. 110, 304–316. https://doi.org/10.1016/j.rse.2007.02.023

Sun, H., Grandstaff, D., Shagam, R., 1999. Land subsidence due to groundwater withdrawal: Potential damage of subsidence and sea level rise in southern New Jersey, USA. Env. Geol 37, 290–296. https://doi.org/10.1007/s002540050386

Taherynia, M.H., Aghda, S.M.F., Ghazifard, A., 2013. Modeling of Land Subsidence in the South Pars Gas Field (Iran). Int. J. Geosci. 04, 1095–1100. https://doi.org/10.4236/ijg.2013.47103

Teatini, P., Ferronato, M., Gambolati, G., Gonella, M., 2006. Groundwater pumping and land subsidence in the Emilia-Romagna coastland, Italy: Modeling the past occurrence and the future trend: MODELING LAND SUBSIDENCE. Water Resour. Res. 42. https://doi.org/10.1029/2005WR004242

Terzaghi, K., 1923. Die Berechnung der Durchlässigkeitsziffer des Tones aus dem Verlauf der hydrodynamischen Spannungserscheinungen, 3/4,. ed. Akademie der Wissens chaften in Wien, Matematisch – Naturwissen – Schaftliche Klasse. Sitzungsberichte. Abteilung II, Wien.

Terzaghi, K., Peck, R.B., Mesri, G., 1996. Soil mechanics in engineering practice. Wiley, New Delhi.

Uko, E.D., Famuyibo, D.A., Okiongbo, K., 2018. Estimation of Land Surface Subsidence Induced by Hydrocarbon Production in the Niger Delta, Nigeria, Using Time-Lapse Orthometric Leveling Data. SSRN Electron. J. https://doi.org/10.2139/ssrn.3214967

Wade, C.M., Cobourn, K., Sullivan, J., Amacher, G., Hester, E., 2016. Groundwater Pumping Decisions and Land Subsidence in the Southern Chesapeake Bay Region of Virginia. https://doi.org/10.13140/RG.2.2.13735.34721

Yidana, S.M., Alo, C., Addai, M.O., Fynn, O.F., Essel, S.K., 2015. Numerical analysis of groundwater flow and potential in parts of a crystalline aquifer system in Northern Ghana. Int. J. Environ. Sci. Technol. 12, 3805–3818. https://doi.org/10.1007/s13762-015-0805-2

Zoback, M.D., 2007. Reservoir geomechanics. Cambridge university press, Cambridge.

10 Appendixes

10.1 Well BO03-01

CODICE	**BO03-01**
COMUNE	**SAN PIETRO IN CASALE**
SIGLA_PROV	**BO**
PROFONDITA	**205**
ACQUIFERO	**A2,A3,A4**
TIPO_MISURA	**Analisi chimica e Livello piezometrico**
PROPRIETA_DATO	**Servizio Tutela e Risanamento Risorsa Acqua - Regione Emilia-Romagna**
GESTORE_DATO	**ARPA - Agenzia Regionale Prevenzione e Ambiente - Regione Emilia-Romagna**
USO	**Industriale**
DATA_INIZIO	**07-MAG-2002**

Table 10.1. Water Table Level of Well BO03-01

Well	Date (dd/mm/yyyy)	Water Table Level (m)
BO03-01	07/05/2002	11.55
	18/12/2002	6.88
	08/05/2003	11.3
	26/11/2003	11.9
	10/05/2004	10.96
	13/12/2004	11.36
	26/05/2005	10.8
	14/12/2005	11.07
	24/05/2006	9.75
	29/11/2006	11.6
	06/06/2007	11.74
	05/12/2007	11.2
	07/05/2008	11.84
	11/11/2008	12.26
	12/05/2009	11
	28/10/2009	12.21
	03/06/2010	11.2
	26/10/2010	11.37
	31/03/2011	10.46
	29/11/2011	11.54
	22/11/2012	11.6
	23/05/2013	10.53
	24/09/2013	11.98

	05/05/2016	10.36

10.2 Well BO23-01

Code	PB23-01
Name of the Database	Emilia-Romagna Region (Italy)
Depth of the well	115.0 meters
Share of the campaign plan	15.85 meters
Reference level	Average Adriatic Sea Level
Reference system	Coordinates UTM 32 Nord (Datum ED50)
X-coordinate	692344
Y Coordinate	4944360
Managing body	Water Resource Protection and Rehabilitation Service - Emilia-Romagna Region
Responsible body	ARPA - Regional Agency for Prevention and Environment - Emilia-Romagna Region
Use	Industrial
Date of first measure	12/05/1988

Table 10.2. Water Table Level of Well BO23-01

Code	Data (dd/mm/yyyy)	Water Table Level (m)
BO23-01	18/12/2002	7.43
	08/05/2003	8.19
	26/11/2003	8.59
	10/06/2004	9.42
	16/12/2004	10.54
	26/05/2005	10.56
	08/06/2005	10.54
	17/11/2005	10.10
	08/11/2006	10.52
	09/05/2007	10.50
	07/11/2007	10.85
	06/05/2008	10.07
	23/10/2008	10.40
	21/05/2009	9.87
	19/10/2009	9.83
	20/05/2010	10.70
	24/11/2010	9.60
	12/05/2011	9.72
	24/11/2011	10.17
	31/05/2012	9.28
	20/11/2012	9.27

	21/05/2013	7.26
	12/11/2013	10.15
	21/05/2015	12.40
	26/11/2015	8.29
	12/05/2016	7.00
	22/11/2016	7.43
	17/05/2017	7.72
	12/10/2017	10.89
	15/03/2018	8.32
	27/11/2018	7.65

10.3 The Two Wells Averaged Values

Table 10.3. Average Water Table Level Values for the Two Wells

Date	Average Water Table Level (m)	pressure (bars)
01/01/2003	7.155	8.51
08/05/2003	9.745	8.25
26/11/2003	10.245	8.20
10/06/2004	10.19	8.21
16/12/2004	10.95	8.13
26/05/2005	10.68	8.16
17/11/2005	10.585	8.17
08/11/2006	11.06	8.12
09/05/2007	11.12	8.12
07/11/2007	11.025	8.13
06/05/2008	10.955	8.13
23/10/2008	11.33	8.10
21/05/2009	10.435	8.19
19/10/2009	11.02	8.13
20/05/2010	10.95	8.13
24/11/2010	10.485	8.18
12/05/2011	10.09	8.22
24/11/2011	10.855	8.14
20/11/2012	10.435	8.19
21/05/2013	8.895	8.34
12/11/2013	11.065	8.12
12/05/2016	8.68	8.36

10.4 History Matching

Table 10.4. Simulation Output

Date	Field Pressure (bars)

01/01/2003	8.47
08/05/2003	8.30
26/11/2003	8.26
10/06/2004	8.27
16/12/2004	8.19
26/05/2005	8.21
17/11/2005	8.22
08/11/2006	8.15
09/05/2007	8.14
07/11/2007	8.14
06/05/2008	8.15
23/10/2008	8.10
21/05/2009	8.14
19/10/2009	8.08
20/05/2010	8.09
24/11/2010	8.13
12/05/2011	8.16
24/11/2011	8.09
20/11/2012	8.12
21/05/2013	8.21
12/11/2013	8.01
12/05/2016	8.26